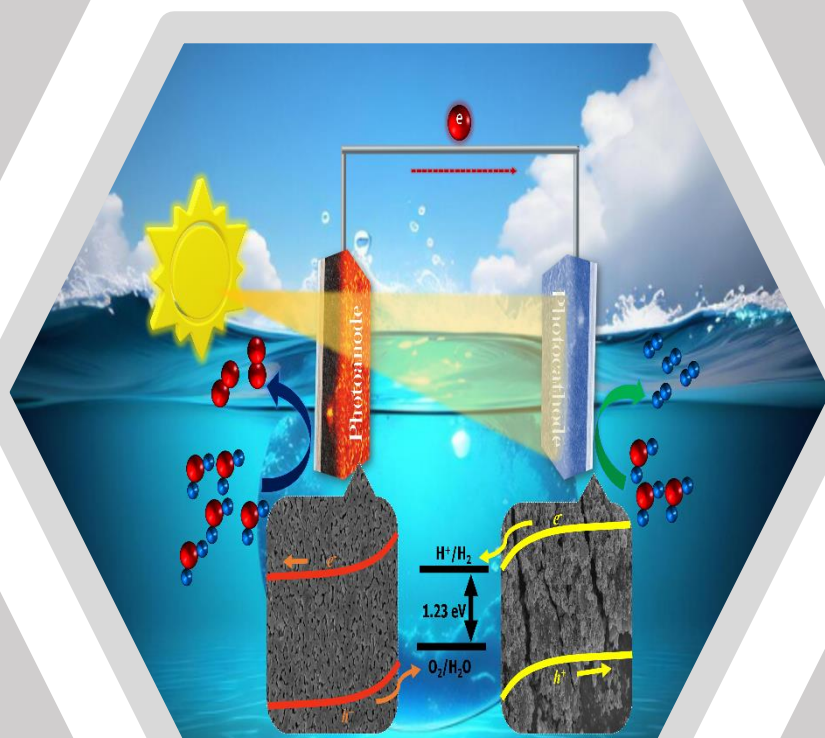


*Workshop on
Electrochemical Science
& Technology -2024
Workshop-EST-2024*



July 06, 2024

*Multipurpose Hall, Training School
Hostel, Anushaktinagar, Mumbai*



**Souvenir cum bulletin of
Indian Society for ElectroAnalytical Chemistry
Volume 6, Issue 2, 2024**



**Souvenir Cum Bulletin of
Indian Society for ElectroAnalytical
Chemistry**

*The Workshop On
Electrochemical Science & Technology-2024*

July 06, 2024

Multipurpose Hall, Training School Hostel

Anushaktinagar,

BARC, Mumbai

Editors

A. K. Satpati

C. N. Patra

**Organized by
Analytical Chemistry Division
Bhabha Atomic Research Centre &**



Indian Society for ElectroAnalytical Chemistry

Mumbai, India

www.iseac.org.in

Workshop-EST-2024

*Analytical Chemistry Division, Bhabha Atomic Research
Centre and
Indian Society for Electro Analytical Chemistry
(ISEAC)*

Welcomes you to the

The Workshop On

Electrochemical Science & Technology-2024

July 06, 2024

ISBN No. 978-81-961201-3-9
August, 2024 (Volume 6, Issue 2, 2024)

Printed by

Shradha Xerox Centre

Shop No 4, Arjun Centre, Govandi Station Rd,
Deonar, Govandi East, Mumbai,

Maharashtra 400088

Phone: 022 2558 7060



Indian Society for ElectroAnalytical Chemistry

Reg. No. MAH/MUM/1173/2006 GBBSD

(Website: www.iseac.org.in; Email: electrochembarc@gmail.com)

Since foundation, the Society has evolved magnificently to represent a truly National Organization and at present, it comprises more than 350 life-members from different parts of India and Overseas. The Executive committee of ISEAC, which manages the activities of ISEAC, is being elected triennially by all the members of ISEAC.

International Events organized by ISEAC:

ISEAC organizes International Conferences, Discussion Meets and Workshop cum Symposium on Electrochemistry and allied topics in association with the Departments of Government of India, International Society of Electrochemistry (ISE) and other Scientific Organizations and Industries. ISEAC has organized several national and International Events in India.

- 1. International Conference on Electrochemistry in Industry Health and Environments (EIHE 2023) at DEA Convention Centre, Anushaktinagar, Mumbai during February 7-11, 2023.*
- 2. International Conference on Electrochemistry in Industry Health and Environments (EIHE 2020) at DEA Convention Centre, Anushaktinagar, Mumbai during January 21-25, 2020.*
- 3. Discussion meeting on Spectro electrochemistry (DM-ISEAC-2022) at Multipurpose hall, Training School Hostel, Anushaktinagar, Mumbai 400094 on 16-07-2022*
- 4. International Conference on Electrochemistry in Advanced Materials, Corrosion and Radiopharmaceuticals (CEAMCR-2018) at DEA Convention Centre, Anushaktinagar, Mumbai during February 15-17, 2018.*
- 5. Twelfth ISEAC Discussion Meet in Electrochemistry (12th ISEAC-DM-2016) held at The Acres Club, Chembur, Mumbai during December 7-8, 2016.*
- 6. Eleventh ISEAC International Discussion Meet on Electrochemistry and its Applications (ISEAC-DM-2014) held at Hotel Radisson Blu, Amritsar during February 20-25, 2014.*
- 7. Fifth ISEAC Triennial International Conference on Advances and Recent Trends in Electrochemistry (ELAC-2013) held at Sitara Hotel, Ramoji Film City, Hyderabad during January 16-20, 2013.*
- 8. ISEAC International Symposium cum Workshop on Electrochemistry (ISEAC-WS-2011) at Cidade de Goa, Dona Paula, Goa during December 7-10, 2011.*

9. *Fourth ISEAC International Discussion Meet on Electrochemistry and its Applications (DM-ISEAC-2011) at Mascot Hotel, Thiruvananthapuram, Kerala during February 7-10, 2011.*
10. *Fourth International Conference on ElectroAnalytical Chemistry and Allied Topics (ELAC-2013) at Toshali Sands, Puri, Orissa during March 16-18, 2010.*
11. *Discussion Meet on ElectroAnalytical Techniques and Their Applications (DM-ELANTE-2008) held at Tea County, Munnar, Kerala during February 25-28, 2008.*
12. *Third International Conference on ElectroAnalytical Chemistry and Allied Topics (ELAC-2007) at Toshali Royal View Resort, Shilon Bagh, Shimla during March 10-15, 2007.*
13. *Discussion Meet on Role of Electrochemistry in Biosensors, Nanomaterials, Fuel Cells and Ionic Liquids (DM-BNFL-2006) held at Bhabha Atomic Research Centre, Mumbai during September 24-25, 2006.*
14. *Discussion Meet on Coulometry (DM-COUL-2005) at Bhabha Atomic Research Centre, Mumbai on May 5, 2005.*
15. *Second International Conference on ElectroAnalytical Chemistry and Allied Topics (ELAC-2004) held at The International Centre, Dona Paula, Goa during January 18-23, 2004.*
16. *Workshop cum Seminar on ElectroAnalytical Chemistry and Allied Topics (ELAC-2000) held at Bhabha Atomic Research Centre, Mumbai during November 27 – December 1, 2000.*

Objectives of ISEAC:

- *Promote the growth of Electrochemistry in India.*
- *Provide a common world-wide platform to the experts, scientists and scholars working in the area of Electrochemistry and its Allied Sciences.*
- *Disseminate scientific and technological knowledge in the area of Electrochemistry to advance both national and international collaborations.*
- *Share the information on Electrochemistry with other International Societies viz. European Society for Electroanalytical Chemistry (ESEAC), Society for Electroanalytical Chemistry (SEAC) and International Society of Electrochemistry (ISE), Bioelectrochemical Society (BES).*
- *Work in harmony with other Indian Electrochemical Societies viz. Society for the Advancement of Electrochemical Science and Technology (SAEST) based at CECRI, Karaikudi and Electrochemical Society of India (ECSI) based at Indian Institute of Science, Bengaluru.*

- *Provide incentive by way of awards to researchers for the best thesis, the best paper published in the journal and the best paper presented in National and International Conferences/Symposia.*
- *Encourage young as well as experienced Indian researchers for participation in International Electrochemistry Conferences by providing partial funds, if possible.*

Procedure to join ISEAC:

ISEAC has the provision for individual to join as Life-members and for company to join as Corporate Member. The Life-membership fee w.e.f. April 1, 2011 is Rs. 4000/- (Rs. Four thousands only) for Indians and € 300/- (Euro three hundred only) for others. The Fee has to be transferred electronically (NEFT or wire transfer) to ISEAC Bank Account and then you have to sign-up through “Join ISEAC as Life-Member” icon available on www.iseac.org.in with the fund transfer details.

Name of Bank: State Bank of India, BARC Branch, Mumbai-400 085, India

Branch code: 1268

Beneficiary name: Indian Society for ElectroAnalytical Chemistry (ISEAC)

Account number: 34209997299

BIC (Swift Code): SBININBB508

IFSC code (for within India): SBIN0001268

Please contact us for any further information:

The Secretary,

Indian Society for ElectroAnalytical Chemistry (ISEAC)

Analytical Chemistry Division,

Bhabha Atomic Research Centre, Trombay,

Mumbai – 400 085, India

Email: electrochembarc@gmail.com;

web.: www.iseac.org.in

Phone: +91-22-2559 0744 (office hours only); 8369268926 (after office hours)

You are Welcome to Join

ISEAC

EST – 2024

Workshop

on

Electrochemical Science and Technology
July 06, 2024

Organized by

Analytical Chemistry Division
Bhabha Atomic Research Centre



In association with

The Indian Society for ElectroAnalytical
Chemistry



Venue

Multipurpose Hall, Training School Hostel,
Anushaktinagar, Mumbai 400094 India

For more information visit us at
www.iseac.org.in

Scope

The Workshop, EST-2024 is intended to discuss the basic and applied aspects of the electrochemical science and technology in recent scientific problems. Electrochemical science and technologies holds key to sustainable future with emerging energy technologies, catalysis, and miniaturized in-vitro biological investigations. The present Workshop, EST-2024 will emphasize both on the fundamental and applied nature of this important area of research. It will mainly focus on the following sub-topics:

- Energy Storage & conversion (Battery, supercapacitor, fuel cell)
- Electroanalytical Chemistry, Sensors, Biosensor
- Electrocatalysis
- Environmental Science and Technology
- Spectro- and Photo-electrochemistry
- Instrumentation

Organizing Committee

Dr. Awadhesh Kumar, CG, BARC, Chairman
Dr. C. N. Patra, ACD, BARC, Co-Chairman
Dr. A. K. Satpati, ACD, BARC, Convener
Dr. P.K. Mohapatra, RC& IG, BARC
Dr. P.D. Naik, Ex-BARC
Dr. A.C. Bhasikuttan, RPCD, BARC
Dr. N. Choudhury, ChD, BARC
Shri K. Bhanja, HWD, BARC
Dr. Amrit Prakash, RMD, BARC
Shri A.K. Singh, UED, BARC
Dr. S. K. Ghosh, MP&CED, BARC
Dr. V. T. Aher, RRS, BARC
Prof. (Smt.) S. Chatterjee, ICT, Mumbai
Prof. Kothandaraman R, IITM
Prof. T.N. Narayanan, TIFR, Hyderabad
Prof. Arnab Dutta, IITB
Prof. V.G. Anand, IISER, Pune

Registration is free and limited based on advance request

Contact: electrochembarc@gmail.com

Content

Serial No.	Title and Authors	Page
1	Activities of Electrochemistry in Development of Analytical Methods, Instrumentations and in Energy Harvesting Research Srikant Sahoo, Sudipa Manna, Mohsin Jafar, Milan Kumar Dey, Prem Kumar Mishra and Ashis Kumar Satpati*	2-58
2	Applications of atomic force microscopy in modern biology Tathagata Nandi and Sri Rama Koti Ainavarapu*	59-77
3	Rational Designing of Nickel-Iron Containing Layered Double Hydroxide [NiFe@LDH] Electrocatalysts for Effective Water Splitting Madasu Sreenivasulu, and Nagaraj P. Shetti*	78-116
4	Perspective of Electrochemical Biosensors in Agriculture Jitendra Kumar*, Bhanu Prakash Sandaka, Kuber C. Bhainsa, and Anand D. Ballal	117-128
5	Comparative Electrochemical Studies of Binary Metal Oxide Nanocomposite on GCE and NF Substrates for Supercapacitor Application Bhakti G. Thali and Rajesh M. Kamble*	129-143

Activities of Electrochemistry in Development of Analytical Methods, Instrumentations and in Energy Harvesting Research

Srikant Sahoo, Sudipa Manna, Mohsin Jafar, Milan Kumar Dey, Prem Kumar Mishra and Ashis Kumar Satpati*

Analytical Chemistry Division
Chemistry Group
Bhabha Atomic Research Centre
Trombay, Mumbai 400094
*email: asatpati@barc.gov.in

Abstract

Present article is focused in providing the perspective of the activities on electrochemistry and electrochemical science and technology carried out in Analytical Chemistry Division towards the work program of the Department. The electrochemistry related activities started in 1950's under in the Department. In absence of the current days spectroscopic techniques the electrochemical techniques provided the alternate and cost-effective version available during early days of the development of analytical chemistry. In addition to provide the quantitative analytical supports to the Divisional work program the activities have important contribution in the research and developments of important technical issues of materials science. Present article has outlined some of the activities of electrochemical research In Analytical Chemistry Division towards the development of analytical methods for heavy metal ions, methods for biomolecules, interfacial research in photoelectrochemistry and renewable energy systems.

1. Introduction

The research on electrochemical techniques in has been started in 1950,s along with the inception of Analytical Chemistry Ection. The technique has been extensively used in the determination of uranium, thorium, several rare earth elements and transition metal ions and halides to support the activities of the Department. The activities that are well documented in terms of publications are cited in the present article. In an historical perspective, the electrochemical techniques are evolved internationally to determine the composition of gun powder during the world war after the discovery of polarography by Dr. Jaroslav Heyrovský in current days Czeck Republic. The technique has been very well incepted in the electrochemistry activity of the Analytical Division for the determination of metal ions. Polarographic techniques were having unique advantage of low-cost instrumentations and their capability of generating kinetics and mechanistic information of the chemical systems. The contribution of the technique towards the Chemistry activities in the Centre has been presented in the present article with subdivision of the progress in different directions in development of analytical methods, development of electroanalytical instrumentations, investigations of interactions in biochemical systems and the contribution in solar energy harvesting and electrical energy storage systems.

2. Electrochemistry Activities during its inception

During its inception in late 1950's the experiments used to be carried out using potentiometer, pH meter and conductivity meters. Later, the current measurements were carried out using the inception of lamp and scale galvanometer with the application of potentials through analogue potentiometers. The dropping mercury electrode was used the analytical

measurements. Some of the works which may be included for the early days of developments are include. The method for selective extraction of Beryllium was developed, in the absence of sufficient literature, achieving the desired extraction efficiency was challenging. Extensive work on the measurement and adjustment of pH of the media with varied solution compositions was carried out and the efficient extraction of Beryllium with extraction efficiency of 70 to 80 % could be attained. In early days the of electrochemical experiments the Cambridge pH meter was used for such measurements[1]. The polarography of uranyl ion was recorded and published in way back 1959 using the manual set up and homemade fabricated cell. The polarographic wave as published is shown in Figure.1[2, 3].

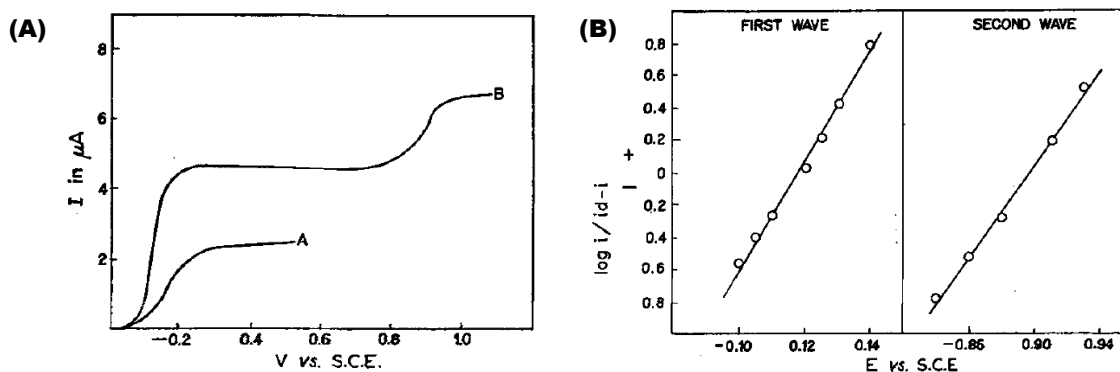


Figure .1 The Polarographic plot of uranium recorded way back in 1959 (A) along with the mechanistic Criteria for investigating the mechanism of the process (B) [3]

The two-wave pattern of the reduction of uranyl ion was obtained in ammonium thiocyanate media along with perchloric acid. The reversible nature of the reduction pattern was established with first reduction as two electron transfer process and the second reduction as the single electron transfer process, the mechanism of the electrochemical process was proposed to be due to the reduction of U(VI) to U(IV) and reduction of the U(IV) to U(III). Information about the disproportionational nature of the reduction wave of U(IV) to U(III) was

observed and discussed. The analytical method was established from the reduction peaks of uranium. Polarography of uranium was also investigated in several other media.

Conductivity meters were available during early days of electrochemical work and contributed well in the thorium extraction research. The complexation of Th and the mechanism of the complexation with EDTA was established using conductometric titration[4]. The conductometric titration along with polarographic measurements was extended for other metal ions as well for their determination and also investigation of basic kinetic parameters[5, 6]. In addition to conductometry, the potentiometry and potentiometric titration was used in analytical determination and also obtaining basic information of redox systems[7]. Voltammetry was introduced with solid electrode systems as alternate to mercury electrodes[8]. The cathode ray polarography was available during that time and bimetallic electrode system was investigated [9].

Zinc has been one of the important transition metal elements very well suited using polarographic measurements. The element was investigated for its complexation in several different matrices pertaining to its determination and the investigation of its toxicity[10-12]. Meanwhile, with the advancement of instrumentation facilities the electrokinetic parameters of several chemical systems were investigated[11, 13-15]. Important contributions were made in relation with analytical determination and solving the problem of materials science and technology with strong interaction with the materials science activities of the Centre. During 1908's the instrumentations have been improved with the availability of potentiostat and associated automated dropping mercury electrode systems along with the facility to fabricate several customized electrode systems. Electrochemical systems and power suppliers were fabricated in house during this period for different customized measurements. Experiments on low energy nuclear reaction (LENR) or popularly known as the cold fusion, was given immense priority. Several scientists of Electrochemical Methods Section of Analytical Chemistry

Division have contributed in the activity with a priority[16]. The cylindrical Pd electrode was used as cathode and Pt as anode for the electrolysis experiments D₂O media with LiOD as the electrolyte. Presence of the tritium activity was reported by confirmation through several control experiments.

The analysis of minerals was one of the important activities for their metal ions content, polarographic techniques were adopted for the analysis of metal ions like, Pb, Cu, Cd, Zn, and Ni in the minerals like monazite and zircon. In one of the well documented development of method, the analysis of Pb in zircon sample has been reported through improvised dissolution and selective voltametric determination procedure[17]. The determination of impurities in ultrapure gallium has been important activities on electrochemistry where several transition metal elements as impurities were determined, the development of method and determination Cr in ultrapure Ga sample was reported[18].

Hydrogen charging and permeation of hydrogen through different nuclear structural material was one of the important activities where the major contribution has been made. Hydrogen was charged using the material of interest as cathode. The correlation of hydrogen charging current, hydrogen concentration in structural material and the solution conditions were carried out to ascertain the detrimental effect of hydrogen in structural stability of the materials [19, 20]. Several analytical methods were developed for analytical determination and also investigation of kinetic parameters in metal ion and also in biological systems during this activity period.

3. Activities utilizing the recent instrumentations

In the current century, significant uplifting of the activities on electrochemistry has been done using modern electrochemical facilities and newly introduced activities for the analytical

measurements, investigation of corrosion and their inhibition and investigation of the interfaces. Determination of Pd, Cr, Nitrites, halides, Pt, Rh, Hg, U, As, peroxides etc. in complex matrices for the important applications in Departmental and societal requirements are developed and the methods were utilised for analytical measurements [21-25].

The potential of the electrochemical techniques in the investigation of the interfacial processes have been carried to its outmost capacity. The metallurgical aspects of cold rolled and heat treated SS304 is important, the corrosion aspects of the treated SS304 were investigated, the hydrogen uptake and the related corrosion property of zircaloy-2 and zircaloy-4 were investigated, indicating impervious passive films and their possibility of bleaching under different solutions and polarization conditioning[26, 27]. The inhibition of corrosion and the binding mechanism of the inhibitors with active functional groups for binding with metal and alloy surfaces were investigated with thermodynamics and kinetics parameters.

The electrochemical instrument, potentiostat and galvanostatic with features like, linear sweep and pulse voltametric techniques was developed and used in the Division in several important electrochemical analysis. The photograph of the inhouse developed electrochemical system is shown in Figure 2.

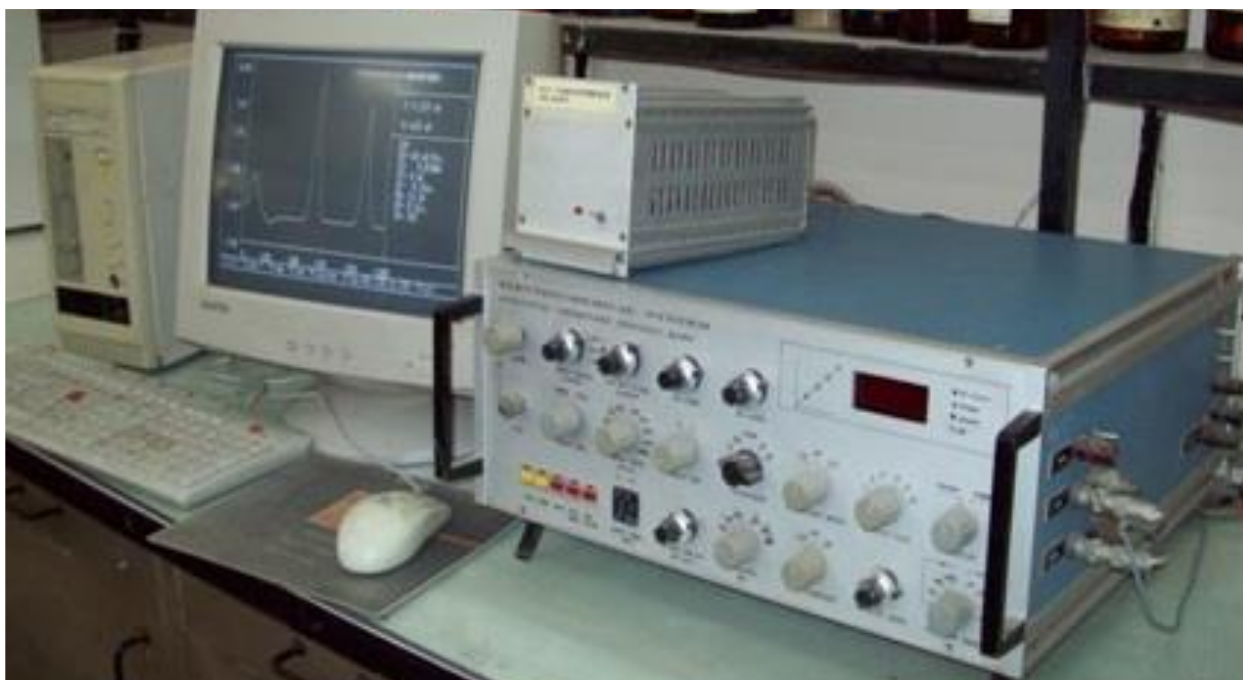


Figure 2. The inhouse developed computer controlled electrochemical system equipped with linear and pulse voltametric techniques.

Instrumentations and related technologies are developed for the determination of dissolved oxygen in water required in nuclear and in several chemical industries and environmental monitoring. It requires continuous monitoring of dissolved oxygen to keep the corrosion of the structural material under control and thus to improve the life of the plant. In nuclear industry, the specification of dissolved oxygen in coolant water is as low as 5 ppb. Determination of the dissolved oxygen is also important in industrial waste, sewage and water bodies. Determination of dissolved oxygen in potable water is an important water quality parameter. Present model has been designed for the continuous monitoring of dissolved oxygen under flow condition. The reduction current of oxygen is the measurable parameter for the determination of dissolved oxygen. The current flows due to this process is measured using the electronics device and the measured current is calibrated with respect to the dissolved oxygen concentration. Sensor displays the reading of dissolved oxygen concentration in ppm/ppb units, the instrument can be used for continuous monitoring and also batch mode of applications. It

has been developed with completely indigenous materials and technology. The picture of the dissolved oxygen sensor is shown in Figure 3. The technology has been published over BARC website, and the technology has been transferred to four companies so far.



Figure 3. Picture of the dissolved oxygen monitor which has been developed and technology has been transferred to several companies, Technology code: CH32ACD, Website, <http://barc.gov.in/technologies/dom1/index.html>.

4. Electroanalytical methods over modified electrodes

In the recent years, electrochemical sensing of toxic metal ions in the complex matrices at wide concentration range has attracted enormous impetuosity in the environment, human health as well as geochemical point of view. Electrochemical in hyphenation with the spectroscopic and microscopic techniques are utilised in characterization of biological interfaces, bacteria, antibiotics, glucose, anticancer drugs etc.[28, 29].

The quantification of the metal ions in trace and ultra-trace level is a challenging task among the scientist and researcher. Heavy metals leaking to the environment are the most representative pollutant due to the human activity and threatening the human health by inducing various diseases. The heavy metals are non-biodegradable, universally distributed and accumulated in the biosphere through the alimentary chain. These metal ions enter into the living organisms through water, air or food chain and alter the biochemical life cycle leading to a greater risk to the human health and the environment. Uranium is one of the important actinides in view of its use as a fuel in nuclear industry. Besides its utility as nuclear fuel, geochemical pathways of the element are extremely important due to its long-term toxic implications. Therefore, determination of uranium has immense importance in relation to the nuclear industry and environment [30-32]. There have been methods of determination of toxic metal ions such as, gas chromatography-atomic fluorescence spectrometry and atomic absorption spectrometry[33-38]. Other commonly used methods for the determination of total mercury are: cold vapour atomic absorption spectrometry (CVAAS), inductively coupled plasma mass spectrometry (ICP-MS)[39, 40]. All the methods mentioned require complicated instrumentations and also involve high operational cost. Voltammetric techniques represent important method with high sensitivity and low operational cost and have the possibility of portable instrumentations for onsite determination.

The bare electrodes are easily contaminated by the unwanted species or impurities present in the solution, which is detrimental to the determination of actual analyte due to the memory effect, additionally the unmodified electrodes are less selective and sensitive. The fabrication of the modified electrode is being carried out for a particular analyte of interest, which is not possible by using bare electrode. The efficacy of conventional solid electrode or

unmodified electrode-based sensors is often hampered by a gradual fouling of the surface due to adsorption of large organic surfactants of reaction products. Sometimes, the detection of particular analyte of interest is not feasible by using bare solid electrodes due to their slow electron transfer kinetics occurs at the electrode surface. Modified electrodes have been used over conventional bare electrodes because it has various interesting properties such as, fast electron transfer kinetics, enhance catalytic property and provides larger surface area, leads to the increase in the sensitivity as well as selectivity of the method.

In electrode modifications, thin film and Metal nanoparticles are of great interest due to their unique optical, magnetic and catalytic property and high electrical conductivity in nature. Gold nano particles (AuNPs) have shown high sensitivity for mercury by measuring the anodic stripping peak due to the obvious reason of high affinity of mercury towards gold [41-43]. There are some reports on the gold nanoparticle modified electrode for the determination of mercury either on the carbon electrode or on screen printed electrode[44-50]. However, preparation of the stable arrays of gold nanoparticle and easy regeneration of the substrate for regular determination of mercury is still challenging. Bismuth is a good candidate for modifying the electrode surface for various analytical application because bismuth is a soft conducting material, enhances the diffusion kinetics, have high potential window in the cathodic side and it is not required of removing dissolved oxygen during stripping analysis. Additionally, bismuth is an environmentally friendly material due to its less toxic in nature and also inexpensive material[51-57]. Bi film electrode (BFE) on the carbon paste electrodes is very well suited in the stripping voltammetry experiments, the carbon paste electrode reduces the possibility of the memory effect due to its easy renewability [58-60]. The major concern in stripping voltammetry, especially using modified film electrodes are the interference and the fouling effect of the electrode surface due to surfactants. Nafion film a cation exchanger, an

ideal permselective membrane has been tested in stripping voltammetry, useful in the reduction in interference due to surfactants. In recent times, due to the toxicity of mercury, mercury drop electrodes are being avoided in the stripping as among all the heavy metal ions, toxicity of mercury is more severe than the others. Mercury exhibits a very complex behaviour in the food chain and in the human body system [61, 62]. Mercury and copper have been extensively used in industries and there are enormous concerns of contamination of these metal ions in the environment through the industrial activities. All the heavy metal ions, beyond certain concentration levels are highly toxic to the environments; Hg is important toxic elements in the list. In the body system Cu generally present in the bound form with ceruloplasmin and non-toxic. The free Cu in the body system causes toxicity as it generates reactive oxygen species and damages proteins, lipids and DNAs[63]. Stripping voltammetry is one of the most important methods of determination of Cu in wide concentration ranges using modified electrodes.

Bi-film was deposited on the glassy carbon electrode and carbon paste electrode (CPE) by using stripping voltammetry[58-60, 64-66]. However, the easy renewability of CPE is a better choice for the present purpose compared to glassy carbon electrode. It has been observed by previous researchers that a strong stripping peak due to Bi was observed before Cu peak, which is detrimental to the appearance of Cu stripping peak on bare Bi film electrodes [52, 67]. There was one report based on the decrease in the Bi stripping peak for the determination of Cu using bare Bi film electrodes [52]. We also have reported the determination of Cu from the decrease in the Bi stripping peak on bare Bi film electrode [67] and a direct determination of Cu using Bi-Graphene composite electrode has been proposed [41]. There was one report based on the decrease in the Bi stripping peak for the determination of Cu using bare Bi film electrodes [52]. We also have reported the determination of Cu from the decrease in the Bi stripping peak on bare Bi film electrode[67] and a direct determination of Cu using Bi-

Graphene composite electrode[68]. Gold has been incorporated into the Bi film so that the stripping peak due to Cu could be observed. Gold has the strong affinity towards mercury thus the Bi-AuNPs composite material would be the ideal choice for the simultaneous determination of Cu and Hg.

Additionally, it has been reported that the nanoparticle arrays have increased the effective mass transport and also increased the signal to noise ratio of the analytical measurements[69-71] . Merged diffusion layers of nanoparticle modified electrodes also reduced the requirement of active materials to obtain similar or enhanced response to the whole electrode. There are a few reports on the gold nanoparticles (AuNPs) modified electrode for the determination of mercury either on the carbon electrode or on the screen-printed electrode[41, 44]. In our investigation we have employed the simple electrodeposition method for the deposition of AuNPs over the carbon paste electrode surface to avoid any excess chemical processing in the method. Easy regeneration of the carbon paste electrode has the advantage in the procedure. Interference effects due to some of the commonly occurring metal ions and surfactants were investigated. One paper reported the modified electrode using EDTA-like films for the simultaneous determination of Cu and Hg[72] . In a recent publication heavy metal ion were determined using bismuth nanotube modified glassy carbon electrode[73]. Other than analytical application Au and Bi₂O₃ nanocomposite modified electrode was also applied for photocatalytic decomposition of dyes[74]. Thus, it is interesting to investigate the applicability of AuNPs arrays embedded onto the Bi film on CPE for the simultaneous determination of Cu and Hg.

Further, the analytical method has been developed for the determination of uranium (U) in ground water and sea water using Hg thin film modified multiwall carbon nanotube incorporated carbon paste electrode. Parameters for the optimal sensitivity and the minimal usage of metallic mercury have been optimized. Conditions and the mechanism of the

adsorption pre-concentration process were investigated. The thin film electrode also provides better physical stability compared to the mercury drop electrode for onsite application. The different modified electrodes developed under present investigation was applied for the determination of metal ions such as Hg, Cu and U in different water samples and soil samples.

4.1. Electrochemical characterization of the modified electrodes

A. AuNPs modified electrodes

The electronic property of the AuNPs modified electrode was investigated in 1mM potassium ferro-cyanide solution containing 0.1M KCl using cyclic voltammetry measurements. Reversible response of ferrocyanide oxidation was observed (corresponding figure is not shown). Electrochemical response of ferrocyanide oxidation on AuNPs modified CPE substrate was found to be sharper compared to bare CPE surface. Cyclic voltammetry response remained reversible at scan rate of 500 mVs⁻¹ where as in the case of bare CPE the peaks were comparatively broadened. Anodic peak current on AuNPs modified electrode was 1.7 times higher than the bare carbon paste electrode when compared at the scan rate of 500 mVs⁻¹. Thus, the additional current was due to the increase in active surface area on deposition of gold nanoparticles over the carbon paste electrode surface.

Resistance and capacitance behaviour of the bare CPE and the AuNPs modified CPE were carried out from the electrochemical impedance measurements. Experiments were carried out at an applied potential of 0.3 V with AC frequency from 10 kHz to 10 mHz and amplitude of 10 mV. The Nyquist plot has shown RC behaviour with Warburg component. Charge transfer resistance on the bare carbon paste electrode surface was around 1.9 times higher compared to the AuNPs modified electrode surface.

B. Bi-Au film modified electrodes

The investigation of the interfacial charge transfer property of the CPE/Bi-AuNPs modified electrode was carried out using electrochemical impedance measurements in 0.1 M acetate buffer solution of pH 4.5. Impedance measurements were recorded at a single frequency of 100 Hz with varying potentials. It was observed that the capacitance of the Bi film modified CPE was lowest. Capacitance of the CPE/Bi-AuNPs composite was also less, which is useful for the application of the composite electrode in analytical measurements as modified electrode. The CPE/AuNPs composite electrode has shown very high capacitance, significantly higher than the other two electrodes. The lower capacitance of the CPE/Bi-AuNPs composite electrode is beneficial to have lower background in stripping analysis.

C. Hg- film modified electrode

Electrochemical impedance measurements were carried out to have an explanation about the adsorption process of uranium-(chloranilic acid) CAA complex on the MTMCPE surface. From the frequency scan at open circuit potential, Nyquist plot was obtained. Bare CPE was observed to show very high charge transfer resistance at open circuit potential. On deposition of mercury thin film on the CPE surface, the charge transfer resistance was observed to reduce by almost two orders of magnitude. Contribution due to the diffusion was observed at the lower frequency region. The Nyquist plot, characterized as a suppressed semicircle could be due to the uneven nature of the surface. Nature of the Nyquist plot was not altered on mercury film deposition.

5. Voltammetric investigation of the Modified electrodes

A. Voltammetric response Hg using AuNPS modified electrode

The determination of Hg was carried out using AuNPs array modified carbon paste electrode in a deaerated 0.1 M NaNO₃ and KCl solution by differential pulse anodic stripping voltammetry. The electrochemical parameters were optimized such as: deposition potential -0.6 V, deposition time 300 s, pulse amplitude 25 mV, step potential 25 mV and anodic scan from 0 V to 0.6 V. As reported previously, the mixture of NaNO₃ and HCl of 0.1 M concentration provided better stripping response of mercury[75, 76]. Better stripping response in such supporting electrolyte media was due to the predominant formation of Hg₂Cl₂ and HgCl₂ in presence of chloride ions. The anodic stripping peak due to mercury was observed at potential around 0.45 V shown in Figure. 4. Corresponding calibration plot due to the subsequent addition of Hg standard was shown in the inset of Figure 4. The sensitivity of the measurement was $3.47 \times 10^{-8} \text{ A}/\mu\text{gL}^{-1}$ and the correlation coefficient of linear regression as 0.998. Standard deviation in current measurements of six measurements at $1 \mu\text{gL}^{-1}$ concentration was obtained as $2.77 \times 10^{-9} \text{ A}$. Three sigma detection limit was obtained as $0.24 \mu\text{gL}^{-1}$. In the present method AuNPs modified CPE was fabricated using very easy way of constant potential deposition. It was also easy to regenerate the carbon paste electrode substrate for repeated application. Detection limit of the present method was comparable to reported results.

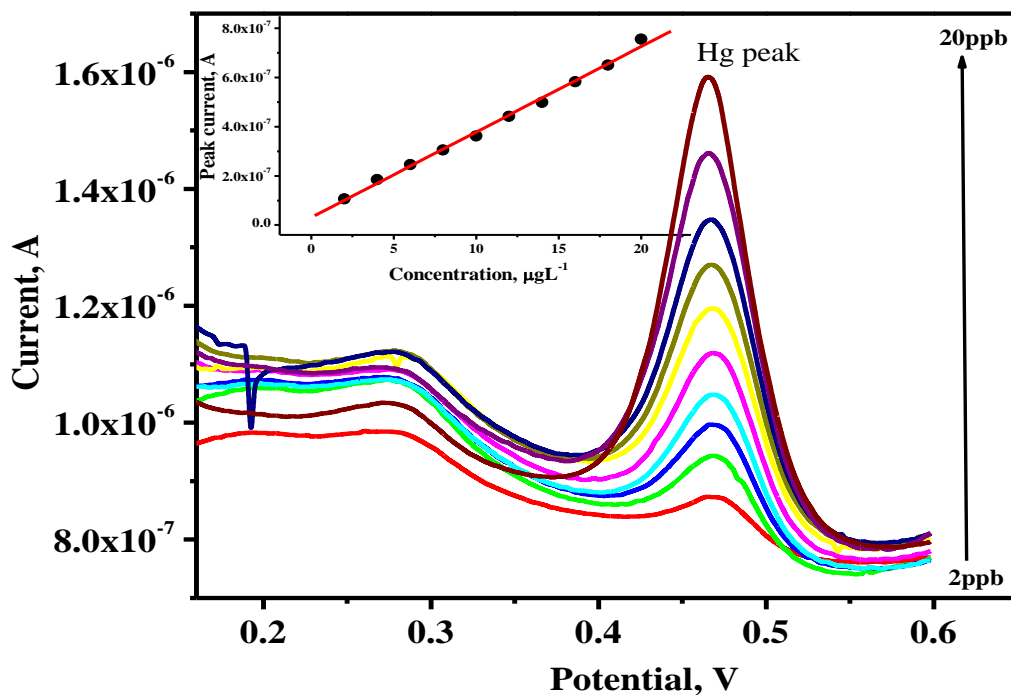


Figure.4. Voltammetric response of Hg with successive addition of $1 \mu\text{g L}^{-1}$ (ppb) of Hg^{2+} in 0.1 M NaNO_3 and KCl as the supporting electrolyte media. Inset: corresponding linear calibration plot with the fitted line

Interferences

The Possible interferences of Ag^+ , Cu^{2+} , As^{3+} and Fe^{2+} were evaluated with the stripping peak of the mercury. Cu^{2+} , Fe^{2+} and As^{3+} , did not interfere with the stripping peak even ~ 300 times higher concentration to Hg^{2+} . The stripping Voltammogram of mercury was recorded containing a solution of $20 \mu\text{g L}^{-1}$ of mercury, and then Ag^+ was added into the solution. The mercury stripping peak was decreased drastically by the addition of Ag^+ in the solution. With the addition of $100 \mu\text{g L}^{-1}$ of Ag^+ in the solution, mercury stripping peak was suppressed almost completely. The stripping peak was reappeared when 0.3 mM Au(III) in the solution was added and it is shown in Figure.5(a). Thus, from the interference pattern it is indicated that metallic Ag interacts with the gold nanoparticles to form solid solution which becomes inactive to

mercury. This is an important issue on the determination of mercury in water samples. In a silver containing sample, amount of AuNPs deposition has to be higher to obtain the stripping peak of Hg. On further addition of Au in the solution, fresh gold nanoparticles are formed; the substrate regained its activity towards mercury. Likewise, Fe(II) was added successively in the test solution, and the peak observed with the addition of Fe(II) in the solution was not proportional to the addition of Fe(II). The presence of Fe (II) did not interfere with Hg determination up to a 5000 $\mu\text{g/L}$ concentration level, as shown in Figure.5(b)

Additionally, the interference due to some of the common surfactants, triton X-100 (TX100), sodium dodecyl sulphate (SDS), and cetyltrimethyl ammonium bromide (CTAB) was investigated. A deposition time of 150 s was used in these cases. With the addition of neutral surfactant, TX100 in the test solution the stripping peak was reduced initially, with further addition of TX100 concentration, the peak height was increased, shown in Figure. 5(c). Maximum peak current was observed with 0.5 mM TX100 concentration, and then it was reduced with further addition of TX100. The base line was deformed beyond 0.5 mM TX100 concentration. In the case of SDS, the stripping peak was increased marginally at initial additions of up to 0.1 mM concentration, shown in Figure 5(d). With further addition of SDS beyond 0.2 mM concentration, the base line of the voltammogram was deformed and the stripping peak height was reduced. CTAB has strong interference with the measurements; the stripping peak vanished even with 1 μM concentration of CTAB in the stripping solution (plots not shown). TX100 being the neutral surfactant might entangle mercury ions through its surfactant chains and increased the surface concentration of mercury at the electrode surface. On further addition of TX100, higher electrode coverage by surfactant molecules reduced the peak current increased the capacitance due to adsorption. SDS, being an anionic surfactant, does not have coulomb interaction towards the electrode surface during deposition, thus did not interfere heavily on the mercury stripping peak. Being cationic in nature the surfactant

molecules in CTAB attracted towards the negatively polarized electrode during electrodeposition process, the active area of the electrode will be covered by the surfactant molecules for deposition and stripping of mercury. Complexation property of SDS with Hg(II) was used for the solid phase extraction and pre-concentration of mercury for its high sensitive determination[77, 78]. Beyond a certain concentration, SDS and CTAB were reported to be interfered with the potentiometry sensing of mercury[79]. Thus, it is important to remove any cationic bulky molecule from the test solution in voltammetric determination of mercury.

The developed method was used to determine mercury in the soil samples using the AuNPs modified carbon paste electrode. The results obtained from the present method was validated with the total mercury analyzer based on thermal decomposition and atomic absorption technique. Analysis results were agreed well between the two methods of determination. The developed method was found suitable for the detection of Hg in water and soil samples.

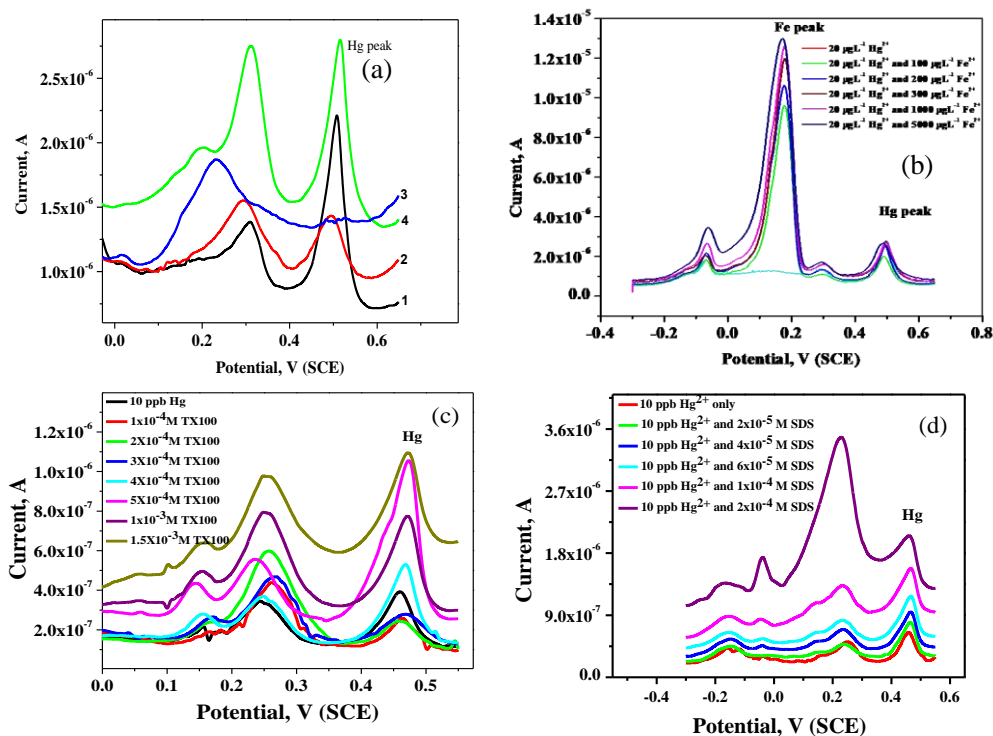


Figure.5. (a) Adsorptive stripping voltammetric response in 0.1 M NaNO₃ and KCl as the supporting electrolyte media (1) 20 μg L⁻¹ of Hg²⁺, (2) and (3) 50 , 100 μg L⁻¹ of Ag, and (4) addition of 3x10⁻⁴ M Au , (b) Effect of Fe(II) on stripping peak of 20 μg L⁻¹ Hg(II), (c) Stripping voltammetric peak of 10 μg L⁻¹ Hg (II) in the presence of different concentrations of TX100, (d) Stripping voltammetric peak of 10 μg L⁻¹ Hg (II) in the presence of different concentrations of SDS.

B. Voltammetric response Hg and Cu using Bi-Au film modified electrode

The simultaneous determination of Cu²⁺ and Hg²⁺ were carried out using CPE/Bi-AuNPs electrode in 0.1M acetate buffer medium at optimized electrochemical conditions such as accumulation potential -0.5V, accumulation time 200sec and pH of the buffer solution 5. and it is given in the Figure. 6(a). voltammograms were recorded using CPE/Bi-AuNPs electrode with successive additions of Cu and Hg standard concentrations. The Peak positions of Cu and Hg were well separated and useful for their simultaneous determination. Stripping peak currents were increased with increase in the Cu²⁺ and Hg²⁺ concentration in the stripping solution. The peak positions of both the elements remained unaltered on successive addition of the standards. Calibration plot of Cu²⁺ followed the regression equation $i_p = 2.03 \times 10^{-8} C + 8.61 \times 10^{-10}$ with the correlation coefficient of 0.998 and standard deviation of 1.06×10^{-9} where C in μg L⁻¹ unit. The calibration plot of Hg²⁺ followed the linear regression equation as $i_p = 4.28 \times 10^{-8} C + 1.52 \times 10^{-11}$ with the correlation coefficient 0.996 and standard deviation of 4.02×10^{-9} where C in μg L⁻¹ unit. Three sigma detection limits of Cu and Hg were obtained as 0.16 μg L⁻¹ and 0.28 μg L⁻¹ respectively. Linear ranges for Cu and Hg are 5 to 25 μg L⁻¹ and 2 to 10 μg L⁻¹ respectively under the optimized experimental conditions.

Bi film produces strong stripping signal during anodic scanning process and it is difficult to separate the Cu stripping peak from that of Bi, due to which determination of Cu is

difficult on Bi film electrode. Proportional decrease of Bi-stripping peak with the addition of Cu was successfully attempted as an alternate way to determine Cu [52]. It would always be good idea to observe the direct electrochemical stripping response of Cu with its proportional increment with concentration. Interestingly, in the present case on simultaneous deposition of AuNPs and the Bi-films, the stripping response of Cu was shifted to positive potential and it was clearly observed. Cu has the stronger affinity to form inter-metallic with Au which has shifted its stripping peak towards more positive directions. Due to that, its stripping peak was well separated from the Bi-stripping peak. Stripping response of Cu and Hg was compared using three different electrodes; CPE/Bi, CPE/AuNPs and CPE/Bi-AuNPs and it is shown in Figure. 6. (b). It was observed that on CPE/Bi electrode, no stripping response due to Cu and Hg was observed. Though the stripping peak heights in the case of CPE/Bi-AuNPs modified electrode was only marginally higher than that of CPE/AuNPs, the base line was improved in the case of CPE/Bi-AuNPs composite modified electrode. Modified electrodes by AuNPs alone are applied for the determination of Hg[41, 44-47]. However, as seen in the present case the stripping response of Hg has improved due to the incorporation of Bi in the composite. Similarly, the stripping response of Cu could also be observed on AuNPs modified electrode. However, its stripping response was not proportional, as Cu never stripped back proportionally from the composite film. In the presence of Bi along with the AuNPs have increased conductivity of the individual particles and also the inter-particle conductivity. Incorporation of Bi has also improved the holding capacity of the material, which has produced proportional stripping response and enhanced the linear range.

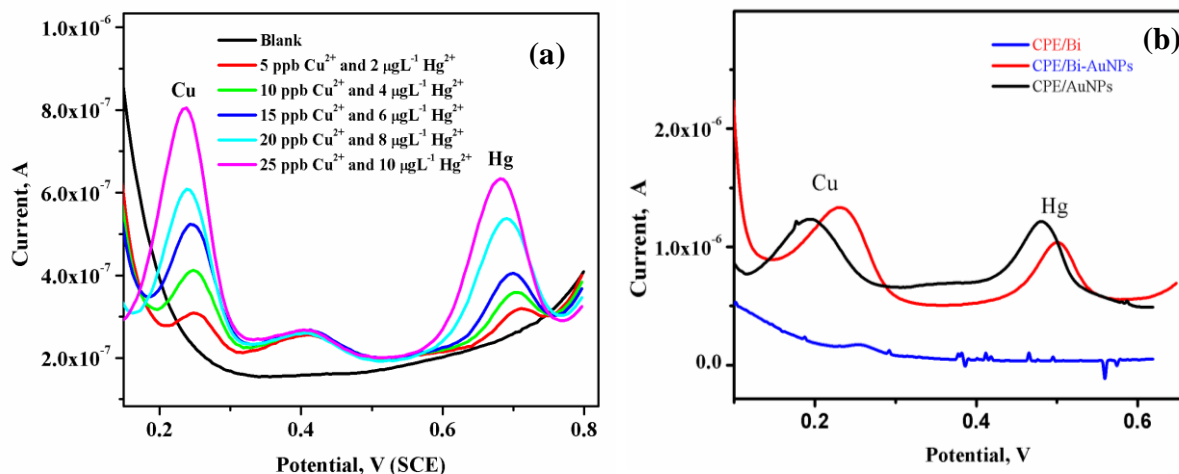


Figure.6. (a) Stripping response of Cu^{2+} and Hg^{2+} on different modified carbon paste electrodes, (b) Stripping response of Cu^{2+} and Hg^{2+} on different modified carbon paste electrodes.

In real water samples Cu remains at much higher concentration compared to Hg. To evaluate if the modified electrode could work in presence of Cu, voltammetric experiments were carried out using dummy sample containing $200 \mu\text{g L}^{-1} \text{Cu}^{2+}$, and Hg^{2+} was added successively in the solution. Corresponding plot is shown in Figure. 7(a). It was observed that the Hg stripping peak was increased proportionately and unaffected due to the presence of Cu^{2+} . Cu stripping peak was also unaffected with the addition of Hg^{2+} . This observation concluded that both Cu and Hg stripping responses remained unaffected due to the presence of other at high concentration. Reproducibility of the stripping responses was evaluated by recording voltammetric scans. Percentage of standard deviation for Cu^{2+} and Hg^{2+} were obtained as 3.6 % and 4.5% respectively for 6 repetitive measurements

Interference effects due to some of the commonly occurring metal ions Fe(III), Cr(VI), As(III), Ag(I), Pb(II), Cd(II), Zn(II), U(VI) were investigated on the stripping peak of $20 \mu\text{g L}^{-1} \text{Cu}$ and $8 \mu\text{g L}^{-1} \text{Hg}$. Except due to Ag(I) and As(III) no interference was observed from all the other metal ions up to 500 time higher concentration than Cu(II) and Hg (II). Ag(I)

interfered with both the Cu and Hg peaks. Effect of interference due to Ag(I) on the Hg stripping peak was shown in Figure.7(b). It was observed that Hg stripping peak was reduced with the addition of Ag(I) in the test solution from $50 \mu\text{g L}^{-1}$ Ag(I) concentration. Observable Hg stripping peak was observed with the addition of Ag(I) up to $1000 \mu\text{g L}^{-1}$. Hg stripping peak was recoverable with the increase in the gold content in the modified electrode. During preparation of the modified electrode a gold concentration of 100 times higher compared to the Ag(I) concentration is recommended to minimize the interference due to Ag(I) on the Hg stripping peak. Tolerance of Ag(I) on the stripping peak has increased due to the incorporation of Bi along with the AuNPs. As only AuNPs modified electrodes were heavily interfered by Ag(I) for Hg^{2+} determination. As(III) has interference with the Cu stripping peak beyond 200 times higher concentration than Cu by broadening the Cu stripping peak.

The developed method was used to determine mercury in water and soil samples using the Bi-AuNPs nanocomposite modified carbon paste electrode. The results obtained from the present method was validated with the total mercury analyzer based on thermal decomposition and atomic absorption technique. Analysis results were agreed well between the two methods of determination. We have tested the stability of the sensor; it remains stable up to 7 days when stored inside water. Analytical performance of the presently developed electrode was compared with the methods reported previously in the literature for Cu and Hg, present method stands well in terms of sensitivity and easy of application compared to the reported literature.

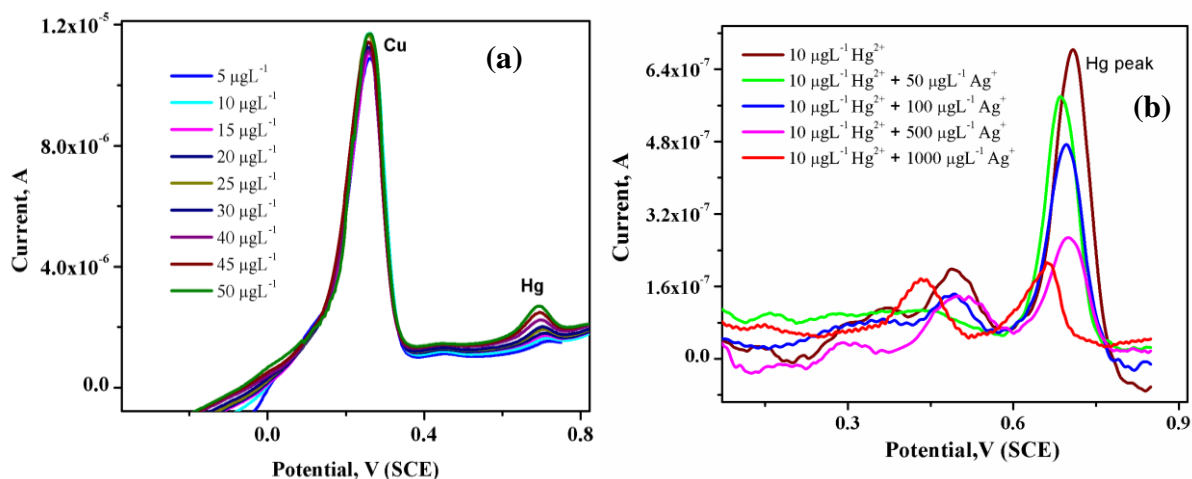


Figure.7. (a) Voltammetric plots of Hg^{2+} with its successive addition as shown inside the figure and at a constant concentration of Cu^{2+} of $200 \mu\text{g L}^{-1}$. (b) Interference effect of Ag(I) on the Hg stripping peak.

6. Applications in bioanalytical method developments

Analytical methods are developed for the determination of several biomolecules and drugs like, para-nitrophenol, dopamine, ascorbic acid, uric acid, cysteine, ciprofloxacin, darunavir, 6-mercaptopurine, and investigated their interactions with dsDNA, and serum albumin. Results on a few of these biomolecules are shown as below.[21, 29, 80-82].

6.1 Functionalized carbon nano particle modified electrode for the determination of Curcumin

A. Morphological and structural characteristics

The surface morphology of the FCNTs was investigated by scanning electron microscope (SEM) as shown in Figure 8. FCNTs are shown to have similar size, shape and uniformly distributed on the substrate. It was observed from SEM images that average diameter of the carbon nanotube is in the range of 10 to 40 nmol/L. The inset shows the EDS image of the FCNTs. The EDS microanalysis confirms the presence of the individual components of the FCNTs such as carbon, sulphur and oxygen and nitrogen as impurity in the FCNTs moiety.

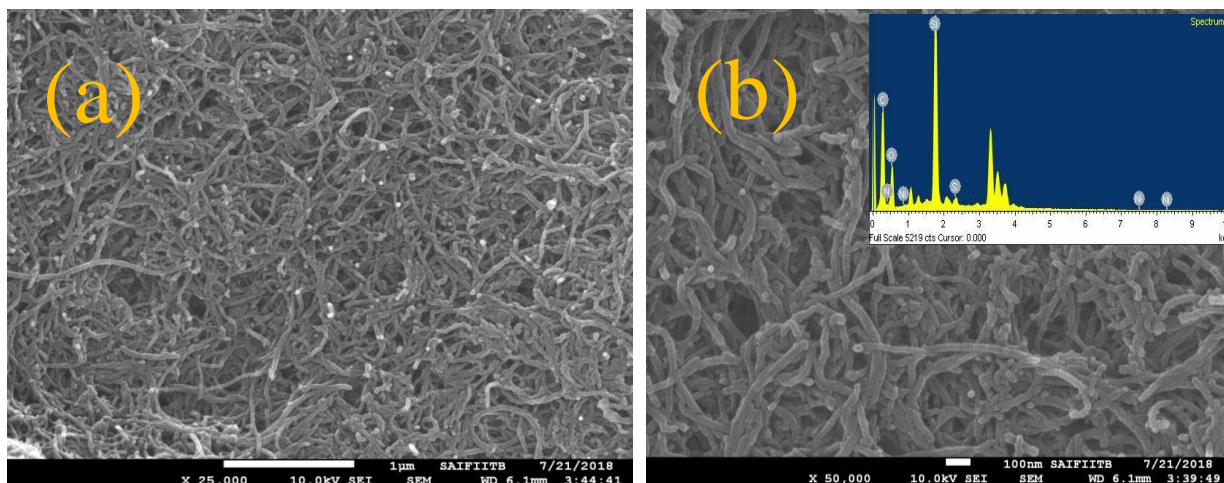


Figure 8 SEM images of FCNTs (a) Low resolution (b) High resolution (Inset: EDX images of FCNTS)[83].

B. Effect of pH on the electrochemical measurements

The effect of pH on oxidation of curcumin was investigated using square wave voltammetry in 0.1 mol/L acetate buffer solution containing 0.018 mmol/L curcumin and the results are shown in Figure 9a. The oxidation peak of curcumin was found to be shifted towards anodic direction with decrease in pH of the solution. The oxidation peak current was found to be increased with increase in the pH of the supporting electrolyte and reaches maximum at pH 4 and then reduces as the pH of the solution increases. The oxidation peak of curcumin was completely disappeared at pH above 12. The expulsion of a proton became easy with increase in alkalinity of the supporting electrolyte and the peak current has been increased [84]. The redox property of the curcumin at the surface of the modified electrode depends upon the transfer of proton along with the transfer of electrons during the oxidation and reduction process. The Nernstian slope of 0.059 V/pH indicates that the number of proton and electron proportion involved in the reaction is 1:1. Figure 9b shows the plot of pH vs peak potential of curcumin in the pH range of 1 to 12 and it was found to be linear with a correlation coefficient of 0.984, E_p (between pH 1 to 12) = 48.8 pH + 553. The slope of E_{p_a} vs pH was obtained as

0.049V/pH, which may be considered as closer to the Nernstian slope [85]. Therefore, the oxidation of curcumin is summarized as the involvements of $2e^-$ and $2H^+$ proton transfer process.

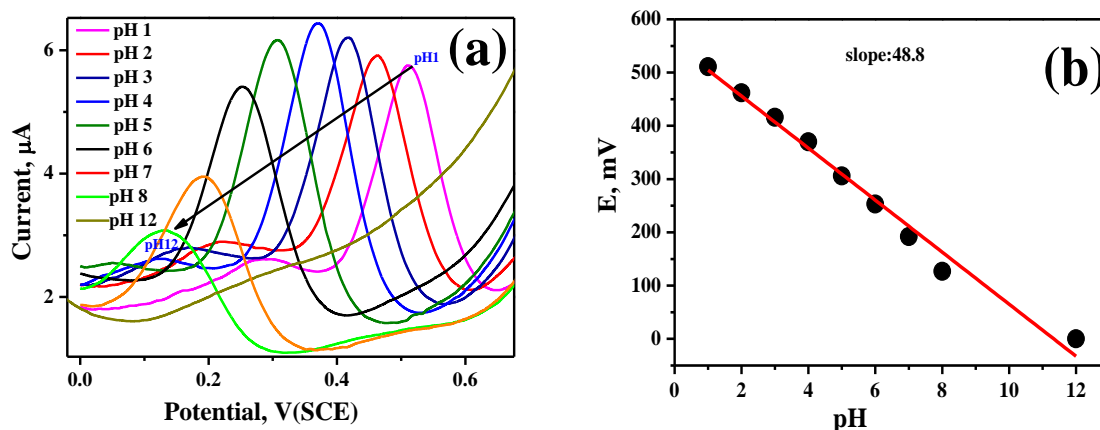


Figure 9 (a) Effects of variation of pH on 0.018 mmol/L curcumin using FCNTs modified electrode in 0.1 mol/L acetate buffer of pH 4.5 using square wave voltammetry. (b) Plot of peak potential vs pH.

C. Square wave voltammetric determination of curcumin

The anodic stripping voltammetry experiment was carried out with different concentrations from 2 to 14 $\mu\text{mol/L}$ using FCNTs modified electrode for the determination of the curcumin in 0.1 mol/L acetate buffer at pH 4.5 and the corresponding plot is shown in the Figure 10a. Good linear relationship between anodic peak current (I_{pc}) and the concentration of curcumin (Figure 10b) has been observed, the linear correlation followed the equation of I_{pc} (μA) = $1.2803c$ ($\mu\text{mol/L}$) + 3.0514 ($R^2 = 0.997$). The reproducibility of current was verified by carrying out the repetitive measurement for 5 times over the period of 25 days, the variation of the performance of the electrode remained within 5%. The limit of detection was calculated from the linear calibration plot and found to be $0.069 \mu\text{mol/L}$ using the IUPAC definition of $\text{LOD} = 3 S/M$, where S is the standard deviation and M is the plot of the calibration curve.

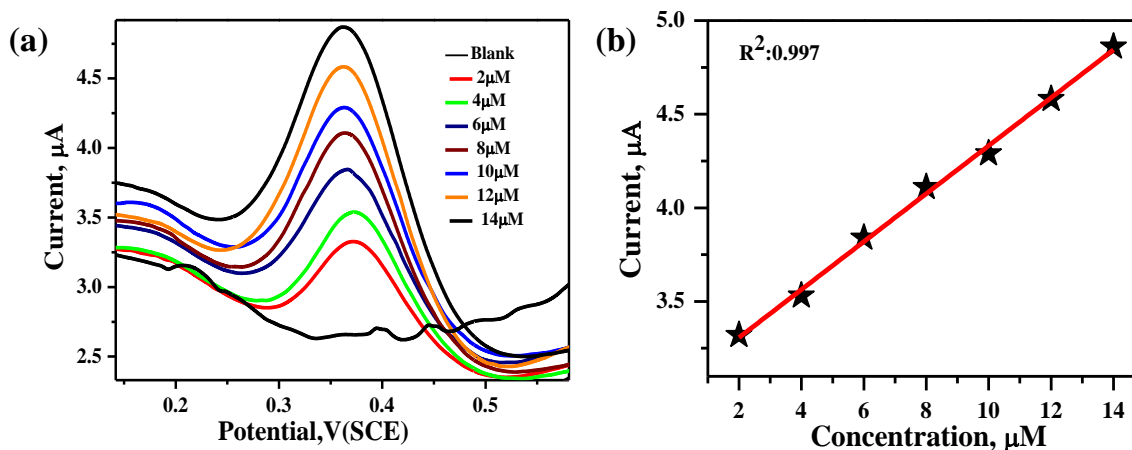
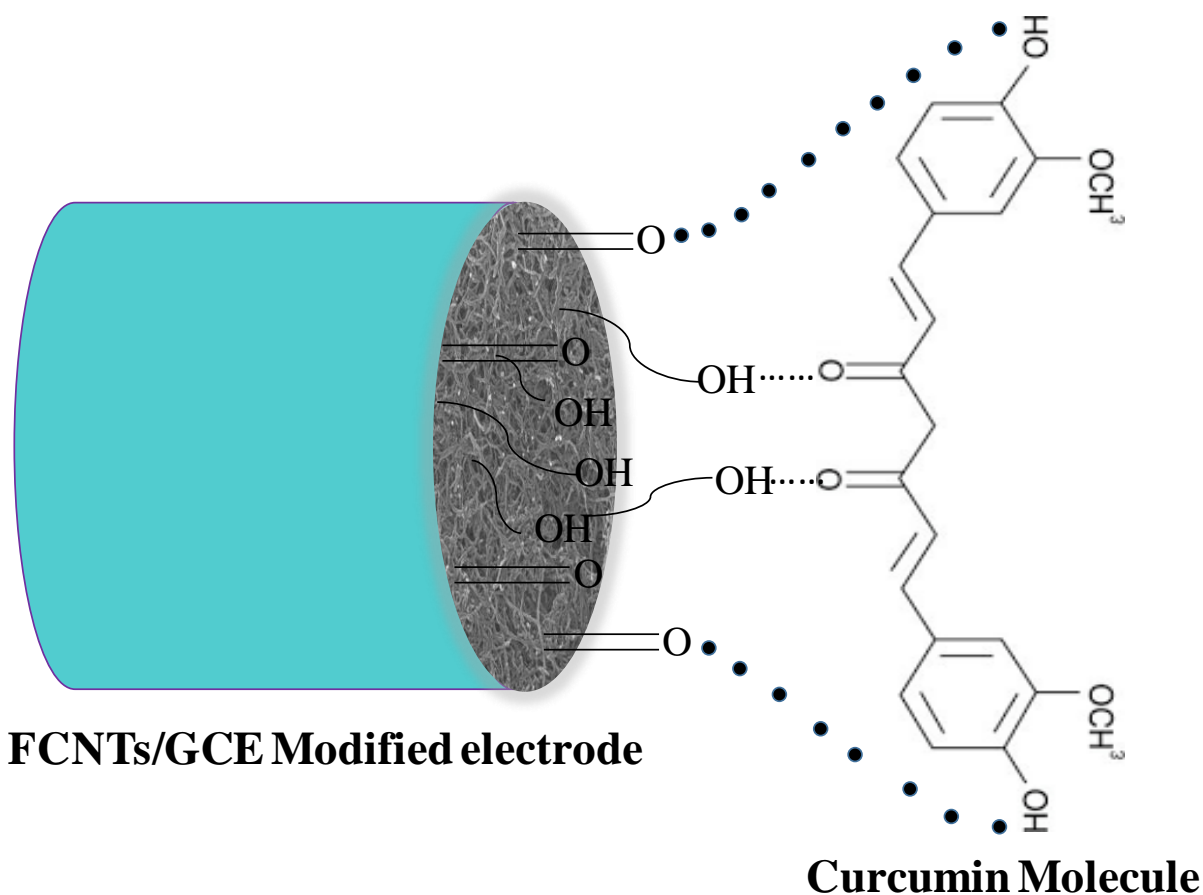


Figure 10 (a) Square wave voltammetry with varying concentrations of curcumin using the FCNTs/GCE modified electrode in 0.1 mol/L acetate buffer at pH 4. (b) Corresponding linear calibration plot.

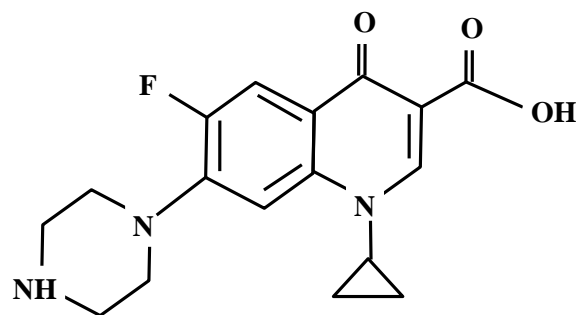
The higher electrochemical response over the GCE modified with FCNTs has been resulted due to the presence of the functional groups introduced over the CNTs and the inherent fast electron transfer properties of CNTs. The incorporation of the C=O and O-H groups as revealed from the FTIR measurements supports strong bonding with GCE base and also helps curcumin to come close to the modified electrode surface. The schematic representation of the interaction of the modified substrate with the curcumin molecule is represented in scheme 1. It may be noted the interactions are shown for the representative purposes with one molecule of curcumin, practically several molecules of curcumin will be interacted through different modes of interactions.



Scheme 1. Modes of interaction between the modified electrode substrate with the curcumin molecule.

6.2 Determination of Ciprofloxacin and Probing its Interaction with Bovine Serum Albumin

Ciprofloxacin (Cf) is an antibacterial drug that belongs to the fluoroquinolone family, and the IUPAC name of Cf is 1-cyclopropyl-6-fluoro-4-oxo-7-piperazin-1-yl-quinoline-3-carboxylic acid. Cf is a faintly yellowish to light-yellow crystalline substance with a molecular weight of 331.34 g/mol. The empirical formula of Cf is $C_{17}H_{18}FN_3O_3$ [1, 2]. The chemical structure of Cf is given in Scheme 2 [86, 87].



Scheme 2. Chemical structure of the antibiotic Cf

To investigate the drug interactions at the initial stage of the drug discovery, many *in vitro* methods are used. Of these methods, electrochemical, spectroscopic and spectro-electrochemical approaches are the most accurate, cost effective, easy to perform and time saving compared to *in vivo* studies, such as microbial experiments, animal studies and clinical trials. In the present investigation, in addition to the investigation of the electrochemical properties of Cf, we also probed the interaction of the Cf with serum albumin BSA using electrochemical, spectroscopic and spectro-electrochemical experiments.

A. Probing using CV

Cyclic voltammetry (CV) of 1.0×10^{-4} M Cf in a 0.04 M BR buffer with a pH of 7 was carried out at varying scan rates from 0.01 V/s to 0.5 V/s using GCE as the working electrode. After every CV scan, the GCE was cleaned by polishing it with 0.05 μm alumina powder on a polishing cloth to avoid adsorption of the drug to the surface of the electrode. The CV plots at different scan rates are overlaid and shown in Figure 10A. The plots had one oxidation peak of Cf at around 1.0 V, and the peak current rose along with an increase in the scan rate of the measurements. The peak current of Cf was plotted with respect to the scan rate of the measurements and also with regard to the square root of the scan rate of the measurements. The plots are shown in Figures 10B and C, respectively, and the data points were generated using

linear fitting. The peak current values fit reasonably well with the scan rate of the measurements and also with the square root of the scan rate of the measurements, although none of the correlations generated a perfect fitting of the results. The correlation of the peak current with the scan rate and the square root of the scan rate of the measurements thus indicated that the electrochemical process was influenced by both adsorption and diffusion. To further ascertain the overall mass transfer process, the peak current data were further analysed and the peak current per square root of scan rate was plotted with respect to the square root of the scan rate of the measurements; this plot is shown in Figure 10D. The data points are fitted well with the linear fit, which further supports the electrochemical oxidation process of Cf is characteristics of mixed adsorption and diffusion controlled process [88].

The electrochemical properties of Cf under different prototrophic conditions are traditionally investigated by recording the differential pulse voltammetry (DPV) [89]. Experiments were carried out at different pH values from 2–10, and their corresponding DPV plots are shown in Figure 10E. The peak potential shifted towards less positive potentials, which indicates that the oxidation of Cf becomes easy with an increase in the pH of the solution. The observed peak potentials have been plotted with respect to the pH of the solution, and the corresponding plot is shown in Figure 10F. The correlation between the potential and experimental pH fit well with the linear correlation, and the slope of linear fitting was 52 mV. The measured slope was close to the expected slope of 59 mV, and the mechanism of electrochemical oxidation process can be assigned to have an equal number of protons and electrons [90, 91].

The peak position of the voltammetric peak of Cf was shifted towards more positive potentials with each increase in the scan rate of the measurements. This shifting in the peak potential is indicative of the observed difficulty in the oxidation process of Cf at higher scan rates. The observed peak of Cf was plotted with the logarithm of the scan rate of the

measurements, and a straight-line correlation was generated (Figure 11B). The equation (1) used for the fitting is shown below [92].

$$E_p = E^0 + (RT/\alpha nF)[\ln(RTk_s/\alpha nF) - \ln v] \quad (1)$$

Where, E_p is the peak potential, E^0 is the formal potential, R is the universal gas constant (8.314 J/mol K), T is the absolute temperature, α is the electron transfer coefficient, n is the electron transfer number, F is Faraday's constant (96,485 C mol⁻¹), k_s is the standard rate constant of the reaction and v is the scan rate (V/s) of the measurements. The (αn) value is obtained using the linear fitting. E^0 of Cf is obtained from the intercept of the plot of the peak potential with respect to the scan rate of the measurements (Figure 11A). The value of E^0 obtained in this way was 0.99 V. Based upon the slope and intercept of the plot in Figure 11B, the (αn) and the k_s values were 0.85 and 275 s⁻¹, respectively. A similar method was used to determine the k_s values using electrochemical measurements [39]; the electrochemical kinetic parameters of Cf (αn) and the k_s were found to be 0.71 and 177.9 s⁻¹, respectively [93]. The electrochemical kinetics of Cf thus obtained over the GCE were reasonably fast, which can be utilised for the investigation of kinetics of the interaction of the Cf with carrier proteins as intended in the present study.

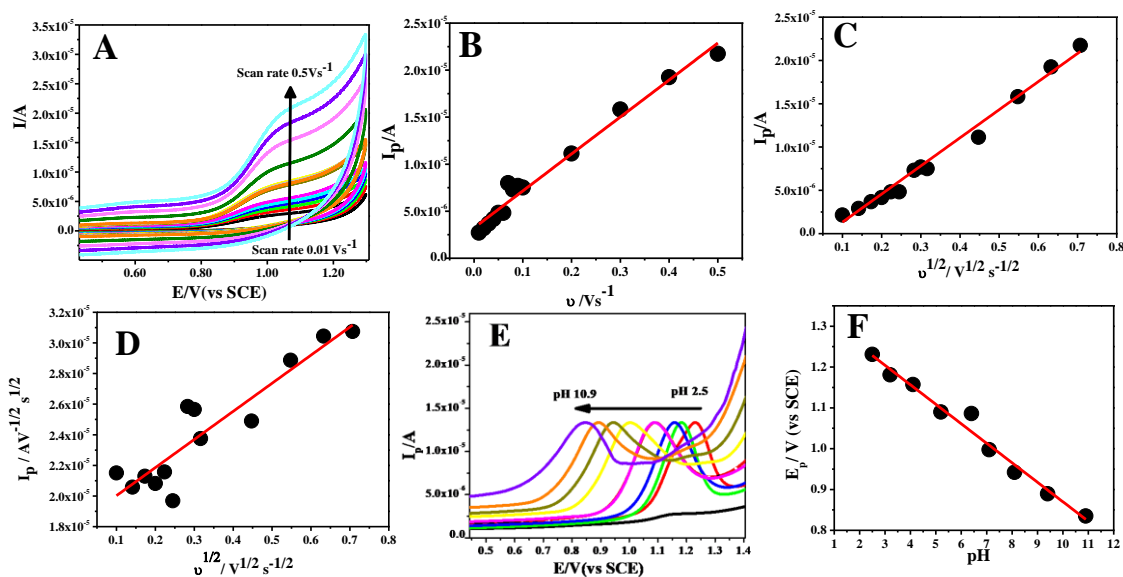


Figure 10. (A) CV of 1.0×10^{-4} M Cf at a pH of 7 with various scan rates, corresponding variation of peak current (I_p) with respect to (B) the scan rate and (C) the square root of the scan rate. (D) I_p per square root of the scan rate with respect to the square root of the scan rate. (E) DPV plots of 1.7×10^{-4} M Cf with varying pH values and their (F) corresponding variation of peak potentials (E_p) with respect to different pH values.

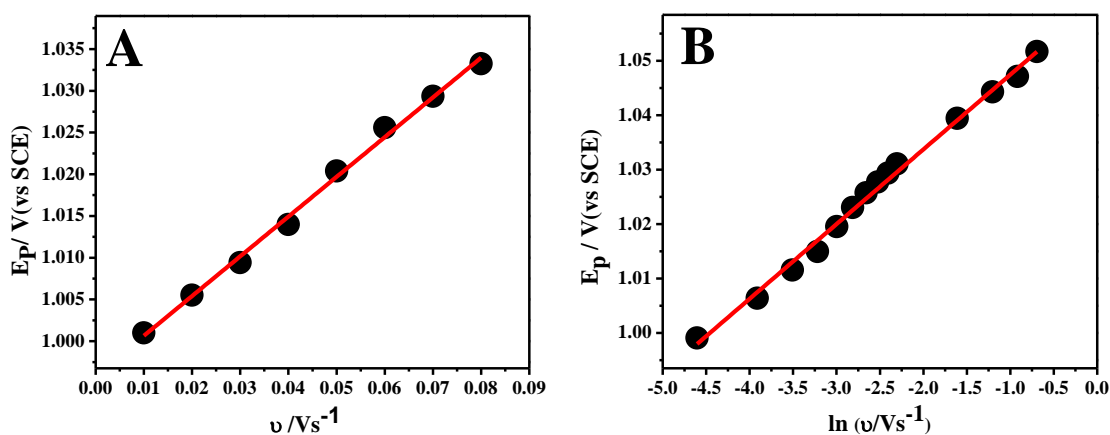


Fig. 11. (A) Plot of the peak potential vs the scan rate of the measurements; (B) Plot of the peak potential vs the log of the scan rate of the measurements [28].

6.3 Electrochemical Investigations on Melamine and Cysteine

Considering the toxic effects of melamine it is very important to determine melamine in milk products along with other food materials. There are some reports of determination of melamine based on chromatography [94-96] colorimetry [97, 98] and electrochemistry [99-101]. Determination of melamine using electrochemical techniques is becoming popular [102, 103]. With an aim to develop methods for the determination of melamine, electrochemical behavior of melamine have been explored in static mercury drop electrode (SMDE), AuNPs modified CPE and and RGO-AuNPs modified CPE. While, carrying out the CV with SMDE a peak due to reduction of melamine was observed at -0.93V at pH 2 of BR buffer solution, the peak position being shifted linearly (slope: -0.116 V/pH) in the cathodic direction with the pH of the buffer from pH 2 to pH 9, when pH was increased above 5 the electrochemical response merged with current produced due to the hydrogen evolution (Figure 12). The result reflected involvement of double number of proton to that of an electron in the reduction process, if the shift in peak potential is approximated only due to the proton concentration. Heterogeneous reduction was found to be diffusion controlled. The reduction peak intensity followed linear relationship with concentration of the compound (Figure 13), producing detection limit of 0.2 μ M in BR Buffer (pH 2). Although the method provides simplicity in determination of melamine at μ M concentration level, it suffered from the interference of commonly occurring Zn even in sub μ M concentration and Ca in the mM concentration level. Melamine has strong interaction with Cu²⁺, which generates electrochemical signals. These electrochemical signals could be a measure of melamine concentration [104]. However, a clear electrochemical signal for quantitative detection of melamine was not attempted previously. We have explored for the quantitative determination of melamine by monitoring the stripping signal of copper in linear sweep stripping voltammetry using SMDE. Anodic stripping voltammetry of copper was carried out with deposition of Cu²⁺ at a potential of -1.0 V for 10 s and then the potential was

scanned from -1.0 V to 0.2 V. The stripping peak due to the oxidation of Cu was observed at around 0 V as shown in figure 14. The original Cu stripping peak current was gradually decreased with the addition of melamine and a new pre-peak at more negative potential to that of the Cu stripping peak was appeared. Linear calibration plots were found from the decrease in the stripping peak of copper (peak 1) and increase in new peak, appeared at -0.09 V (peak 2). The three sigma LODs from the linear calibration plot was obtained as 0.778 μM (peak 1) and 0.773 μM (peak 2). For indirect determination of melamine this measurement was most workable procedure to determine melamine as it is very easy to obtain reproducible mercury drop for regular analysis. This indicated that the type of interaction responsible for the decrease in the stripping current of Cu and generation of a new pre-peak was the same. However, this method was affected by the interference due to the presence of Ag^+ , Pb^{2+} and Bi^{3+} at 10 times higher concentrations. The spike recovery test could not provide us with satisfactory result showing $\sim 35\%$ deviations from the added concentration of melamine. This might be due to the interaction of the organic molecules, present in the milk sample even after pretreatment, with Cu^{2+} ; possible interference due to deposition of other major metal ions such as Ca^{2+} and Zn^{2+} during preconcentration step on Hg surface cannot be withdrawn. Therefore, effort was extended to another indirect way to determine melamine by monitoring oxidation signal of $\text{K}_4[\text{Fe}(\text{CN})_6]$ on RGO-AuNPs Composite modified CPE (Figure 15). Square wave voltammetry was performed using 10^{-5} M ferrocyanide and the current due to the oxidation of ferrocyanide was used as the probe (Figure 16). The current was decreased by 40% due to the addition of 160 μM of melamine. The current was found to decrease proportionately (slope: 0.0025 AM^{-1}) with the addition of the melamine. The LOD was calculated to be 2.23 μM . The method was found to be free from Interferences from common metal ions including Hg^{2+} , Ag^+ , Cu^{2+} , Bi^{3+} , Pb^{2+} , K^+ , Na^+ , and Cl^- . Milk proteins interfere with the analysis, requiring additional sample preparation. The present modified electrode is easy to fabricate and operates

at higher concentration ranges compared to the literature reports. Thus, the RGO-AuNPs modified CPE was successfully used for the determination of melamine in milk sample. The work was further extended to measure the oxidation signal directly generated from the oxidation in the melamine centre. As the electrooxidation behavior of melamine is quite poor it is difficult to obtain the direct electrochemical oxidation peak due to melamine. In order to improve the electro-oxidation property of melamine, CPE was modified with MWCNT and nafion composite. Interestingly the electrochemical injection from the melamine molecules was improved on the MWCNT modified surface (Figure 17). This interaction of melamine with MWCNT was explored for the direct determination of melamine in contaminated samples. Use of nafion films has the advantage of suppression of interference besides holding the CNTs on the electrode surface. However, due to strong interaction of MWCNT with melamine, the electrode regeneration was an issue to use the sensor for actual application. To solve this problem another approach of modifying the electrode with AuNPs was proposed as AuNPs has strong interaction with melamine [105-108], although, the oxidation peak due to melamine was not experimentally observed on bulk gold electrode. Carbon paste electrode was modified with AuNPs by electrodeposition method. An oxidation signal at $\sim 0.15\text{V}$ was obtained when CV was carried out at a scan rate of 20mV sec^{-1} in PBS of pH 7. The redox process was found to be irreversible and adsorption controlled. The voltammetric signal was increased with the increase in concentration of melamine. Two calibration regions were observed one at low and the other at high concentrations (Figure 18). Present method was free from interferences from the metal ions like, Cu^{2+} , Ag^+ , Pb^{2+} , Bi^{3+} and Hg^{2+} at 100 fold higher concentration than melamine since the method does not include any preconcentration step.

Among the amino acids L-cysteine (CySH) is considered to be the most important one. This amino acid has important role in biological functioning and has been used widely in the medicine and food industries [109]. In addition to the basic electrochemical aspects it is

important to have analytical method for the sensitive determination of CySH [110, 111]. In this work a voltammetric method is developed for the determination of this molecule based on gold nano particles (AuNPs) modified glassy carbon electrode (GCE). A clear oxidation peak of CySH was observed at 0.69 V at pH 7.5. The oxidation peak potential of CySH was shifted towards more negative direction with increase in pH of the solution (Figure 19) which indicated important role of the proton concentration in the supporting electrolyte solution during the oxidation process of CySH. The oxidation process was proposed to be 2 electrons and 2 proton transfer process for the formation of CyS-SCy dimeric species. It was experimentally found that adsorption of monomeric and dimeric species plays a significant role in the heterogeneous redox process. Based on the electrochemical properties a voltammetric method was developed to quantify the species (Figure 20). LOD of 74nM was obtained. The chronoamperometric measurements revealed that the determination of CySH using the modified electrode is reasonably free from the interference due to tryptophan, tyrosine, histidine and methionine. The method has been applied for the real sample analysis.

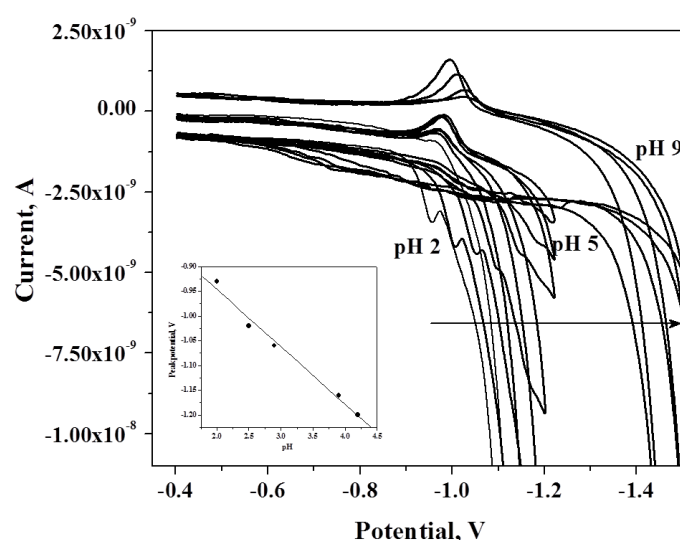


Figure 12: Cyclic voltammograms of melamine on SMDE in BR buffer of different pHs, Inset: plot of reduction peak potential of melamine with respect to pH of the solution.

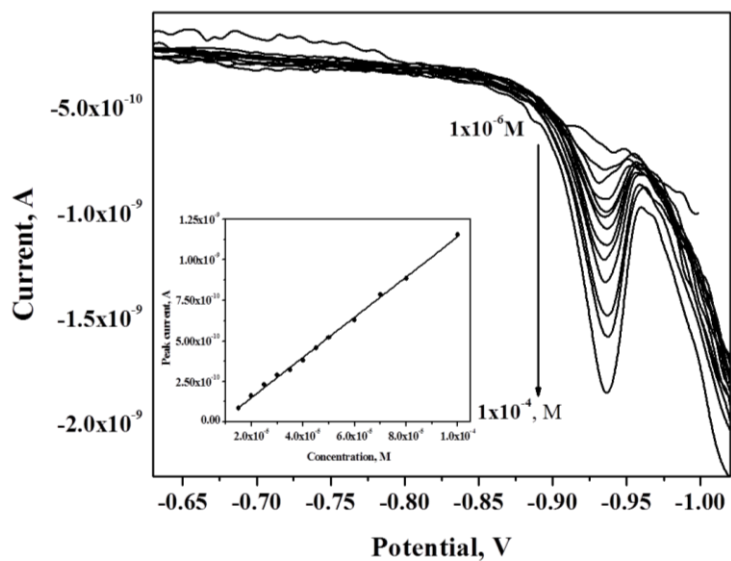


Figure 13: Differential pulse voltammograms of melamine reduction on SMDE with different concentration of melamine.

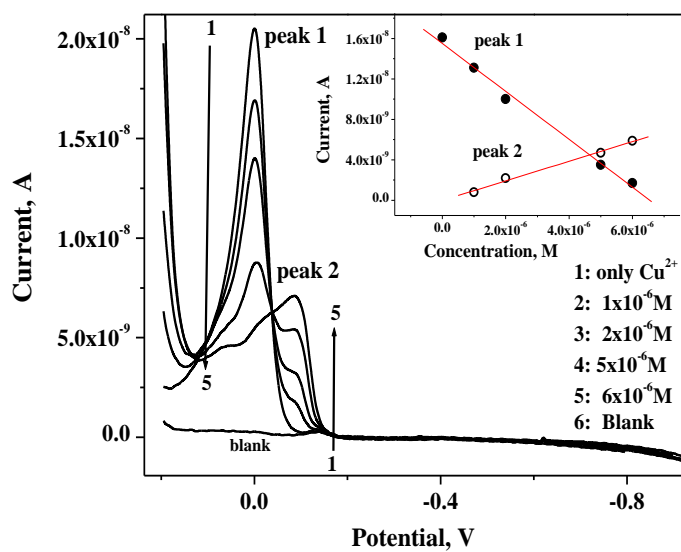


Figure 14: Linear sweep anodic stripping voltammetry of $3.3 \mu\text{M}$ of Cu^{2+} with different concentration of melamine. Deposition potential was -1.0 V for 10 sec . Inset: corresponding linear calibration plots of peak 1 and peak 2.

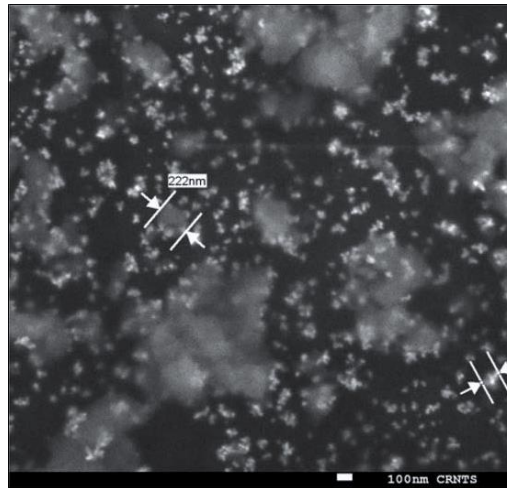


Figure 15: Scanning electron micrograph of the reduced graphene oxide–gold nanoparticles composite.

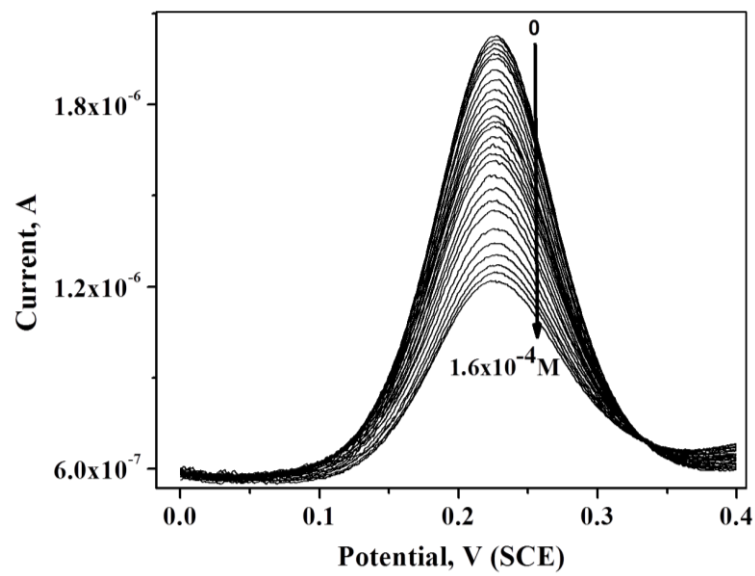


Figure 16: Square wave voltammograms of 0.01 mM $K_4[Fe(CN)_6]$ with the addition of melamine (top to bottom).

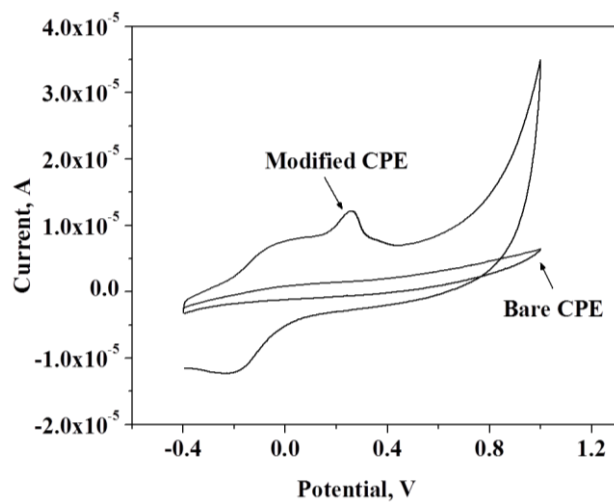


Figure 17: Cyclic voltammogram of oxidation of melamine on MWCNT-nafion composite modified CPE.

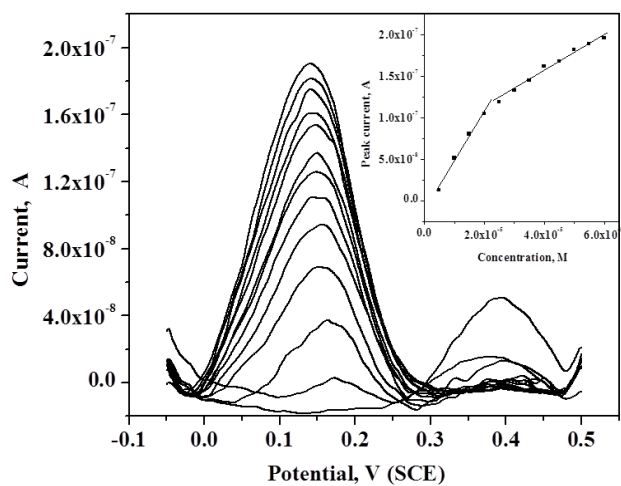


Figure 18: Square wave voltammograms of melamine on AuNPs modified carbon paste electrode with successive addition of 0.5 μM melamine. Inset: Corresponding calibration plot.

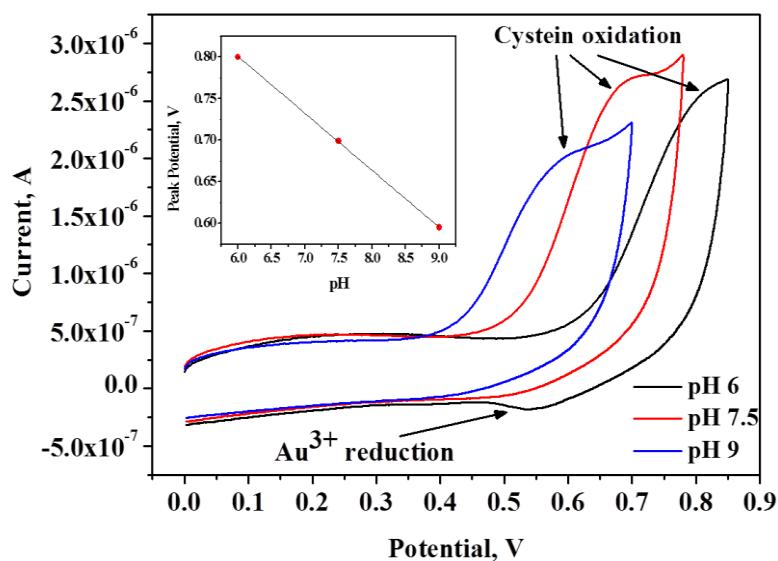


Figure 19: Cyclic voltammograms showing the effect of pH on CySH oxidation; Inset: Plot of oxidation peak potential against pH of the supporting electrolyte media.

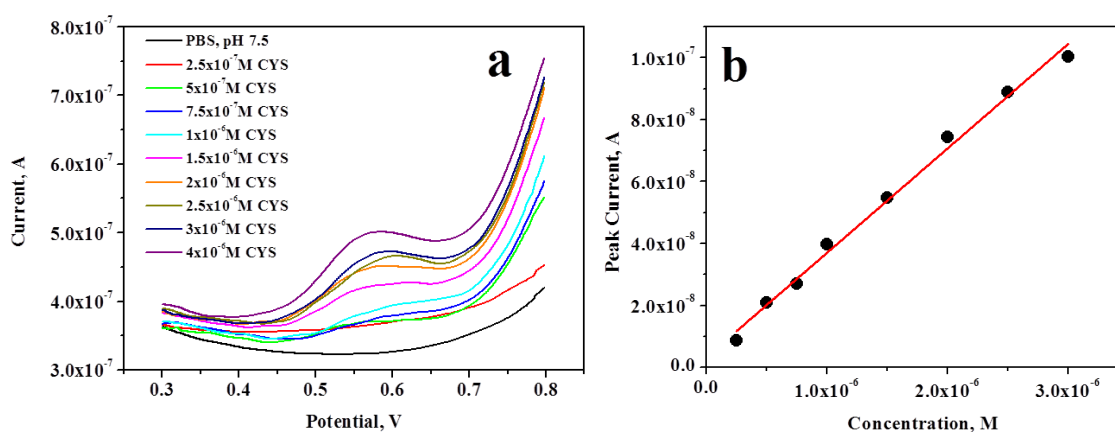


Figure 20: (a) Differential pulse anodic stripping voltammograms of different concentrations of the CySH in PBS of pH 7.5, using AuNPs modified GCE; (b) corresponding linear calibration plot of peak current and against concentration.

7. Interfacial research on energy harvesting and storage

Electrochemical science and technology have important thrust area in utilization of alternate energy through developing supercapacitor electrodes and efficient catalysts for electrochemical and photoelectrochemical generation hydrogen and oxygen from water. The

metal oxides and sulphides were synthesised, along with the graphene oxides (GO), reduced graphene oxides (rGO), 3D-graphene oxide and carbon quantum dots for making composites with the active redox components. The electron transport from the active redox system of the metal chalcogenides are enhanced and transported to the current collectors through the different forms of carbon synthesised for the application of the material as supercapacitor electrodes [112, 113].

Materials and composites of MoS₂, 3D graphene/noble metals, cobalt oxide, Ni oxide, bismuth vanadate, hematite etc. were synthesised through hydrothermal, electrochemical, metal organic frame work route for the electrochemical and photoelectrochemical splitting of water to generate hydrogen. The kinetics of the interfaces were probes through several conventional electrochemical technique and scanning electrochemical microscope [114-118].

The strategy of experimentation and some representative results are shown used in the characterization of the interfaces used in energy harvesting, storage and sensing substrates are shown in Figure 21.

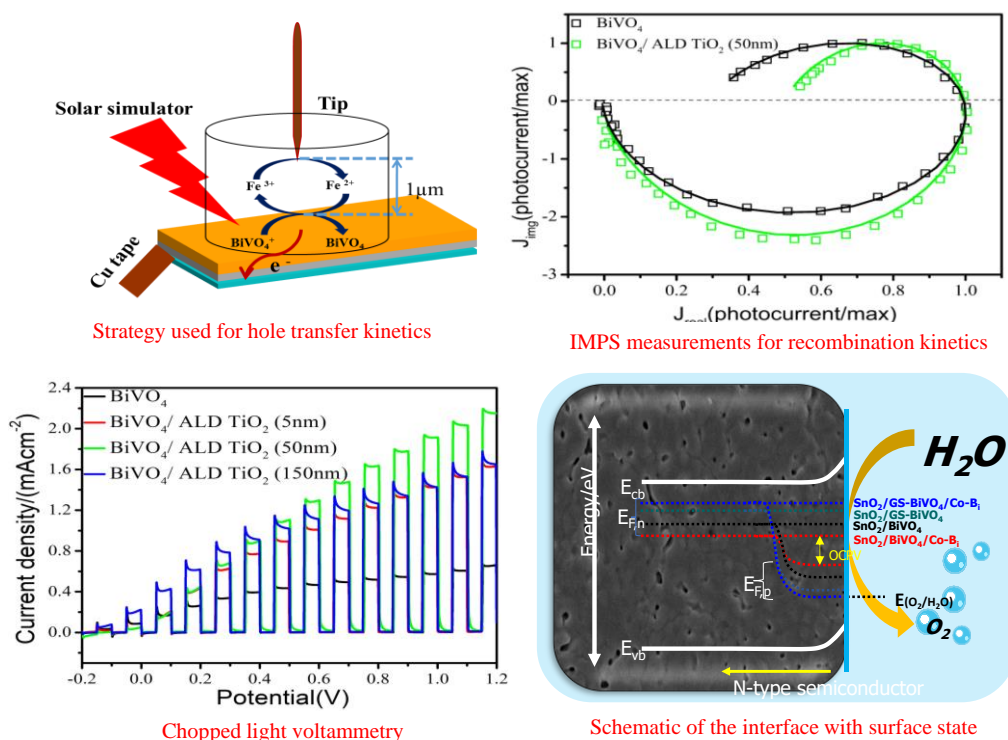


Figure 21. The Schematics of the experimental arrangements and information about the interfacial processes using hyphenated electrochemical measurements.

Bismuth vanadate (BiVO_4) has been one of the most promising photoanode for photoelectrochemical (PEC) water oxidation process. Efforts are still on to overcome the drawbacks of this photoanode to enhance the catalytic efficiency and improving the stability. In the present work, 3D graphene (3D-G) has been incorporated inside the BiVO_4 matrix, primarily to improve the conductivity of the material. The photoanodes are fabricated with the incorporation of SnO_2 heterojunction and application of cobalt borate (Co-B_i) as co-catalyst. The incorporation of 3D-G has enhanced the photocurrent from 0.72 mAcm^{-2} to 1.21 mAcm^{-2} in $\text{ITO/SnO}_2/\text{BiVO}_4$ and $\text{ITO/SnO}_2/3\text{D-G-BiVO}_4$ material, the photocurrent has been improved from 0.89 mAcm^{-2} to 1.52 mAcm^{-2} in $\text{ITO/SnO}_2/\text{BiVO}_4/\text{Co-B}_i$ and $\text{ITO/SnO}_2/3\text{D-G-BiVO}_4$. Semiconductor properties are evaluated from the Mott-Schottky measurements and the charge transfer and transport kinetics of the PEC process are measured from several photoelectrochemical investigations. Both the charge transport and the charge transfer efficiencies are enhanced upon inclusion of 3D-G into the catalytic system. The life time of the charge carrier is observed to be increased. The decrease in the decay kinetics of the holes, enhancement in the open circuit photovoltage (OCPV) and the resulted modulation of the surface states is responsible for the enhancement in the surface charge transfer process due to the inclusion of 3D-G into the catalytic system. Therefore, the additional role of 3D-G in the modulation of the surface states and release of the Fermi level pinning has made the band alignment between the semiconductor and the analyte better, which resulted in enhanced catalytic performance in the photoelectrochemical oxidation of water. Some of the related results are shown in Figure 22.

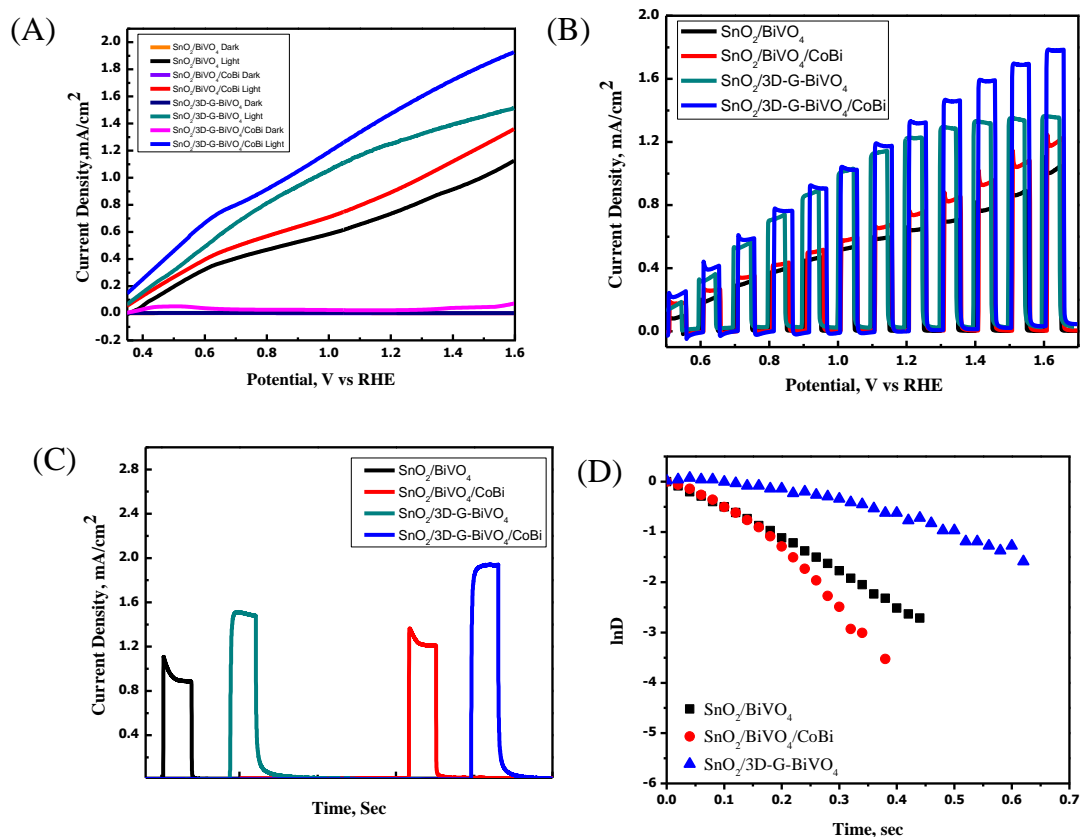


Figure 22. (A) Linear Sweep Voltammetry (BBS Buffer pH 8), (B) Chopped light Voltammetry for $\text{SnO}_2/\text{BiVO}_4$ (black), $\text{SnO}_2/\text{BiVO}_4/\text{Co-Bi}$ (red), $\text{SnO}_2/3\text{D-G-BiVO}_4$ (green), $\text{SnO}_2/3\text{D-G-BiVO}_4/\text{Co-Bi}$ (blue) (C) Transient Study for $\text{SnO}_2/\text{BiVO}_4$ (black), $\text{SnO}_2/\text{BiVO}_4/\text{Co-Bi}$ (red), $\text{SnO}_2/3\text{D-G-BiVO}_4$ (green), $\text{SnO}_2/3\text{D-G-BiVO}_4/\text{Co-Bi}$ (blue), (D) $\ln D$ vs Time graph for $\text{SnO}_2/\text{BiVO}_4$ (black), $\text{SnO}_2/\text{BiVO}_4/\text{Co-Bi}$ (red), $\text{SnO}_2/3\text{D-G-BiVO}_4$ (blue).

8. Research and developments on Electrochemical supercapacitor

Electrochemical supercapacitors have been attracted many researchers in the recent years because of their high-power density than batteries, long cyclic life and high energy density than conventional dielectric capacitors as the energy storage devices. In addition to that supercapacitor score high in terms of environmental friendliness among the energy storage devices. In recent years, various metal sulphides, oxides and their nano composites have been reported for their highly reversible electrochemical redox process, long cyclic stability, high

charge storage capacity through pseudo-capacitance and unique physical and chemical properties. Several metal oxides and sulphones are attempted in our laboratory for supercapacitor applications, out of which the results of a few of them are indicated in this subsection [112, 119-122].

The facile hydrothermal method is adopted for the synthesis of hierarchical flower like nickel sulphide nanostructure materials and its composite with carbon quantum dots (NiS/C-dots) composite. The composite material exhibited good performance for electrochemical energy storage devices as supercapacitor with specific capacity of 880 Fg^{-1} at the current density of 2 Ag^{-1} . The material remained stable up to the tested 2000 charge discharge cycles. Carbon quantum dots of 1.3 nm size were synthesised from natural sources and the favourable electronic and surface property of C-dots were utilised for improvement of the supercapacitor performance of NiS. The results from Tafel analysis, double layer capacitance and the impedance measurements reveals that the incorporation of C-dots inside the NiS matrix has improved the charge transfer process, which is mainly responsible for the enhancement of the super-capacitive property of the composite materials [114-116, 118, 123-126].

The discharge capacity of the materials was measured at different current density and the measured specific capacity was plotted with respect to the current density of the measurements (*cf.* Figure 23). The specific capacity of the composite material is higher compared to the pristine material, with increase in the current density, the specific capacity is increased initially then decreased very fast in the case of pristine material and slowly in the case of composite material. The specific capacity measured at multiple charge-discharge cycles and plotted up to 2000 cycles. Specific capacity is increased with multiple cycling up to the charge discharge cycle of around 50, after which the measured specific capacity is stabilised. It remained stable up to the charge-discharge cycles of 2000 recorded in the present measurements. Electrochemical impedance measurement provides the information about the

electrochemical interface by separating the transport of charge by overcoming the solution resistance, resistance in the double layer region, resistance due to the charge transfer and diffusion resistance. For a porous surface, additional pore resistance and pore capacitance also requires to be included for explaining the complete electrochemical behaviour. Supercapacitors have all such electrochemical processes require separate analysis to zero down the complete characterization of the electrochemical process involved during charging and discharging process. In the present case impedance measurements were carried out at different applied potentials of 0.16V, 0.46 V, 0.56V and 0.70V and the Nyquist plot are shown in Figure 23E for NiS/C-dots composite materials.

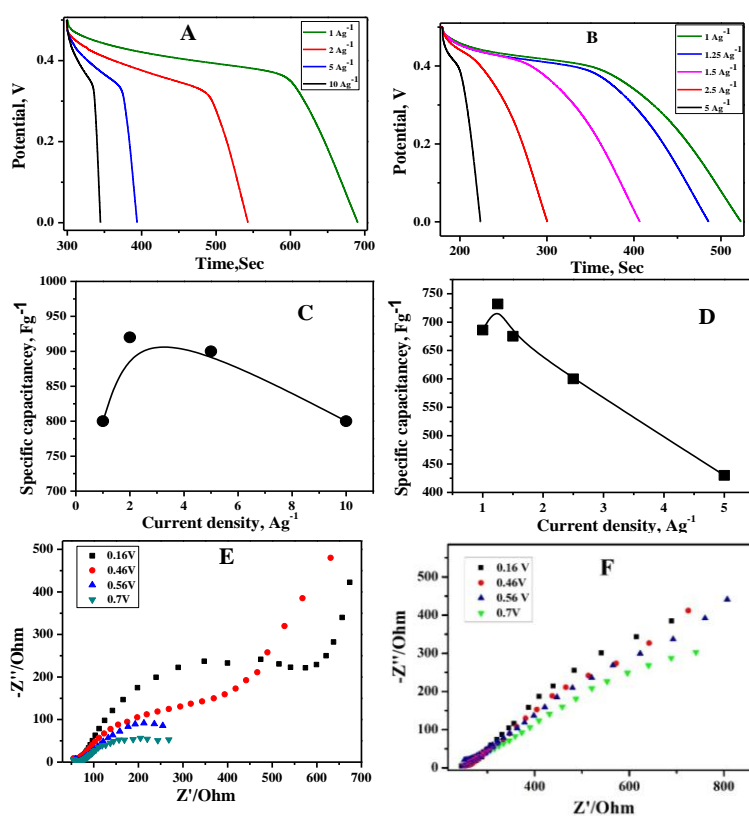


Figure 23. Galvanostatic charge discharge plot at different current density (A) NiS/C-dots composite (B) Pristine NiS and Specific capacity vs Current density (C) NiS/C-dots composite (D) Pristine NiS, (E) Nyquist plot of NiS/C-dots composite at different applied potentials (F) Nyquist plot of Pristine NiS at different applied potentials.

Currently the research is being carried out in the interfacial processes in materials, biological systems with focusing towards investigations in cellular level electrochemical investigations and detection of single molecular species through molecular collision. Solving several technological issues of the department utilising the electrochemical science and technology. Focus is also given in alternate energy harvesting and storage an important research aspect of the Department and of recent interest of the society.

9. Acknowledgements

We sincerely acknowledge the encouragements and supports from Dr. C N Patra, Head, Analytical Chemistry Division and Dr. Awadhesh Kumar, Associate Director, Chemistry Group.

References

- [1] A.K. Sundaram, S. Banerjee, Extraction of cations as salts of fatty acids: Beryllium as Butyrate, *Analytica Chimica Acta*, 8 (1953) 526-529.
- [2] V.T. Athavale, R.G. Dhaneswar, M.M. Mehta, Polarographic determination of nickel, chromium and tin in zircaloy and zirconium metal, *Analytica Chimica Acta*, 23 (1960) 74-77.
- [3] S.C. Saraiya, V.S. Srinivasan, A.K. Sundaram, Polarography of uranium in thiocyanate medium, *Analytica Chimica Acta*, 23 (1960) 77-82.
- [4] V. Athavale, S. Saraiya, A. Sundaram, Thorium-EDTA complexes-A conductometric study, *Analytica Chimica Acta*, 23 (1960) 200-201.
- [5] S. Saraiya, V. Srinivasan, A. Sundaram, Acetylacetone complexes of cadmium and lead: a polarographic study, *Current Science*, 31 (1962) 187-188.
- [6] T. Radhakrishnan, S. Saraiya, A. Sundaram, A conductometric-amperometric study of cadmium cobalticyanide, *Journal of Inorganic and Nuclear Chemistry*, 26 (1964) 378-382.

- [7] V. Apte, R. Dhaneshwar, Behaviour of the platinum electrode as a pH electrode, *Talanta*, 13 (1966) 1595-1598.
- [8] V. Athavale, M. Dhaneshwar, R. Dhaneshwar, Voltammetric studies with different electrode systems. Part IV. Determination of silver by using a silver-molybdenum system, *Analyst*, 94 (1969) 855-859.
- [9] V. Athavale, M. Dhaneshwar, R. Dhaneshwar, Bimetallic electrode systems in polarography: Cathode ray polarographic study using silver and silver amalgam cathodes and molybdenum anode, *Journal of Electroanalytical Chemistry and Interfacial Electrochemistry*, 14 (1967) 31-35.
- [10] R. Sundaresan, S. Saraiya, A. Sundaram, Polarography of zinc in alanine media, *Proceedings of the Indian Academy of Sciences-Section A*, Springer India, 1967, pp. 184-188.
- [11] R. Sundaresan, S. Saraiya, A. Sundaram, On the polarography of zinc in ethylenediamine medium, *Proceedings of the Indian Academy of Sciences-Section A*, Springer, 1967, pp. 120-124.
- [12] R. Sundaresan, S. Saraiya, T. Radhakrishnan, A. Sundaram, Polarography of zinc in presence of glycine, *Electrochimica Acta*, 13 (1968) 443-447.
- [13] M.M. Mehta, S.C. Saraiya, A.K. Sundaram, Effect of complexing agents on the disproportionation of uranium (V), *Proceedings of the Indian Academy of Sciences - Section A*, 63 (1966) 371-375.
- [14] R. Sundaresan, S. Saraiya, A. Sundaram, Indirect polarographic determination of stability constants: II. Pyridine complexes, *Proceedings of the Indian Academy of Sciences-Section A*, Springer, 1967, pp. 246-252.
- [15] S. Saraiya, A. Sundaram, Indirect polarographic determination of stability constants: IV. Thiosulphate complexes, *Proceedings of the Indian Academy of Sciences-Section A*, Springer, 1969, pp. 120-125.
- [16] T. Radhakrishnan, R. Sunderesan, S. Gangadharan, B. Sen, T. Murthy, Tritium generation during electrolysis experiment (Paper No. A6), 1989.

- [17] M. Palrecha, R. Parthasarathy, M.S. Das, A modified method for the determination of lead in zircons by differential-pulse anodic stripping voltammetry, *Analytica chimica acta*, 194 (1987) 299-302.
- [18] M. Palrecha, P. Mathur, Adsorptive stripping voltammetric determination of chromium in gallium, *Talanta*, 45 (1997) 433-436.
- [19] B. Chaudhari, T. Radhakrishnan, The uptake of cathodic hydrogen by shim steel, *Corrosion science*, 25 (1985) 1077-1088.
- [20] A. Tendulkar, T. Radhakrishnan, A galvanostatic study of the role of arsenic on the entry of hydrogen into mild steel, *Corrosion science*, 36 (1994) 1247-1256.
- [21] S. Sahoo, P. Sahoo, A. Sharma, A. Satpati, Interfacial polymerized RGO/MnFe₂O₄/polyaniline fibrous nanocomposite supported glassy carbon electrode for selective and ultrasensitive detection of nitrite, *Sensors and Actuators B: Chemical*, 309 (2020) 127763.
- [22] S. Sahoo, A. Satpati, A. Reddy, Electrodeposited Bi-Au nanocomposite modified carbon paste electrode for the simultaneous determination of copper and mercury, *RSC Advances*, 5 (2015) 25794-25800.
- [23] S. Sahoo, P.K. Sahoo, A.K. Satpati, Gold nano particle and reduced graphene oxide composite modified carbon paste electrode for the ultra trace detection of arsenic (III), *Electroanalysis*, 29 (2017) 1400-1409.
- [24] A.A. Dalvi, A. Satpati, M. Palrecha, Simultaneous determination of Pt and Rh by catalytic adsorptive stripping voltammetry, using hexamethylene tetramine (HMTA) as complexing agent, *Talanta*, 75 (2008) 1382-1387.
- [25] V. Aher, M. Palrecha, A. Kulkarni, G. Shah, Determination of palladium in synthetic nuclear wastes by differential pulse voltammetry, *Journal of radioanalytical and nuclear chemistry*, 252 (2002) 573-576.

- [26] S. Phadnis, A. Satpati, K. Muthe, J. Vyas, R. Sundaresan, Comparison of rolled and heat treated SS304 in chloride solution using electrochemical and XPS techniques, *Corrosion science*, 45 (2003) 2467-2483.
- [27] A. Satpati, S. Phadnis, R. Sundaresan, Electrochemical and XPS studies and the potential scan rate dependent pitting corrosion behavior of Zircaloy-2 in 5% NaCl solution, *Corrosion science*, 47 (2005) 1445-1458.
- [28] P.R. Ipte, A.K. Satpati, Probing the interaction of ciprofloxacin and E. coli by electrochemistry, spectroscopy and atomic force microscopy, *Biophysical chemistry*, 266 (2020) 106456.
- [29] P. Ipte, A. Sharma, H. Pal, A. Satpati, Probing the interaction of ciprofloxacin with dsDNA: electrochemical, spectro-electrochemical and AFM investigation, *Journal of Electroanalytical Chemistry*, 885 (2021) 115098.
- [30] M. Gholivand, H.R. Nassab, H. Fazeli, Cathodic adsorptive stripping voltammetric determination of uranium (VI) complexed with 2, 6-pyridinedicarboxylic acid, *Talanta*, 65 (2005) 62-66.
- [31] T.P. Rao, P. Metilda, J.M. Gladis, Preconcentration techniques for uranium (VI) and thorium (IV) prior to analytical determination—an overview, *Talanta*, 68 (2006) 1047-1064.
- [32] E. Andreotti, A. Credaro, C. Dossi, A. Giuliani, D. Monticelli, M. Pellicciari, S. Sangiorgio, Determination of uranium content in water using cathodic stripping voltammetry and gamma-spectrometry, *Journal of Radioanalytical and Nuclear Chemistry*, 277 (2008) 413-417.
- [33] A. D'Ulivo, V. Loreti, M. Onor, E. Pitzalis, R. Zamboni, Chemical vapor generation atomic spectrometry using amineboranes and cyanotrihydroborate (III) reagents, *Analytical chemistry*, 75 (2003) 2591-2600.
- [34] X.-P. Yan, X.-B. Yin, D.-Q. Jiang, X.-W. He, Speciation of mercury by hydrostatically modified electroosmotic flow capillary electrophoresis coupled with volatile species generation atomic fluorescence spectrometry, *Analytical Chemistry*, 75 (2003) 1726-1732.

- [35] S.J. Christopher, S.E. Long, M. Rearick, J.D. Fassett, Development of isotope dilution cold vapor inductively coupled plasma mass spectrometry and its application to the certification of mercury in NIST standard reference materials, *Analytical Chemistry*, 73 (2001) 2190-2199.
- [36] Y.A. Vil'pan, I.L. Grinshtein, A.A. Akatov, S. Gucer, Direct atomic absorption determination of mercury in drinking water and urine using a two-step electrothermal atomizer, *Journal of Analytical Chemistry*, 60 (2005) 38-44.
- [37] E. KopyŚĆ, K. PyrzyŃska, S. GarboŚ, E. Buska, Determination of mercury by cold-vapor atomic absorption spectrometry with preconcentration on a gold-trap, *Analytical sciences*, 16 (2000) 1309-1312.
- [38] H. Xu, L. Zeng, S. Xing, G. Shi, J. Chen, Y. Xian, L. Jin, Highly ordered platinum-nanotube arrays for oxidative determination of trace arsenic (III), *Electrochemistry Communications*, 10 (2008) 1893-1896.
- [39] S.R. Segade, J.F. Tyson, Determination of methylmercury and inorganic mercury in water samples by slurry sampling cold vapor atomic absorption spectrometry in a flow injection system after preconcentration on silica C18 modified, *Talanta*, 71 (2007) 1696-1702.
- [40] F. Ubillús, A. Alegría, R. Barberá, R. Farré, M.J. Lagarda, Methylmercury and inorganic mercury determination in fish by cold vapour generation atomic absorption spectrometry, *Food Chemistry*, 71 (2000) 529-533.
- [41] O. Abollino, A. Giacomino, M. Malandrino, G. Piscionieri, E. Mentasti, Determination of mercury by anodic stripping voltammetry with a gold nanoparticle-modified glassy carbon electrode, *Electroanalysis: An International Journal Devoted to Fundamental and Practical Aspects of Electroanalysis*, 20 (2008) 75-83.
- [42] B. Kumar Jena, C. Retna Raj, Gold nanoelectrode ensembles for the simultaneous electrochemical detection of ultratrace arsenic, mercury, and copper, *Analytical chemistry*, 80 (2008) 4836-4844.
- [43] H. Xu, L.P. ZENG, S.J. XING, Y.Z. XIAN, G.Y. SHI, L.T. JIN, Electropolymerization and Electrochromic Properties of Poly (3-bromothiophene) Films on a Transparent Nano-mesoporous TiO₂ Surface, *Chinese Journal of Chemistry*, 26 (2008) 1991-1996.

- [44] T. Hezard, K. Fajerweg, D. Evrard, V. Collière, P. Behra, P. Gros, Gold nanoparticles electrodeposited on glassy carbon using cyclic voltammetry: Application to Hg (II) trace analysis, *Journal of Electroanalytical Chemistry*, 664 (2012) 46-52.
- [45] O. Abollino, A. Giacomino, M. Malandrino, S. Marro, E. Mentasti, Voltammetric determination of methylmercury and inorganic mercury with an home made gold nanoparticle electrode, *Journal of applied electrochemistry*, 39 (2009) 2209-2216.
- [46] E. Bernalte, C.M. Sánchez, E.P. Gil, Gold nanoparticles-modified screen-printed carbon electrodes for anodic stripping voltammetric determination of mercury in ambient water samples, *Sensors and Actuators B: Chemical*, 161 (2012) 669-674.
- [47] E. Bernalte, C.M. Sánchez, E.P. Gil, Determination of Mercury in indoor dust samples by ultrasonic probe microextraction and stripping voltammetry on gold nanoparticles-modified screen-printed electrodes, *Talanta*, 97 (2012) 187-192.
- [48] J. Gong, T. Zhou, D. Song, L. Zhang, X. Hu, Stripping voltammetric detection of mercury (II) based on a bimetallic Au- Pt inorganic- organic hybrid nanocomposite modified glassy carbon electrode, *Analytical chemistry*, 82 (2010) 567-573.
- [49] A. Mandil, L. Idrissi, A. Amine, Stripping voltammetric determination of mercury (II) and lead (II) using screen-printed electrodes modified with gold films, and metal ion preconcentration with thiol-modified magnetic particles, *Microchimica Acta*, 170 (2010) 299-305.
- [50] X. Niu, C. Chen, Y. Teng, H. Zhao, M. Lan, Novel Screen-Printed Gold Nano Film Electrode for Trace Mercury(II) Determination Using Anodic Stripping Voltammetry, *Analytical Letters*, 45 (2012) 764-773.
- [51] J. Wang, J. Lu, S.B. Hocevar, P.A. Farias, B. Ogorevc, Bismuth-coated carbon electrodes for anodic stripping voltammetry, *Analytical chemistry*, 72 (2000) 3218-3222.
- [52] J. Wang, J. Lu, Ü.A. Kirgöz, S.B. Hocevar, B. Ogorevc, Insights into the anodic stripping voltammetric behavior of bismuth film electrodes, *Analytica Chimica Acta*, 434 (2001) 29-34.
- [53] J. Wang, Stripping analysis at bismuth electrodes: a review, *Electroanalysis: An International Journal Devoted to Fundamental and Practical Aspects of Electroanalysis*, 17 (2005) 1341-1346.

- [54] J. Wang, R.P. Deo, S. Thongngamdee, B. Ogorevc, Effect of surface-active compounds on the stripping voltammetric response of bismuth film electrodes, *Electroanalysis: An International Journal Devoted to Fundamental and Practical Aspects of Electroanalysis*, 13 (2001) 1153-1156.
- [55] A. Economou, Bismuth-film electrodes: recent developments and potentialities for electroanalysis, *TrAC Trends in Analytical Chemistry*, 24 (2005) 334-340.
- [56] A. Królicka, A. Bobrowski, Bismuth film electrode for adsorptive stripping voltammetry–electrochemical and microscopic study, *Electrochemistry Communications*, 6 (2004) 99-104.
- [57] I. Švancara, K. Vytřas, Electroanalysis with bismuth electrodes: State of the art and future prospects, *Chemické listy*, 100 (2006).
- [58] A. Królicka, R. Pauliukait, I. Švancara, R. Metelka, A. Bobrowski, E. Norkus, K. Kalcher, K. Vytřas, Bismuth-film-plated carbon paste electrodes, *Electrochemistry Communications*, 4 (2002) 193-196.
- [59] G.-U. Flechsig, M. Kienbaum, P. Gründler, Ex situ atomic force microscopy of bismuth film deposition at carbon paste electrodes, *Electrochemistry communications*, 7 (2005) 1091-1097.
- [60] K. Vytřas, I. Švancara, R. Metelka, A novelty in potentiometric stripping analysis: Total replacement of mercury by bismuth, *Electroanalysis: An International Journal Devoted to Fundamental and Practical Aspects of Electroanalysis*, 14 (2002) 1359-1364.
- [61] J.R. Miller, J. Rowland, P.J. Lechler, M. Desilets, L.-C. Hsu, Dispersal of mercury-contaminated sediments by geomorphic processes, Sixmile Canyon, Nevada, USA: implications to site characterization and remediation of fluvial environments, *Water, Air, and Soil Pollution*, 86 (1996) 373-388.
- [62] R.E. Clement, C.J. Koester, G.A. Eiceman, Environmental analysis, *Analytical chemistry*, 65 (1993) 85-116.
- [63] G.J. Brewer, Copper toxicity in the general population, *Clinical Neurophysiology*, 4 (2010) 459-460.

- [64] G.-J. Lee, C.K. Kim, M.K. Lee, C.K. Rhee, Reliability evaluation of nano-Bi/silver paste sensor electrode for detecting trace metals, *Journal of Nanoscience and Nanotechnology*, 12 (2012) 5673-5677.
- [65] J. Wang, Ü.A. Kirgöz, J. Lu, Stripping voltammetry with the electrode material acting as a built-in internal standard, *Electrochemistry communications*, 3 (2001) 703-706.
- [66] S.B. Hocevar, J. Wang, R.P. Deo, B. Ogorevc, Potentiometric stripping analysis at bismuth-film electrode, *Electroanalysis: An International Journal Devoted to Fundamental and Practical Aspects of Electroanalysis*, 14 (2002) 112-115.
- [67] M. Dey, A. Satpati, S. Sahoo, R. Kameswaran, A. Reddy, T. Mukherjee, Bi-Film on a carbon paste electrode modified with nafion film embedded with multiwall carbon nano tubes for the determination of heavy metals, *Analytical Methods*, 3 (2011) 2540-2546.
- [68] P. Sahoo, B. Panigrahy, S. Sahoo, A.K. Satpati, D. Li, D. Bahadur, In situ synthesis and properties of reduced graphene oxide/Bi nanocomposites: as an electroactive material for analysis of heavy metals, *Biosensors and Bioelectronics*, 43 (2013) 293-296.
- [69] X. Dai, G.G. Wildgoose, C. Salter, A. Crossley, R.G. Compton, Electroanalysis using macro-, micro-, and nanochemical architectures on electrode surfaces. Bulk surface modification of glassy carbon microspheres with gold nanoparticles and their electrical wiring using carbon nanotubes, *Analytical chemistry*, 78 (2006) 6102-6108.
- [70] T.J. Davies, R.G. Compton, The cyclic and linear sweep voltammetry of regular and random arrays of microdisc electrodes: Theory, *Journal of Electroanalytical Chemistry*, 585 (2005) 63-82.
- [71] T.J. Davies, C.E. Banks, R.G. Compton, Voltammetry at spatially heterogeneous electrodes, *Journal of Solid State Electrochemistry*, 9 (2005) 797-808.
- [72] G.O. Buica, C. Bucher, J.C. Moutet, G. Royal, E. Saint-Aman, E.M. Ungureanu, Voltammetric Sensing of Mercury and Copper Cations at Poly (EDTA-like) Film Modified Electrode, *Electroanalysis: An International Journal Devoted to Fundamental and Practical Aspects of Electroanalysis*, 21 (2009) 77-86.

- [73] Y. Li, G. Sun, Y. Zhang, C. Ge, N. Bao, Y. Wang, A glassy carbon electrode modified with bismuth nanotubes in a silsesquioxane framework for sensing of trace lead and cadmium by stripping voltammetry, *Microchimica Acta*, 181 (2014) 751-757.
- [74] C. Lee, S. Jeong, N. Myung, K. Rajeshwar, Preparation of Au-Bi₂O₃ nanocomposite by anodic electrodeposition combined with galvanic replacement, *Journal of The Electrochemical Society*, 161 (2014) D499.
- [75] Y. Bonfil, M. Brand, E. Kirowa-Eisner, Trace determination of mercury by anodic stripping voltammetry at the rotating gold electrode, *Analytica chimica acta*, 424 (2000) 65-76.
- [76] A. Giacomino, O. Abollino, M. Malandrino, E. Mentasti, Parameters affecting the determination of mercury by anodic stripping voltammetry using a gold electrode, *Talanta*, 75 (2008) 266-273.
- [77] M. Ghaedi, M. Reza Fathi, A. Shokrollahi, F. Shajarat, Highly selective and sensitive preconcentration of mercury ion and determination by cold vapor atomic absorption spectroscopy, *Analytical Letters*, 39 (2006) 1171-1185.
- [78] F. Marahel, M. Ghaedi, A. Shokrollahi, M. Montazerzohori, S. Davoodi, Sodium dodecyl sulfate coated poly (vinyl) chloride: An alternative support for solid phase extraction of some transition and heavy metals, *Chemosphere*, 74 (2009) 583-589.
- [79] H. Khani, M.K. Rofouei, P. Arab, V.K. Gupta, Z. Vafaei, Multi-walled carbon nanotubes-ionic liquid-carbon paste electrode as a super selectivity sensor: application to potentiometric monitoring of mercury ion (II), *Journal of hazardous materials*, 183 (2010) 402-409.
- [80] S. Sahoo, A. Satpati, Fabrication of rGO/NiS/AuNCs ternary nanocomposite modified electrode for electrochemical sensing of Cr (VI) at ultra-trace level, *Surfaces and Interfaces*, 24 (2021) 101096.
- [81] S. Sahoo, P. Sahoo, S. Manna, A. Satpati, A novel low cost nonenzymatic hydrogen peroxide sensor based on CoFe₂O₄/CNTs nanocomposite modified electrode, *Journal of Electroanalytical Chemistry*, 876 (2020) 114504.
- [82] P.R. Ipte, S. Sahoo, A. Satpati, Spectro-electrochemistry of ciprofloxacin and probing its interaction with bovine serum albumin, *Bioelectrochemistry*, 130 (2019) 107330.

- [83] S. Sahoo, A. Satpati, Determination of Curcumin on Functionalized Carbon Nano Tube Modified Electrode and Probing its Interaction with DNA and Copper Ion, *Journal of Analysis and Testing*, 7 (2023) 136-146.
- [84] A. Satpati, S. Sahoo, M. Dey, A. Reddy, T. Mukherjee, Electrochemical and spectroelectrochemical investigations of quercetin on unmodified and DNA-modified carbon paste electrode and its determination using voltammetry, *Analytical Methods*, 3 (2011) 1344-1350.
- [85] P. Daneshgar, P. Norouzi, A.A. Moosavi-Movahedi, M.R. Ganjali, E. Haghshenas, F. Dousty, M. Farhadi, Fabrication of carbon nanotube and dysprosium nanowire modified electrodes as a sensor for determination of curcumin, *Journal of applied electrochemistry*, 39 (2009) 1983-1992.
- [86] K.F. Ali, Estimation and evaluation of the effect of pH on ciprofloxacin in drug formulations, *J. Chem. Pharm. Res*, 6 (2014) 910-916.
- [87] N. Rajendiran, M. Suresh, Study of the interaction of ciprofloxacin and sparfloxacin with biomolecules by spectral, electrochemical and molecular docking methods, *International Letters Chem., Phys. Astronomy*, 78 (2018) 1-29.
- [88] L.M. Goncalves, C. Batchelor-McAuley, A.A. Barros, R.G. Compton, Electrochemical oxidation of adenine: a mixed adsorption and diffusion response on an edge-plane pyrolytic graphite electrode, *The Journal of Physical Chemistry C*, 114 (2010) 14213-14219.
- [89] F. Scholz, *Electroanalytical methods*, Springer 2010.
- [90] X. Zhang, Y. Wei, Y. Ding, Electrocatalytic oxidation and voltammetric determination of ciprofloxacin employing poly (alizarin red)/graphene composite film in the presence of ascorbic acid, uric acid and dopamine, *Analytica chimica acta*, 835 (2014) 29-36.
- [91] F. Zhang, S. Gu, Y. Ding, Z. Zhang, L. Li, A novel sensor based on electropolymerization of β -cyclodextrin and l-arginine on carbon paste electrode for determination of fluoroquinolones, *Analytica chimica acta*, 770 (2013) 53-61.

- [92] E. Laviron, General expression of the linear potential sweep voltammogram in the case of diffusionless electrochemical systems, *Journal of Electroanalytical Chemistry and Interfacial Electrochemistry*, 101 (1979) 19-28.
- [93] L. Fotouhi, M. Alahyari, Electrochemical behavior and analytical application of ciprofloxacin using a multi-walled nanotube composite film-glassy carbon electrode, *Colloids and Surfaces B: Biointerfaces*, 81 (2010) 110-114.
- [94] M.S. Filigenzi, B. Puschner, L.S. Aston, R.H. Poppenga, Diagnostic determination of melamine and related compounds in kidney tissue by liquid chromatography/tandem mass spectrometry, *Journal of Agricultural and Food Chemistry*, 56 (2008) 7593-7599.
- [95] H. Wang, Y. Liu, H. Cao, H. Yang, X. Liu, L. Yan, Determination of melamine in pet food by SPE-HPLC, *Chinese Journal of Analytical Chemistry*, 36 (2008) 273-274.
- [96] W.C. Andersen, S.B. Turnipseed, C.M. Karbiwnyk, S.B. Clark, M.R. Madson, C.M. Giesecker, R.A. Miller, N.G. Rummel, R. Reimschuessel, Determination and confirmation of melamine residues in catfish, trout, tilapia, salmon, and shrimp by liquid chromatography with tandem mass spectrometry, *Journal of Agricultural and Food Chemistry*, 56 (2008) 4340-4347.
- [97] F. Wei, R. Lam, S. Cheng, S. Lu, D. Ho, N. Li, Rapid detection of melamine in whole milk mediated by unmodified gold nanoparticles, *Applied Physics Letters*, 96 (2010).
- [98] R.K. Bera, C.R. Raj, Naked eye sensing of melamine using rationally tailored gold nanoparticles: hydrogen-bonding and charge-transfer recognition, *Analyst*, 136 (2011) 1644-1648.
- [99] Q. Cao, H. Zhao, L. Zeng, J. Wang, R. Wang, X. Qiu, Y. He, Electrochemical determination of melamine using oligonucleotides modified gold electrodes, *Talanta*, 80 (2009) 484-488.
- [100] C.W. Liao, Y.R. Chen, J.L. Chang, J.M. Zen, A sensitive electrochemical approach for melamine detection using a disposable screen printed carbon electrode, *Electroanalysis*, 23 (2011) 573-576.
- [101] L. Fotouhi, N. Farzinnejad, M. Heravi, S. Khaleghi, Study the electrochemical reduction of some triazines in N, N-dimethylformamide at glassy carbon electrode, *BULLETIN-KOREAN CHEMICAL SOCIETY*, 24 (2003) 1751-1756.

- [102] Y. Kong, C. Wei, Z. Wang, Z. Hou, H. Li, J. Yu, J. Yuan, Y. Zhao, J. Long, Y. Tang, Determination of melamine in quail egg and milk with capillary zone electrophoresis, *American Journal of Analytical Chemistry*, 5 (2014) 258-265.
- [103] H. Akter, A. Shaikh, T.R. Chowdhury, M. Rahman, P. Bakshi, A.S. Ahammad, Gold nanoparticle-modified indium tin oxide electrode for highly sensitive electrochemical detection of melamine, *ECS Electrochemistry Letters*, 2 (2013) B13.
- [104] H. Zhu, S. Zhang, M. Li, Y. Shao, Z. Zhu, Electrochemical sensor for melamine based on its copper complex, *Chemical Communications*, 46 (2010) 2259-2261.
- [105] J. Yue, X. Jiang, Y.V. Kaneti, A. Yu, Deposition of gold nanoparticles on β -FeOOH nanorods for detecting melamine in aqueous solution, *Journal of colloid and interface science*, 367 (2012) 204-212.
- [106] L.Y. Bai, C.X. Dong, Y.P. Zhang, W. Li, J. Chen, Comparative Studies on the Quick Recognition of Melamine Using Unmodified Gold Nanoparticles and p-Nitrobenzenesulfonic Grafted Silver Nanoparticles, *Journal of the Chinese Chemical Society*, 58 (2011) 846-852.
- [107] J.D. Wuest, A. Rochefort, Strong adsorption of aminotriazines on graphene, *Chemical communications*, 46 (2010) 2923-2925.
- [108] S. Zeng, M. Cai, H. Liang, J. Hao, Size-dependent colorimetric visual detection of melamine in milk at 10 ppb level by citrate-stabilized Au nanoparticles, *Analytical Methods*, 4 (2012) 2499-2505.
- [109] C.A. Burtis, D.E. Bruns, *Tietz Fundamentals of Clinical Chemistry and Molecular Diagnostics-E-Book: Tietz Fundamentals of Clinical Chemistry and Molecular Diagnostics-E-Book*, Elsevier Health Sciences 2014.
- [110] Y. Zhong, M. Lin, J. Zhou, Y. Liu, Construction of Electrochemical Sensor Based on Praseodymium Hexacyanoferrate Modified Graphite Electrode and Its Application for Cysteine Determination, *Chinese Journal of Analytical Chemistry*, (2010) 229-232.
- [111] A.A. Ensafi, S. Behyan, Sensing of L-cysteine at glassy carbon electrode using Nile blue A as a mediator, *Sensors and Actuators B: Chemical*, 122 (2007) 282-288.

- [112] S. Sahoo, A.K. Satpati, P.K. Sahoo, P.D. Naik, Incorporation of carbon quantum dots for improvement of supercapacitor performance of nickel sulfide, *ACS omega*, 3 (2018) 17936-17946.
- [113] M.K. Dey, A.K. Satpati, Implication of charge transfer property on the supercapacitive performance of manganese oxide originated through different synthesis routes, *Journal of Electroanalytical Chemistry*, 849 (2019) 113366.
- [114] S. Kumar, S. Bawari, S. Narayanaru, T.N. Narayanan, A.K. Satpati, Enhanced Electron Transfer Kinetics of Covalent Carbon Nanotube Junctions, *The Journal of Physical Chemistry C*, 126 (2021) 239-245.
- [115] A. Sharma, S. Manna, S. Kumar, A.K. Satpati, Bismuth Vanadate and 3D Graphene Composite Photoanodes for Enhanced Photoelectrochemical Oxidation of Water, *ACS omega*, 8 (2023) 33452-33465.
- [116] A. Sharma, S. Manna, A.K. Satpati, Enhancement in photoelectrochemical efficiency and modulation of surface states in BiVO₄ through the TiO₂ outer layer using the atomic layer deposition technique, *The Journal of Physical Chemistry C*, 127 (2023) 4395-4406.
- [117] S. Kumar, A.K. Satpati, Investigation of interfacial charge transfer kinetics of photocharged Co-Bi modified BiVO₄ using scanning electrochemical microscopy (SECM), *Electrochimica Acta*, 368 (2021) 137565.
- [118] S. Kumar, P.K. Sahoo, A.K. Satpati, Insight into the catalytic performance of HER catalysis of noble metal/3D-G nanocomposites, *Electrochimica Acta*, 333 (2020) 135467.
- [119] S. Sahoo, A.K. Satpati, Electrochemical capacitance properties of cobalt oxide entangled over MWCNT and cobalt oxide AC composites, *Journal of Electroanalytical Chemistry*, 801 (2017) 416-424.
- [120] M.K. Dey, P.K. Sahoo, A.K. Satpati, Electrochemically deposited layered MnO₂ films for improved supercapacitor, *Journal of Electroanalytical Chemistry*, 788 (2017) 175-183.
- [121] S. Sahoo, P. Sahoo, A. Satpati, Improvised synthesis of noble metal ion infused nickel sulphide for supercapacitor application, *Materials Today: Proceedings*, 67 (2022) 1109-1113.

- [122] S. Manna, A.K. Satpati, C.N. Patra, A.K. Tyagi, Enhancing the PEC Efficiency in the Perspective of Crystal Facet Engineering and Modulation of Surfaces, *ACS omega*, 9 (2024) 6128-6146.
- [123] A.K. Satpati, Synthesis Strategies and Applications of Metallic Foams and Hollow Structured Materials, *Handbook on Synthesis Strategies for Advanced Materials: Volume-II: Processing and Functionalization of Materials*, (2022) 325-376.
- [124] S. Kumar, S. Ahirwar, A.K. Satpati, Insight into the PEC and interfacial charge transfer kinetics at the Mo doped BiVO₄ photoanodes, *RSC advances*, 9 (2019) 41368-41382.
- [125] S. Shyamal, A. Maity, A.K. Satpati, C. Bhattacharya, Amplification of PEC hydrogen production through synergistic modification of Cu₂O using cadmium as buffer layer and dopant, *Applied Catalysis B: Environmental*, 246 (2019) 111-119.
- [126] S. Shyamal, A. Maity, A.K. Satpati, C. Bhattacharya, Development of Cu₂O thin films under the influence of electrochemical impedance: Applications in improved photoelectrochemical water reduction, *Electrochimica Acta*, 308 (2019) 384-391.

Applications of atomic force microscopy in modern biology

Tathagata Nandi and Sri Rama Koti Ainavarapu*

Department of Chemical Sciences, Tata Institute of Fundamental Research
Dr. Homi Bhabha Road, Colaba, Mumbai 400005, India

*Corresponding author: S.R.K.A

Email: koti@tifr.res.in

Abstract

Single molecule force spectroscopy (SMFS) is an emerging tool to investigate mechanical properties of biomolecules and their responses to mechanical forces, and one of the most-used techniques for mechanical manipulation is the atomic force microscope (AFM). AFM was invented as an imaging tool which can be used to image biomolecules in sub-molecular resolution in physiological conditions. It can also be used as a molecular force probe for applying mechanical forces on biomolecules. In this brief review we will provide exciting examples from recent literature which show how the advances in AFM have enabled us to gain deep insights into mechanical properties and mechanobiology of biomolecules. AFM has been applied to study mechanical properties of cells, tissues, microorganisms, viruses as well as biological macromolecules such as proteins. It has found applications in biomedical fields like cancer biology, where it has been used both in the diagnostic phases as well as drug discovery. AFM has been able to answer questions pertaining to mechanosensing by neurons, and mechanical changes in viruses during infection by the viral particles as well as the fundamental processes such as cell division. Fundamental questions related to protein folding that have been answered by SMFS are, for example, determination of energy landscape properties of variety of proteins to correlate with their biological functions. A multipronged approach is needed to diversify the research, as a combination with optical spectroscopy and computer based steered

molecular dynamic simulations along with SMFS can help us gain further insights into the field of biophysics and modern biology.

1. Introduction

Force has an immense role to play in biology. Starting from DNA replication to cellular motility, biological processes are driven by mechanical forces. Single molecule force spectroscopy (SMFS) has been highly useful for the quantification of such mechanical forces as well as in determining mechanical properties of biomolecules (1–4). In mechanobiology, physical forces are applied on different biomolecules starting from live organisms to tissues and live cells to protein molecules and their responses to such forces are elucidated. Some of the most well-known techniques used for this purpose are AFM, optical tweezers, magnetic tweezers and biomembrane force probe (BFP). In this particular review we will be discussing the recent developments in the field of AFM and its application in modern biology.

AFM helps us to achieve spatial resolutions of nanometer scale and force resolution of piconewtons. Routinely for biological applications, a micrometre-sized cantilever attached with a sharp nanometre-sized tip is used in an AFM setup for the application of force by indentation or stretching and pulling (Fig. 1). AFM is basically an imaging tool which consists of four basic components: the cantilever, the piezoelectric positioner which is either attached to the cantilever or to the sample stage, the laser and the position sensitive detector or the photodiode (5,6). When the cantilever scans over a surface, the interactions between the cantilever-tip and the surface cause the cantilever to bend and the laser beam to deflect. This finally leads to a change in the laser beam position on the position sensitive detector. (1,5,7). Finally, a topographic image of the surface is obtained. AFM imaging can be done both in contact mode and in non-contact mode, and both in air and in liquid conditions, which are explained elsewhere in detail (1,5,6). In addition, AFM can also be used as a single molecule manipulation tool where it can be used as a molecular force probe for dynamic force

spectroscopic (DFS) purpose. In DFS, a single molecule is held between the cantilever-tip and the sample stage, which are moved away from each other using a piezoelectric positioner and as a result force is thus applied on the tethered molecule (8,9). When polyproteins (proteins covalently attached in tandem) are used in DFS, experimental force vs extension curves with sawtooth like patterns are obtained. In these curves, every sawtooth force peak implies the unfolding of a particular domain of the polyprotein. These experiments can give also us stiffness and other mechanical parameters of the molecule. Other experimental details and their varieties and details of the instrumentation of AFM can be found elsewhere (1,3,6,8,10).

Indentation experiments can also be performed yielding force vs extension plots. From these plots by analysing them with suitable models, a wealth of information can be obtained on mechanical properties of the molecules and other physical properties based on their response to forces (2,3,11–13). These experiments can also be used to find out Young's modulus and stress applied using cantilevers of different shapes and sizes (14,15). Smaller the value of the Young's modulus more is the sample susceptible to deformation. Other parameters like adhesion and stiffness can also be calculated. During performing these experiments, the cantilever and the stage can be moved at different velocities and the force depends nonlinearly with the velocity. Therefore, the loading rate must be reported. In other experiments, the force might be kept constant to investigate the changes in the sample's mechanical properties with time (2). Temperature controller and buffers of appropriate pH can be used to replicate physiological conditions.

Further to understand the biological problems more intricately, AFM can be combined with other optical microscopy and fluorescence spectroscopy components (2). As AFM can provide only topography and surface properties, fluorescence sensors for determining mechanical properties inside cells have also been developed (16). Here in this review we would be looking at the recent advances in the field of AFM in determining the mechanical properties

of proteins, cells, tissues, microorganisms and other biomolecules. We shall be discussing exciting examples from literature which showcase these advancements in our understanding of the role of force in biology.

2. AFM studies on cells and tissues

AFM has been extensively used in determining mechanical properties and understanding fundamental role of forces in biology since its inception. Here in this section we shall review few of the most pioneering works where AFM has been used in different kinds of cells and tissues. During cell division, mitotic cell rounding is an important step for fulfilling the geometrical requirements (17). Stewart et al through their work using AFM as well as transmitted light microscopy have shown that the cell rounding forces are dependent on the actomyosin cytoskeleton and the cell's ability to regulate osmolarity (17). The cell rounding forces increase during mitosis. The force is created by the osmotic pressure but maintained by actomyosin cortex. Therefore, finally it was concluded that cells can modulate their volume, shape and mechanical properties by regulating actomyosin cortex dependent surface tension and osmotic pressure (17).

AFM in the force mapping mode has been used to study the dynamic changes in the stiffness of the cortex of adherent cells during the transition from metaphase to cytokinesis (18). This work could answer a very fundamental question in biology that whether the cell division is driven by cortical relaxation outside the equatorial region or cortical contractility in the furrow region (18). With the help of video microscopy and AFM it was concluded that cortical stiffening takes place (increase in Young's modulus) over the equatorial region prior to the appearance of the furrow and the stiffness further increases as the furrowing starts (18).

Neurons extend axons along well-defined pathways during nervous system development. Axon pathfinding is not only mediated by chemical signalling but also

mechanosensing of the surrounding environment (19). Koser et al through their works showed that axon pathfinding is modulated by mechanical signals. In vivo experiments with AFM showed that neuronal growth can sense and respond to stiffness of the surrounding tissues. AFM results also showed stiffness gradients in the embryonic brain (19).

We will discuss an example of AFM used to understand why mammalian neurons do not regenerate after injury? Injuries to the central nervous system (CNS) cause something called glial scarring which inhibits the growth and regeneration of neurons (20). Moeendarbary et al determined mechanical signatures of glial scars using AFM indentation experiments. The spatiotemporal changes in elastic stiffness was characterised for an injured rat neocortex and spinal cord. Compared to other mammalian tissues, neuronal tissues become exceptionally softer after injury. As neuronal growth depends on tissue stiffness therefore this might be a reason for mammalian neurons not regenerating after injury (20).

2.1 AFM in cancer biology

Carcinogenic cells in response to external stimuli, can undergo changes in their morphology, elasticity and other mechanical properties (10). AFM can be extensively used for imaging live cells and obtain information about their mechanical properties and hence can be used for studying cancerous cells and tumour cells. Hence it can be said that AFM has direct application in the field of biomedical diagnosis. There is a detailed review on how AFM has been used in the field of cancer by Deng et al (10). Here we shall discuss some of the most exciting and insightful works on this field.

AFM imaging showed huge number of needle like structures spread across leukemic cells of patients suffering from myeloid leukaemia (Fig. 2) (21). The cell surface roughness was found to increase a lot more than normal white blood cells (21). Studies have indicated that though tumour cells and cancerous cells look similar visually, their mechanical properties

can be widely different (10). Stiffness values were obtained for metastatic cancerous cells of patients and it was observed that the cells are 70% more softer and the standard deviation is almost 5 times narrower than benign cells (22).

Within tumour microenvironment, transition from healthy to malignant condition causes the mechanical properties of the cells to alter (10,23). Using indentation type AFM, stiffness map was obtained for normal tissues, benign tissues and malignant tissues from human breast cancer biopsies (23). For the normal and the benign tissues, the stiffness map showed a single distinct peak. For malignant tissues a broad distribution was observed with a clear low stiffness peak representative of cancer cells (23). Therefore, indentation type AFM provides scope for the quantification in case of clinical diagnostics of breast cancer.

Furthermore, the potential of anticancer drugs can be evaluated by observing their effects on the morphological features and mechanical properties of cancer cells (10). Cancer cells becoming softer can be attributed to the reorganisation of complex cytoskeleton structure and hence it serves as a target for therapeutic purposes (24). AFM has been used to detect topographical and biophysical changes of nasopharyngeal carcinoma cells and normal nasopharyngeal epithelial cells (24). When treated with Disulfiram chelated with Cu^{2+} (DSF-Cu), morphological changes were observed in the cancerous cells. Also, the adhesion force for cancer cells increased. The roughness decreased and the stiffness increased. However, for the normal cells, these effects were absent (24). There are lot of other drug candidates that have been tested on cancer cells and their efficacies judged on the basis of their effects on the surface stiffness, roughness and other morphological properties (10,25,26).

Modified carbon nanoparticles with biomolecules find application in chemical biology as drug delivery agents (27). Muthukumar et al modified carbon nanoparticles by coating them with bovine serum albumin and loading with methotrexate (CBMs). These modified CBMs

were examined with the help of scanning electron microscopy and AFM and significant changes in their morphology and roughness were reported (27). The CBM could achieve sustained drug release. Lung cancer cell line displayed 83% cell death at a particular concentration of the CBMs. This shows that CBMs or other carbon nanostructures can be quickly analysed using AFM and their potential can thus be predicted (10,27). Therefore, AFM can be used for cancer research both in the diagnostic phase as well as the therapeutic phase.

2.2 AFM in microorganisms and viruses

AFM has been used to quantify the mechanical properties of the rigid cell walls lining the microbial cells (28). AFM indentation experiments have been used to investigate the nanomechanical properties of a gram negative bacteria *Shewanella putrefaciens* at two different pH values 4 and 10 (28). The thickness of the cell wall was found to increase with increase in pH which was attributed to the water mobility within the polymeric fringes or from the cytoplasm to periplasm (28). Direct measurement of the cell surface softness was carried out for a fibrillated oral streptococcal strain and a non-fibrillated strain using AFM (29). The fibrillated strain was found to be softer and less stiff than the non-fibrillated strain which was validated by other experimental techniques (29).

The enzyme lysostaphin is a potential antibiotic agent that can be used to lyse the bacteria *Staphylococcus aureus* (30). AFM has been used to scan the structural and physical dynamics of *Staphylococcus aureus* in real time on being treated with lysostaphin (30). The structure and morphological features of the cell surface got hugely changed on addition of lysostaphin. The cell wall stiffness and the bacterial spring constant decreased. These modifications were attributed to the digestion of peptidoglycan by lysostaphin and thus making the bacteria fragile (30). Therefore, AFM helped to analyse the potential of an antibiotic in lysing a specific bacterium (30).

During cell division, in yeast, chitin is known to accumulate in the cell wall in a region involved in budding (31). AFM has been used to generate force maps of the cell surface spatially at different regions. The bud scar region was found to be 10 times stiffer than the surrounding regions (31). This was the first report on spatially resolved force maps of a single microbial cell (31).

During host to host transfer, the shell of the bacteriophage protects the viral DNA (32). The mechanical properties like strength and Young's modulus were calculated for bacteriophage ϕ 29 shell using scanning force microscopy (32). The Young's modulus was found to be \sim 1.8 GPa, which is similar to hard plastic and the shell could withstand nanonewtons of force (32). These results suggest that the mechanical protection ability of the bacteriophage shell is high (32). Hepatitis B is a well-known human pathogen. Nanoindentation experiments using AFM were carried out and the Young's modulus was found to be \sim 0.4 GPa (33).

During maturation, HIV undergoes huge morphological changes (34). Nanoindentation experiments using AFM were conducted on HIV particles. Immature particles are 14-fold stiffer than mature particles that are important for causing infection (Fig. 3) (34). Interestingly, there is a correlation between the softening of the HIV particles and their ability to enter cells. This result was one of the first in which the virus mechanical properties are directly related to infection (34).

AFM studies on proteins and their correlation with the protein function

AFM in the DFS mode has been used to study folding unfolding processes of different proteins to investigate their mechanical stabilities (3,8). The results obtained could be related to the protein's functions. Uropathogenic *Escherichia coli* uses its pili to attach to different tissues (35). The pili are composed of thousands of coiled FimA which forms the pilus rod

region and it is followed by FimF-FimG-FimH proteins which form the tip fibrillum. The domains are locked to each other by β -strand complementation which can withstand high mechanical forces (35). SMFS experiments revealed exceptional mechanical stability of the pilus with a hierarchy of stability (35). The variants close to the pilus rod were found to be more stable (FimA) than the tip region. This sort of mechanical hierarchy might be necessary as the rupturing or unfolding of FimA might dislodge the whole pilus from the bacteria. And overall, the mechanical stability of the pilus is also important for its attachment to tissues (35).

High mechanical stability is required for pathogens to adhere to their targets and cause infection (36). SMFS using AFM was conducted to determine the mechanical stability of staphylococcal adhesin SdrG which targets a small peptide from human fibrinogen b (36). Using steered molecular dynamics simulation (SMD) and SMFS it was confirmed that this SdrG and fibrinogen peptide complex can withstand exceptionally high forces up to 2 nN (36). From the above two examples it can be said that pathogens target their hosts with exceptional mechanostability (35,36).

Cellulosomes are polyprotein machineries which are required for degradation of cellulosic material (37). For this function they have scaffolds which consist of highly structurally homologous cohesin domains. These cohesins are important for the microbe's attachment with the substrate (37). There are two types of cohesins, hanging and bridging (37). The bridging cohesins are believed to be more mechanically important and hence should be able to bear more forces than the hanging cohesins (37). Using one of the main scaffolds ScA, experiments were carried out in an *in vitro* transcription-translation protein pull down assay and it was proved by SMFS that the bridging cohesins are indeed mechanically more stable than the hanging cohesins (37).

Ubiquitin and small ubiquitin related modifiers (SUMO) are proteins from the same family having highly homologous structure with large differences in their amino acid sequence and functions (38). Ubiquitin is primarily noted for its function in proteasome mediated protein degradation whereas SUMOs are not known to associate with this function (39–43). Hence it is expected that ubiquitin should be able to withstand higher amount of force as compared to SUMOs so that the proteasome can effectively degrade the substrate protein and ubiquitin remaining intact (44). SMFS was carried out on these proteins using AFM and indeed ubiquitin in spite of having similar structural motif could withstand the higher forces compared to the SUMOs (38). Further it was proved using ensemble measurements that ubiquitin indeed is thermodynamically and kinetically the most stable protein compared to the SUMOs (45). Apart from these there are number of proteins for which their mechanical unfolding pathways have been studied, starting from periplasmic proteins to metalloproteins (46–48).

Aggregation of amyloidogenic proteins to amyloid fibrils have implications in various neurodegenerative diseases (49,50). There may be structural differences in the aggregates and different stages can be responsible for the diseases. High speed AFM has been used to characterise fibril formation and elongation of amyloid β proteins (49,50). Cell adhesion proteins functions by binding cells together and resist mechanical forces (51). The mechanical properties of proteins like cadherins, selectins, integrins and FimH have been studied using different single molecule force spectroscopy techniques. There exists a detailed review article on the mechanical properties of cell adhesion proteins (51). Another interesting field where AFM has been used extensively is tip links. Tip links act as force sensors and are responsible for the function of hearing (52). The structure of tip link is highly regulated by the Ca^{2+} ions which is bound to the tip link. Mutations at the binding site can give rise to hearing defects. Single molecule FRET and atomic force microscopy have been used to understand the force

sensing properties (52). It was shown that Ca^{2+} rich environment can restore the force-response of the mutant tip-links (52).

The most effective candidate for vaccine of malaria is *Plasmodium falciparum* circumsporozoite protein CSP which is important for structure and motility of the infective sporozoites (53). SMFS using AFM was carried out on different constructs of CSP (Fig. 4) (53). The CSP construct with the central repeat region of amino acids NANP was found to be mechanically heterogeneous with 40% molecules requiring negligible force for unfolding and hence having apparently no mechanical stability, and 60% displaying low mechanical stability (~ 70 pN) (53). This overall low mechanical resistance offered by the repeat region exposed on the surface of sporozoites give them lubricating capacity required to navigate through the host tissues (53).

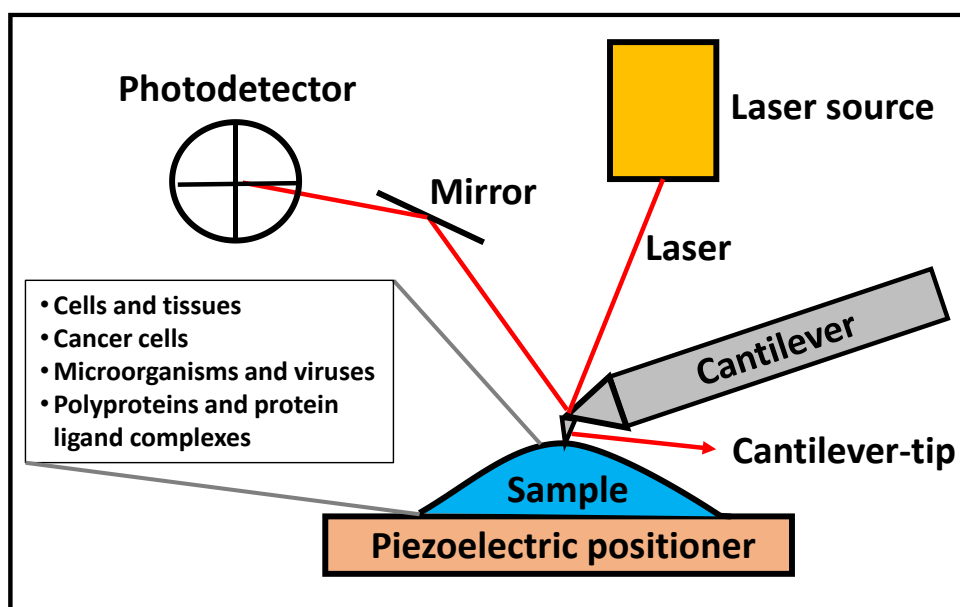


Fig 1. A schematic of a typical AFM experimental set up. The figure shows the most important components of an AFM which have been labelled in the diagram.

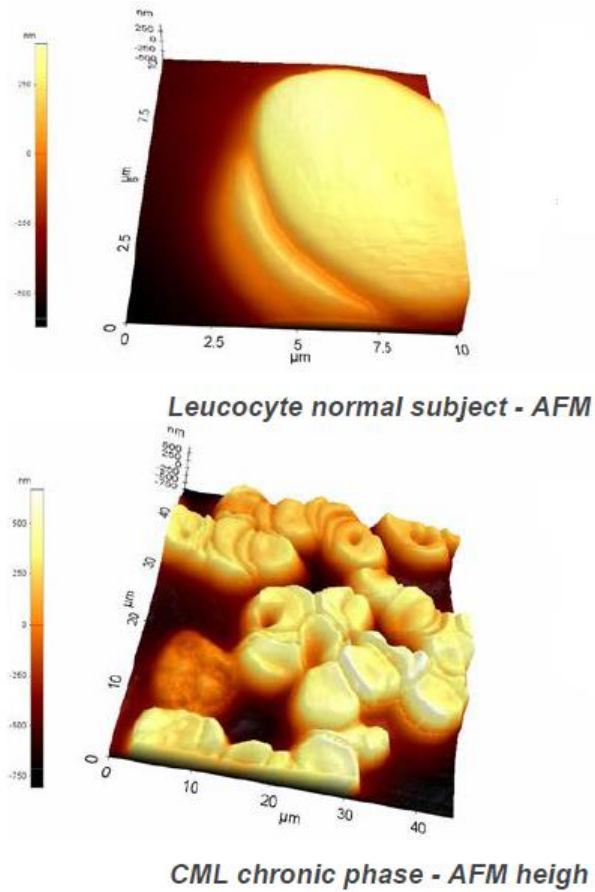


Fig 2. AFM image of leukemic cells. AFM imaging of normal and leukemic leucocytes shows numerous spicule like features on the surface of leukemic cells of patients suffering from chronic myeloid leukaemia. Figure reprinted with permission. This research was originally published in Current Health Sciences Journal. Gaman A et al. Surface morphology of leukemic cells from chronic myeloid leukemia under atomic force microscopy. *Curr Heal Sci J.* 2013; 39(1):45–47.

Fig 3.

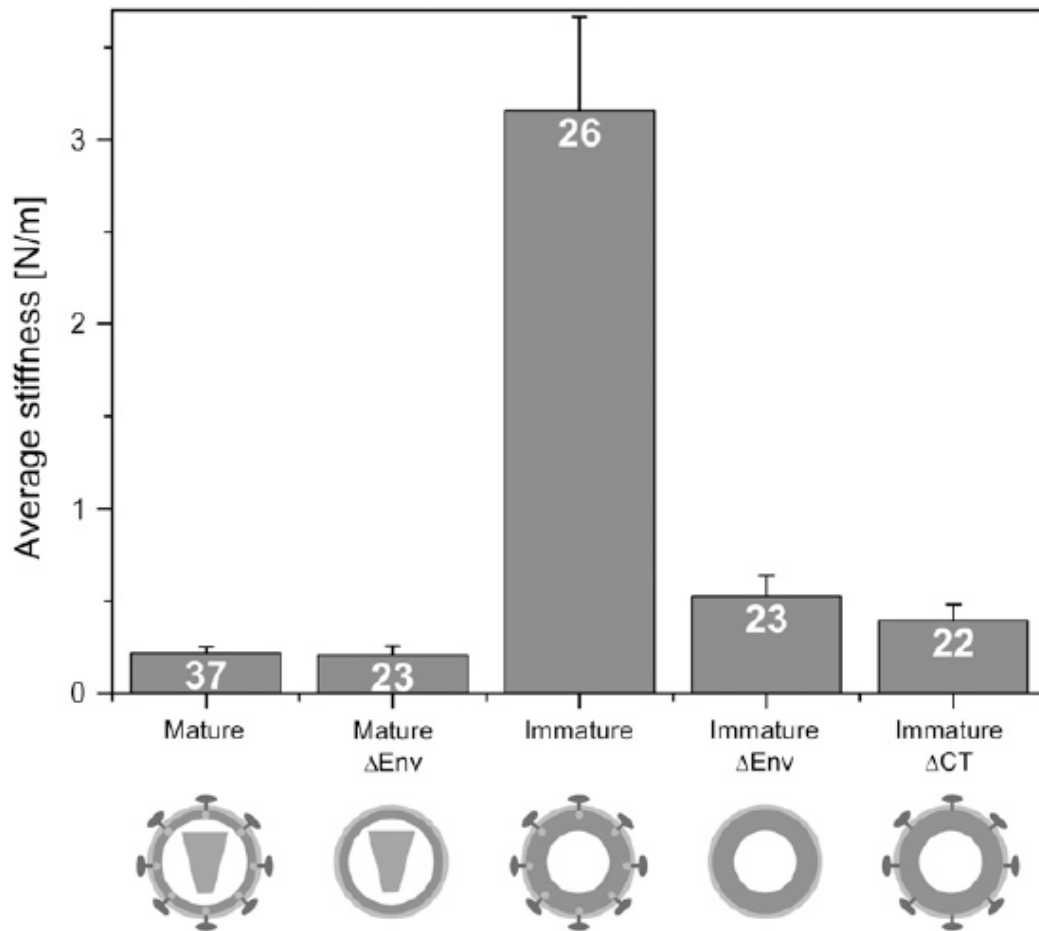


Fig 3. Average stiffness values of HIV particles at different stages. The immature particle is stiffer than the matured ones. The number of virions analysed have been mentioned within the histograms. Figure reprinted with permission. This research was originally published in Biophysical Journal. Kol et al. A stiffness switch in human immunodeficiency virus. Biophys J. 2007; 92(5):1777–83. License Number- 4927601272255.

Fig 4.

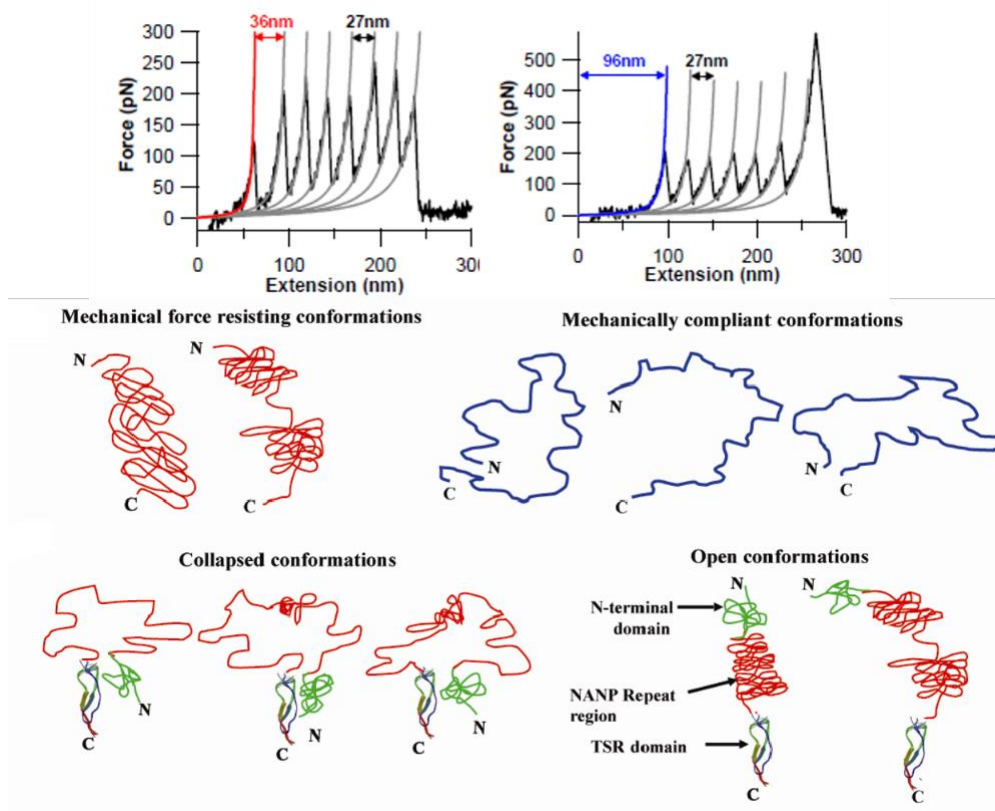


Fig 4. SMFS using AFM on different constructs of *Plasmodium falciparum* CSP. Mechanical heterogeneity can be seen among the CSP and also its overall low mechanical stability depicted by the typical sawtooth profiles. Cartoon representations of different possible conformations of CSP. Figure reprinted with permission. This research was originally published in the Journal of Biological Chemistry. Patra et al. Force Spectroscopy of the Plasmodium falciparum vaccine candidate circumsporozoite protein suggests a mechanically pliable repeat region. J Biol Chem. 2017; 292:2110-2119. © the American Society for Biochemistry and Molecular Biology.

3. Conclusion

Therefore, we have understood the potential of AFM in resolving a lot of fundamental biological questions. We have seen how AFM can be used in live cells and tissues and to understand their mechanosensing properties. We have discussed about its role in cancer research both in diagnosis as well as drug discovery. We have discussed how AFM has been used to investigate the mechanical properties of microorganisms and viruses and how force can play important roles in processes like cell division, antibiotic activity. The mechanical properties of viral shells have also been determined as well as the relationship between mechanical properties and viral infection abilities. Here we have discussed its role in mechanobiology and biomedical fields, but AFM has been used extensively in mechanochemistry also (9). Various mathematical models for the analysis are there and many are yet to be developed which can be useful in answering more valuable questions. Force spectroscopy is a growing field and there are continuous advances both from technological perspectives as well as its field of application. In future, AFM combined with other techniques such as optical microscopy should address more pressing questions related to force in biology.

4. ACKNOWLEDGEMENTS

S.R.K.A. acknowledges the financial support of the Department of Atomic Energy (DAE), India under Project No. 12-R&DTFR-5.10-0100.

5. References

1. Neuman KC, Nagy A. Single-molecule force spectroscopy: Optical tweezers, magnetic tweezers and atomic force microscopy. *Nat Methods*. 2008;5(6):491–505.
2. Krieg M, Fläschner G, Alsteens D, Gaub BM, Roos WH, Wuite GJL, et al. Atomic force microscopy-based mechanobiology. *Nat Rev Phys*. 2019;1(1):41–57.

3. Hughes ML, Dougan L. The physics of pulling polyproteins: A review of single molecule force spectroscopy using the AFM to study protein unfolding, *Reports on Progress in Physics*. 2016.; 79:1-40.
4. Neuman KC, Lionnet T, Allemand JF. Single-molecule micromanipulation techniques. *Annu Rev Mater Res*. 2007;37:33–67.
5. Chang KC, Chiang YW, Yang CH, Liou JW. Atomic force microscopy in biology and biomedicine. *Tzu Chi Med J* . 2012;24(4):162–9.
6. Dufrêne YF. Atomic force microscopy, a powerful tool in microbiology. *J Bacteriol*. 2002;184(19):5205–13.
7. Binnig G, Quate CF, Gerber C. Atomic force microscope. *Phys Rev Lett*. 1986;56(9):930–3.
8. Carrion-Vazquez M, Oberhauser AF, Fisher TE, Marszalek PE, Li H, Fernandez JM. Mechanical design of proteins studied by single-molecule force spectroscopy and protein engineering. *Prog Biophys Mol Biol*. 2000;74(1–2):63–91.
9. Do JL, Friščić T. Mechanochemistry: A Force of Synthesis. *ACS Cent Sci*. 2017;3(1):13–9.
10. Deng X, Xiong F, Li X, Xiang B, Li Z, Wu X, et al. Application of atomic force microscopy in cancer research. *J Nanobiotechnology*. 2018;16(1):1-15.
11. Bustamante C, Marko JF, Siggia ED, Smith S. Entropic elasticity of λ -phage DNA., *Science*. 1994;265:1599–600.
12. Oberhauser AF, Marszalek PE, Erickson HP, Fernandez JM. The molecular elasticity of the extracellular matrix protein tenascin. *Nature*. 1998;393(6681):181–5.
13. Hertz H. Ueber die Berührung fester elastischer Körper. *J für die Reine und Angew Math*. 1882;1882(92):156–71.
14. Fischer-Friedrich E, Hyman AA, Jülicher F, Müller DJ, Helenius J. Quantification of surface tension and internal pressure generated by single mitotic cells. *Sci Rep*. 2014;4:4–11.
15. Vorselen D, Kooreman ES, Wuite GJL, Roos WH. Controlled tip wear on high roughness surfaces yields gradual broadening and rounding of cantilever tips. *Sci Rep* [Internet]. 2016;6(July):1–7. Available from: <http://dx.doi.org/10.1038/srep36972>
16. Polacheck WJ, Chen CS. Measuring cell-generated forces: A guide to the available tools, *Nature Methods*. 2016;13:415–23.
17. Stewart MP, Helenius J, Toyoda Y, Ramanathan SP, Muller DJ, Hyman AA. Hydrostatic pressure and the actomyosin cortex drive mitotic cell rounding. *Nature* [Internet]. 2011;469(7329):226–31.
18. Matzke R, Jacobson K, Radmacher M. Direct, high-resolution measurement of furrow stiffening during division of adherent cells. *Nat Cell Biol*. 2001;3(6):607–10.
19. Koser DE, Thompson AJ, Foster SK, Dwivedy A, Pillai EK, Sheridan GK, et al. Mechanosensing is critical for axon growth in the developing brain. *Nat Neurosci*. 2016;19(12):1592–8.

20. Moeendarbary E, Weber IP, Sheridan GK, Koser DE, Soleman S, Haenzi B, et al. The soft mechanical signature of glial scars in the central nervous system. *Nat Commun.* 2017;8:1–11.
21. Gaman A, Osiac E, Rotaru I, Taisescu C. Surface morphology of leukemic cells from chronic myeloid leukemia under atomic force microscopy. *Curr Heal Sci J.* 2013;39(1):45–47.
22. Cross SE, Jin YS, Rao J, Gimzewski JK. Nanomechanical analysis of cells from cancer patients. *Nat Nanotechnol.* 2007;2(12):780–3.
23. Plodinec M, Loparic M, Monnier CA, Obermann EC, Zanetti-Dallenbach R, Oertle P, et al. The nanomechanical signature of breast cancer. *Nat Nanotechnol.* 2012;7(11):757–65.
24. Yang Y, Li M, Sun X, Zhou C, Wang Y, Wang L, et al. The selective cytotoxicity of DSF-Cu attributes to the biomechanical properties and cytoskeleton rearrangements in the normal and cancerous nasopharyngeal epithelial cells. *International Journal of Biochemistry and Cell Biology.* Elsevier Ltd; 2017;84:96–108.
25. Wang J, Wan Z, Liu W, Li L, Ren L, Wang X, et al. Atomic force microscope study of tumor cell membranes following treatment with anti-cancer drugs. *Biosens Bioelectron.* 2009;25(4):721–7.
26. Venkatesan P, Das S, Krishnan MMR, Chakraborty C, Chaudhury K, Mandal M. Effect of AEE788 and/or Celecoxib on colon cancer cell morphology using advanced microscopic techniques. *Micron.* 2010;41(3):247–56.
27. Muthukumar T, Prabhavathi S, Chamundeeswari M, Sastry TP. Bio-modified carbon nanoparticles loaded with methotrexate Possible carrier for anticancer drug delivery. *Mater Sci Eng C [Internet].* 2014;36(1):14–9.
28. Gaboriaud F, Bailet S, Dague E, Jorand F. Surface structure and nanomechanical properties of *Shewanella putrefaciens* bacteria at two pH values (4 and 10) determined by atomic force microscopy. *J Bacteriol.* 2005;187(11):3864–8.
29. Van Der Mei HC, Busscher HJ, Bos R, De Vries J, Boonaert CJP, Dufrêne YF. Direct probing by atomic force microscopy of the cell surface softness of a fibrillated and nonfibrillated oral streptococcal strain. *Biophys J.* 2000;78(5):2668–74.
30. Francius G, Domenech O, Mingeot-Leclercq MP, Dufrêne YF. Direct observation of *Staphylococcus aureus* cell wall digestion by lysostaphin. *J Bacteriol.* 2008;190(24):7904–9.
31. Touhami A, Nysten B, Dufrêne YF. Nanoscale mapping of the elasticity of microbial cells by atomic force microscopy. *Langmuir.* 2003;19(11):4539–43.
32. Ivanovska IL, De Pablo PJ, Ibarra B, Sgalari G, MacKintosh FC, Carrascosa JL, et al. Bacteriophage capsids: Tough nanoshells with complex elastic properties. *Proc Natl Acad Sci U S A.* 2004;101(20):7600–5.
33. Uetrecht C, Versluis C, Watts NR, Roos WH, Wuite GJL, Wingfield PT, et al. High-resolution mass spectrometry of viral assemblies: Molecular composition and stability of dimorphic hepatitis B virus capsids. *Proc Natl Acad Sci U S A.* 2008;105(27):9216–20.

34. Kol N, Shi Y, Tsvitov M, Barlam D, Shneck RZ, Kay MS, et al. A stiffness switch in human immunodeficiency virus. *Biophys J* . 2007;92(5):1777–83.
35. Alonso-Caballero A, Schönfelder J, Poly S, Corsetti F, De Sancho D, Artacho E, et al. Mechanical architecture and folding of *E. coli* type 1 pilus domains. *Nat Commun*. 2018;9(1):1-11.
36. Milles LF, Schulten K, Gaub HE, Bernardi RC. Molecular mechanism of extreme mechanostability in a pathogen adhesin. *Science*. 2018;359(6383):1527–33.
37. Verdorfer T, Bernardi RC, Meinhold A, Ott W, Luthey-Schulten Z, Nash MA, et al. Combining in Vitro and in Silico Single-Molecule Force Spectroscopy to Characterize and Tune Cellulosomal Scaffoldin Mechanics. *J Am Chem Soc*. 2017;139(49):17841–52.
38. Kotamarthi HC, Sharma R, Koti Ainaravapu SR. Single-molecule studies on polySUMO proteins reveal their mechanical flexibility. *Biophys J* [Internet]. 2013;104(10):2273–81. Available from: <http://dx.doi.org/10.1016/j.bpj.2013.04.008>
39. Müller S, Hoegge C, Pyrowolakis G, Jentsch S. Sumo, ubiquitin’s mysterious cousin. *Nat Rev Mol Cell Biol*. 2001;2(3):202–10.
40. Hay RT. SUMO: A history of modification. *Mol Cell*. 2005;18(1):1–12.
41. Gill G. SUMO and ubiquitin in the nucleus: Different functions, similar mechanisms? *Genes Dev*. 2004;18(17):2046–59.
42. Pickart CM, Eddins MJ. Ubiquitin: Structures, functions, mechanisms. *Biochim Biophys Acta - Mol Cell Res*. 2004;1695(1–3):55–72.
43. Deol KK, Lorenz S, Strieter ER. Enzymatic Logic of Ubiquitin Chain Assembly. *Front Physiol*. 2019;10(July):1–14.
44. Carrion-Vazquez M, Li H, Lu H, Marszalek PE, Oberhauser AF, Fernandez JM. The mechanical stability of ubiquitin is linkage dependent. *Nat Struct Biol*. 2003;10(9):738–43.
45. Nandi T, Yadav A, Ainaravapu SRK. Experimental comparison of energy landscape features of ubiquitin family proteins. *Proteins Struct Funct Bioinforma*. 2020;88:449-461
46. Yadav A, Paul S, Venkatramani R, Ainaravapu SRK. Differences in the mechanical unfolding pathways of apo- and copper-bound azurins. *Sci Rep*. 2018;8(1).
47. Kotamarthi HC, Narayan S, Ainaravapu SRK. Mechanical unfolding of ribose binding protein and its comparison with other periplasmic binding proteins. *J Phys Chem B*. 2014;118(39):11449–54.
48. Kotamarthi HC, Sharma R, Narayan S, Ray S, Ainaravapu SRK. Multiple unfolding pathways of leucine binding protein (LBP) probed by single-molecule force spectroscopy (SMFS). *J Am Chem Soc*. 2013;135(39):14768–74.
49. Watanabe-Nakayama T, Ono K, Itami M, Takahashi R, Teplow DB, Yamada M. High-speed atomic force microscopy reveals structural dynamics of amyloid β 1-42 aggregates. *Proc Natl Acad Sci U S A*. 2016;113(21):5835–40.
50. Milhiet PE, Yamamoto D, Berthoumieu O, Dosset P, le Grimellec C, Verdier JM, et al.

- Deciphering the structure, growth and assembly of amyloid-like fibrils using high-speed atomic force microscopy. *PLoS One*. 2010;5(10):1–8 .
51. Rakshit S, Sivasankar S. Biomechanics of cell adhesion: How force regulates the lifetime of adhesive bonds at the single molecule level. *Phys Chem Chem Phys*. 2014;16(6):2211–23.
 52. Hazra JP, Sagar A, Arora N, Deb D, Kaur S, Rakshit S. Broken force dispersal network in tip-links by the mutations at the Ca²⁺-binding residues induces hearing-loss. *Biochem J*. 2019;476(16):2411–25.
 53. Patra AP, Sharma S, Ainarapu SRK. Force spectroscopy of the *Plasmodium falciparum* vaccine candidate circumsporozoite protein suggests a mechanically pliable repeat region. *J Biol Chem*. 2017;292(6):2110–9.

Rational Designing of Nickel-Iron Containing Layered Double Hydroxide [NiFe@LDH] Electrocatalysts for Effective Water Splitting

Madasu Sreenivasulu¹, and Nagaraj P. Shetti^{1,2*}

¹Center for Energy and Environment, School of Advanced Sciences, KLE Technological University, Hubballi-580031, Karnataka, India.

²University Center for Research & Development (UCRD), Chandigarh University, Gharuan, Mohali, 140413, Panjab, India

Corresponding author: dr.npshetti@gmail.com (Nagaraj P. Shetti)

Abstract

The development and creation of cost-effective, chemically robust electrocatalysts to aid in the oxygen evolution reaction (OER) and hydrogen evolution reaction (HER) represent significant challenges within the realm of electrocatalytic water electrolysis. In this study, we synthesized a highly competent electroactive catalyst comprising nickel-iron layered double hydroxide (LDH) using a simple hydrothermal approach. The resultant structure, characterized by well-interconnected metal ions arranged in nano-spherical architectures, facilitated the formation of an enhanced electrochemical surface area rich in catalytically active sites, exhibiting harmonious effects. Maintaining the appropriate stoichiometric balance, exemplified by NiFe@LDH, proved essential in augmenting catalytic behavior for both OER and HER. The catalysts NiFe@LDH demonstrated overpotentials of 260 mV (76 mV dec^{-1}) for OER and 138 mV (83 mV dec^{-1}) for HER, achieving a current density of 10 mA cm^{-2} in 1M KOH. Furthermore, NiFe@LDH showcased remarkable durability, enduring up to 100 hours with a marginal reduction in current density of 4.2% and 3.2% for OER and HER, correspondingly. Significantly, in the bifunctional two-electrode configuration featuring NiFe@LDH/NF//NiFe@LDH/NF, efficient electrolysis was achieved, maintaining a stable 10 mA cm^{-2} at a bias of 1.57 V for over 150 hours, with a negligible of 4.6% current loss.

1. Introduction

The high energy density, low environmental impact, and light weight of hydrogen make it a preferable substitute to fossil fuels for energy provision in the future.¹ High-purity hydrogen can be produced through electrocatalytic water disintegration, which stands as one of the most efficient and promising methodologies.^{2, 3} Investigating active catalysts for the anodic OER and cathodic HER is crucial for accelerating the slow kinetics of water electrolysis. Noble metal electrocatalysts, like those based on Pt for HER and (Ir) or Ru for OER, have attracted significant interest due to their outstanding electrocatalytic effectiveness in boosting reaction rates and minimizing overpotentials.⁴ However, their limited abundance, insufficient durability, and high expense hinder their wider practical application.^{5, 6} Consequently, substantial efforts have been devoted to designing effective non-precious materials proficient of catalyzing both the HER and OER.⁷ Despite notable progress, most catalysts demonstrate superior performance in either the HER or OER, requiring separate catalyst materials for the anode and cathode. This discrepancy in catalysts could result in increased production and operational expenses due to electrode mismatch and instability in water-splitting applications. Therefore, it is a crucial requirement to synthesize efficient bifunctional catalysts for the entire process of water electrolysis. Bifunctional catalysts proficient of facilitating both the HER and the OER have garnered significant attention, with LDHs emerging as particularly promising candidates. This interest stems from their unique two-dimensional (2D) structure, adaptable compositions, and abundant availability of raw materials. LDHs can be synthesized using various transition elements abundant in the earth's crust, such as nickel (Ni), copper (Cu), iron (Fe), and cobalt (Co), imparting them with electrocatalytic properties.⁸⁻¹⁰ In particular, note are nickel-based LDHs (Ni-LDHs), including NiV-LDH, NiCo-LDH, and NiFe-LDH, which have gained increased attention because of their environmentally benign attributes, cost-effectiveness, and high catalytic efficiency.¹¹⁻¹³ In the field of OER, previously studied nickel-

based LDHs (Ni-LDHs) catalysts have shown improved OER performance, which can be further enhanced by incorporating vanadium (V), manganese (Mn), and chromium (Cr) ions through doping techniques.¹⁴⁻¹⁶ The generation of the OH* intermediate during OER is significantly facilitated by the tailored intercalation of nickel (Ni) and iron (Fe) into Ni-LDHs. Conversely, in the context of HER, the electrocatalytic efficacy of Ni-based LDHs needs to be further intensified to address their inherent high overpotential and limited durability during HER.¹⁷⁻¹⁹ To enhance the HER behavior of nickel-based LDHs (Ni-LDHs) and advance the development of bifunctional catalysts, various methodologies have been developed. These approaches include designing hierarchical heterostructures and incorporating dopant atoms. Previously reported methods for synthesizing NiFe@LDH include Co-precipitation, where precise control over composition and morphology is challenging, Solvothermal synthesis, which is complex and potentially costly due to organic solvents, Electrodeposition, limited to thin films and requires precise deposition parameter control, and the Sol-gel method, which is time-consuming and involves multiple steps. Hydrothermal synthesis yields highly crystalline LDHs through a controlled high-temperature environment, promoting well-defined crystal growth. The autoclave's closed system minimizes contamination, ensuring high-purity products. This method allows precise control over particle size and morphology, enabling the production of uniform LDH particles. Adjusting parameters like temperature and pressure tailors the LDH structure for specific applications. Hydrothermally synthesized LDHs exhibit enhanced thermal stability and superior mechanical properties. This method is suitable for scaling up, ensuring consistent quality, generating fewer by-products, and improving efficiency. It accommodates a range of metal cations and functional groups, enhancing material applicability and reducing synthesis time.²⁰⁻²² As previously indicated, integrating hierarchical structures into LDH catalysts can enhance surface area and active sites, thereby improving performance in the HER. At the same time, enhancing the OER activity via element doping is

also worth considering. A promising approach for developing efficient catalysts capable of complete water splitting in nickel-based LDHs involves integrating hierarchical assembly with element incorporation.

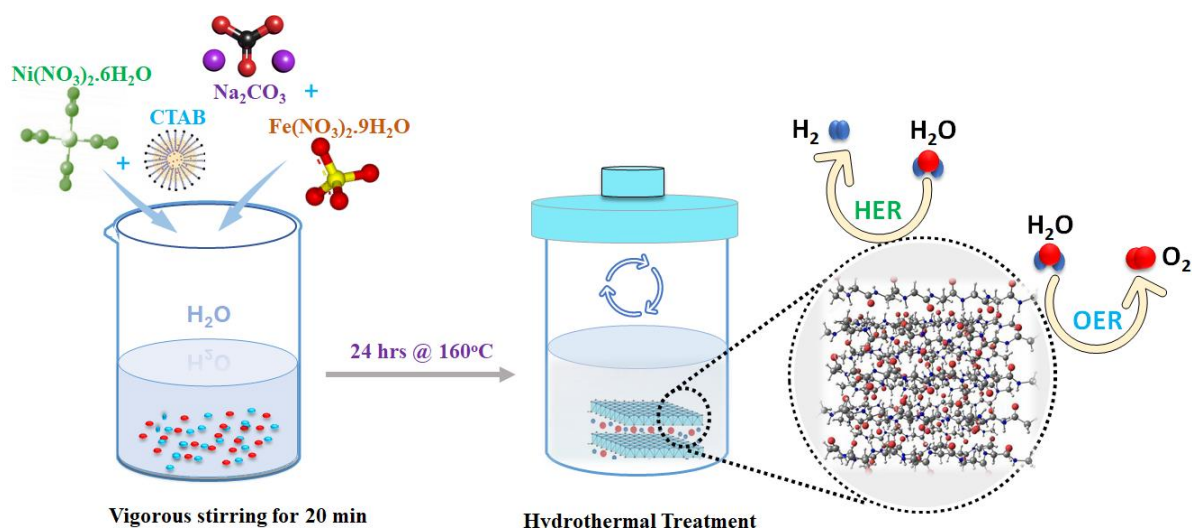
In light of this, a straightforward and environmentally benign hydrothermal method has been developed to generate an extremely durable, active, and effective bifunctional LDH, catalyst for electrolysis. The synthesized catalyst, NiFe@LDH, was applied onto nickel foam substrates to fabricate electrodes for assessing electrocatalytic performance. This electrocatalyst demonstrated excellent behavior for both the OER and HER, achieving fewer overpotentials of 260 mV and 138 mV, correspondingly, to attain a current density of 10 mA cm⁻². Moreover, excellent operational stability was observed over a period of 100 hours. To assess its bifunctional properties, two-electrode configurations employing NiFe@LDH-coated NF electrodes (NiFe@LDH/NF//NiFe@LDH/NF) were utilized, achieving a potential of 1.57 V vs RHE (Reversible Hydrogen Electrode) to achieve a current density of 10 mA cm⁻², with excellent stability maintained for 150 hours. In comparison to commercial catalysts like Pt/C and IrO₂, the bifunctional NiFe@LDH/NF revealed significant electrocatalytic behavior. In-situ surface oxidation studies conducted during the OER and HER processes revealed a synergistic effect influencing the evolution of oxygen and hydrogen.

2. Chemicals and methods

The (Ni(NO₃)₂·6H₂O), Nickel nitrate hexahydrate Hydrochloric acid (HCl), Sodium hydroxide (NaOH), (Fe(NO₃)₂·9H₂O) Ferrous nitrate nonahydrate, Sodium carbonate Na₂CO₃, were obtained from SDF Chemicals. The Commercial IrO₂ (≥ 99.9%) Pt/C (10 wt%), Nafion (5 wt%) KOH flakes (potassium hydroxide, ≥ 85%), HCl (hydrochloric acid, ≥ 38%) C₂H₅OH (ethanol, ≥ 99.9%), Nickel foam (NF), Acetone (≥ 99%) were supplied by Sigma Aldrich.

2.1 Hydrothermal designing of NiFe@LDH

The electroactive catalyst NiFe@LDH was synthesized via a modest single-step hydrothermal approach, approximately 2mmole of Nickel nitrate hexahydrate $\text{Ni}(\text{NO}_3)_2 \cdot 6\text{H}_2\text{O}$, 1mmole of Ferrous nitrate nonahydrate $\text{Fe}(\text{NO}_3)_2 \cdot 9\text{H}_2\text{O}$, is dissolved in 80 ml of NaOH (12mmoles) later 1.04mmole of sodium carbonate and 1mmole of CTAB was added gradually under constant vigorous stirring for 30 min at 950 rpm, later the contents were decanted into the Teflon lined autoclave and allow for undergoing hydrothermal reaction for 24 hrs at 180°C , later it was cool down to 28°C and the contents are cleaned with acetone and ethanol (Scheme 1). $\text{Ni}(\text{OH})_2$ and $\text{Fe}(\text{OH})_2$ were also created by applying a similar procedure for electroactive comparison, (SI-I).



Scheme 1. Synthesis of electroactive catalyst NiFe@LDH.

2.2 Fabrication of NiFe@LDH

Before deposition, the nickel foam (0.5 cm x 0.5 cm, deposition area) underwent a cleaning process, which involved immersion in 0.1 M HCl for about 15 minutes, followed by sonication in acetone for 15 minutes, and concluding with rinsing in ethanol and water for 15 minutes. The active catalyst, specifically nickel-iron LDH (NiFe@LDH), weighing 10 mg, was subjected to sonication for 20 minutes in a mixture consisting of 20 μl solution of Nafion (5 wt%), ethanol ($\text{C}_2\text{H}_5\text{OH}$) of 60 μl , and 60 μl of distilled water to achieve uniform dispersion. Subsequently, a 50 μl dispersion was drop-casted on the NF and then dry out at 70°C in the

oven for 10 minutes. Approximately 4 mg cm^{-2} of material was drop-cast onto the nickel foam. Following the drop-casting of NiFe@LDH onto the nickel foam, the electrodes were dried at 70°C before measurement. Similarly, for comparison, commercial IrO_2 , Pt/C, $\text{Fe}(\text{OH})_2$, and $\text{Ni}(\text{OH})_2$ catalyst ink were, and bare nickel foam was used without further alteration.

2.3 Physicochemical characterization

Powdered electrocatalysts were utilized to investigate surface morphologies and perform various physicochemical analyses. Structural characterization was evaluated using X-ray diffraction (XRD) and Fourier transform infrared (FT-IR) spectroscopy. XRD calibrations were carried out with a Rigaku Smart Lab diffractometer using $\text{Cu K}\alpha$ radiation ($\lambda = 1.5406 \text{ \AA}$) at 40 mA and 40 kV. FT-IR spectra were obtained with a Shimadzu IR Tracer-100 instrument. The oxidation states and elemental conformation of the synthesized materials were assessed using X-ray photoelectron spectroscopy (XPS) with a JEOL Japan-9030 instrument equipped with a monochromated $\text{Al K}\alpha$ (150 W) source. Morphological characteristics were inspected using a Hitachi S-4700 scanning electron microscope (SEM) operating at 20 kV, coupled with an energy-dispersive X-ray spectrometer (EDS). Transmission electron microscopy (TEM) investigation was accomplished with a JEOL JEM-2100 instrument at 120 kV.

2.4 Electrochemical characterization

All electrochemical investigations were evaluated utilizing the traditional 3-electrode system. This system comprised 1 M KOH as the electrolyte, a Pt wire as the counter electrode, an Ag/AgCl electrode (saturated with KCl) as the reference electrode, and the active catalyst coated on nickel foam (NF) as the working electrode. The experimental setup employed a CHI D630 electrochemical analyzer manufactured in the USA. Linear sweep voltammetry (LSV) studies were conducted at a very low scan rate of 10 mV s^{-1} to analyze the OER and HER. The potential range covered by LSV was 1.0 to 1.8 V vs RHE for the OER and 0.0 to -0.4 V vs.

RHE for the HER. Electrochemical impedance spectroscopy (EIS) experiments were measured with an open-circuit voltage of 0.52 V AC dither applied across a frequency range of 1 Hz to 10 kHz. The stability of the HER and OER processes over time was evaluated at specified overpotentials of 138 mV and 260 mV, correspondingly, with the objective of achieving a current density of 10 mA cm⁻² for 100 hours. Overpotentials for the OER were determined using Equation 1.

$$\text{Overpotential, } \eta \text{ (V)} = E_{\text{RHE}} - 1.23 \quad (1)$$

The Nernst equation was utilized to standardize all calibrated potentials to the RHE in the following manner:

$$E_{\text{RHE}} = E_{\text{Ag/AgCl}} + 0.197 + 0.059 \text{ pH} \quad (2)$$

The turnover frequency (TOF) was measured using Equation 4 provided in this document:

$$\text{TOF} = j S / 4 F m \quad (3)$$

In this context, "S" represents NF active surface area, "F" is the Faraday constant (96485.30 C mol⁻¹), "m" indicates the amount of laden catalyst, and "J (mA cm⁻²)" signifies the current density at a potential of 1.65 V.

2.5 Calculations of Faradaic efficiency

During the stability test, the O₂ and H₂ evolved at the anode and cathode, correspondingly, are quantified using the water-gas displacement method. The estimated yield of oxygen produced is calculated using the equation provided below (Equation 4)

$$\text{Faradaic efficiency} = x\text{H}_2 / (Q/nF) \quad (4)$$

In this context, xH₂ represents the amount of hydrogen or oxygen produced by utilizing the total charge Q. Here, 'n' indicates the quantity of electrons that participated in water splitting (4 moles of e⁻s per 1 mole of O₂), while 'F' represents the Faraday constant.

3. Results and discussion

3.1 Chemical phase analysis

The interaction among Nickel nitrate, Ferrous nitrate, Na_2CO_3 , and CTAB varying proportions of these precursors in hydrothermal synthesis yields the active catalyst, the structure, stoichiometry, and constitution of the LDH, and refined methodology profoundly influences catalytic behavior of the catalyst. The XRD design of the electrocatalysts is depicted in [Figure 1a](#). NiFe@LDHs demonstrated a hexagonal structure (JCPDS 26-1286) with characteristic peaks obtained at 11.65° , 23.49° , 34.40° , 39.23° , 46.47° , 59.75° , and 61.19° , related to the (0 0 6), (0 0 1 2), (2 0 4), (2 0 1 0), (2 0 1 6), (2 2 0), and (2 1 2 0) crystallographic planes, respectively. The molecular vibrations of the incorporated anions within the LDH were examined using FT-IR spectroscopy. The broad bands observed in the range of $3300\text{-}3500\text{ cm}^{-1}$ correspond to the stretching vibrations of O-H bonds within the brucite-like layers.²³ The 1637 cm^{-1} band can be allotted to vibrations of the cohering H_2O molecules.²⁴ The vibrations of the intercalated CO_3^{2-} anions are represented by the band at 1358 cm^{-1} ([Figure 1b](#)).^{24, 25} The distinctive peaks between 400 and 800 cm^{-1} in the catalyst show the existence of the inherent stretching vibrations of the Fe-O, Ni-O, and Ni-O-Fe bonds.^{23, 24} The Phase identification for the NiFe@LDH samples was investigated through XRD examination.

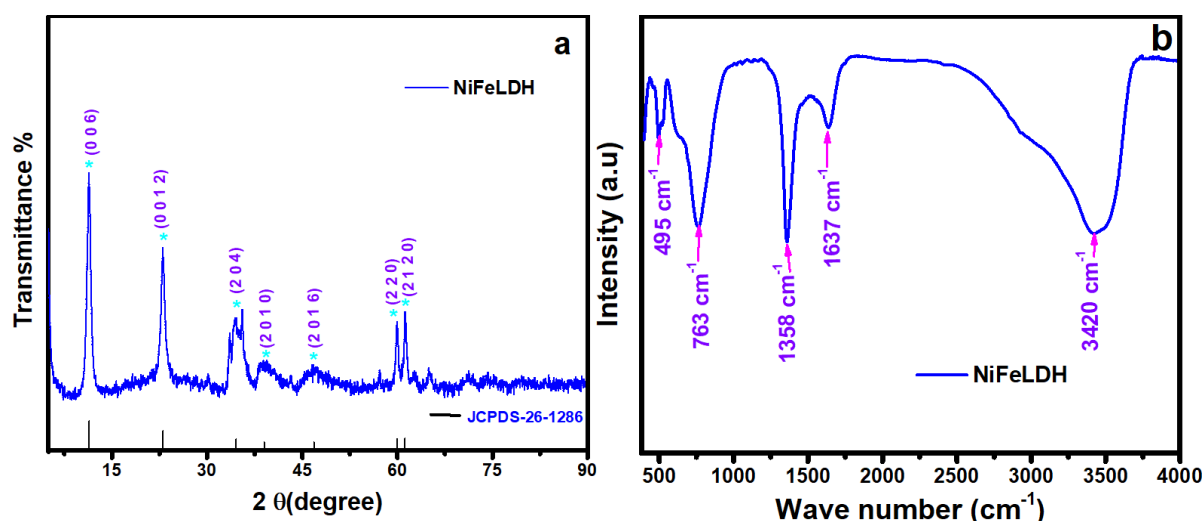


Figure 1. a) The XRD pattern and b) FT-IR spectrum of NiFe@LDH.

The SEM images of NiFe@LDH reveal asymmetric spherical nanostructures of varying diameters with smooth surfaces (Figures 2a & 2b). Nano-spherical structures exhibit unique electronic features due to quantum confinement and altered band structures, enhancing electronic conductivity and optimizing energy levels. Their large surface area-to-volume ratio provides improved active sites, improving mass transport and reaction kinetics. These structures facilitate efficient charge transfer, crucial for HER and OER, ensuring effective electron and hole transport. Their morphology enhances stability and durability, reducing catalyst degradation. Composed of various materials, they benefit from synergistic effects, boosting catalytic activity. Tailored surface energy optimizes reaction intermediates

adsorption, lowering activation energy barriers and increasing reaction rates. These factors make nano-spherical structures highly effective electrochemical catalysts.²⁶

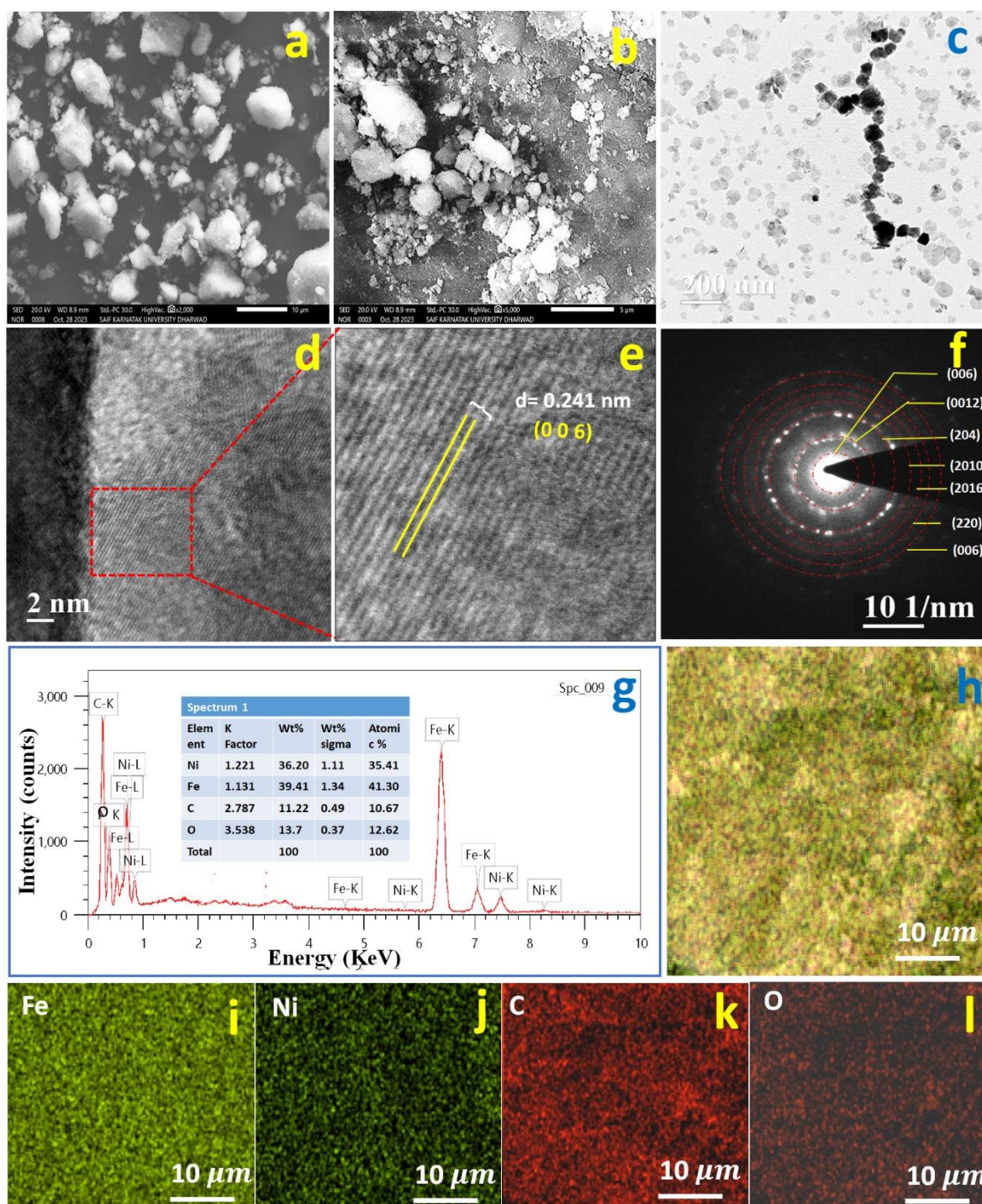


Figure 2. (a, b) Images of SEM: (c) image of HR-TEM; (d & e) NiFe@LDH lattice structure (f) SAED pattern and (g) EDS spectrum (h) Elemental-color mapping i) Iron; e) Nickel; f) Carbon; g) Oxygen.

The HR-TEM was utilized to investigate the nanostructure of the NiFe@LDH catalyst. The interconnected spherical architectures of the catalyst exhibit enhanced surface area, which improves mass transport and promotes synergetic effects, ultimately enhancing overall activity (Figure 2c).²⁷ Figures 2d & 2e show the metal fringes indicating good crystallinity which was in accordance with XRD and concentric bright circles in the SAED pattern (Figure 2f). The EDS analysis was conducted to identify, quantify, and map the distribution of elements. The EDS analysis established the distribution of Nickel (Ni), Iron (Fe), Oxygen (O), and Carbon (C), with atomic percentages of 35.41%, 41.30%, 12.62%, and 10.67%, respectively (Figure 2g). The NiFe@LDH elemental mapping displays the uniform dispersal of the elements (Figure 2h) with the weight percentages of 44.41%, 31.30%, 14.67%, and 9.62% of Ni, Fe, O, and C respectively (Figures i-1). This uniform distribution of particles offers an enhanced number of catalytic sites for synergistic electrochemical interactions involved in water splitting. Furthermore, the stoichiometric composition of the catalyst ensures efficient electronic and chemical configurations, providing ample catalytic sites essential for enhancing reaction intermediates, binding, and improving inherent activity.

The valence states and composition of the NiFe@LDH electrocatalysts were assessed using XPS analysis (Figure S1). Figures 3a-d present the deconvoluted spectra of Ni 2p, Fe 2p, C 1s, and O 1s. In the Ni 2p region of the NiFe@LDH electrocatalysts spectra, two peaks at binding energies (BE) of 856.59 eV and 874.38 eV were identified as Ni 2p_{3/2} and Ni 2p_{1/2} of Ni²⁺, respectively. Two additional peaks, identified as satellite peaks, were observed at 862.26 eV and 879.84 eV (Figure 3a).²⁸ In the Fe 2p XPS spectra, two dominant peaks at 712.7 eV and 725.9 eV were attributed to Fe 2p_{3/2} and Fe 2p_{1/2}, correspondingly,²⁹ with two satellite peaks observed at 718.3 and 731.4 eV (Figure 3b). These characteristics represent the presence of Ni and Fe in the oxidation states of Ni²⁺ and Fe³⁺.³⁰

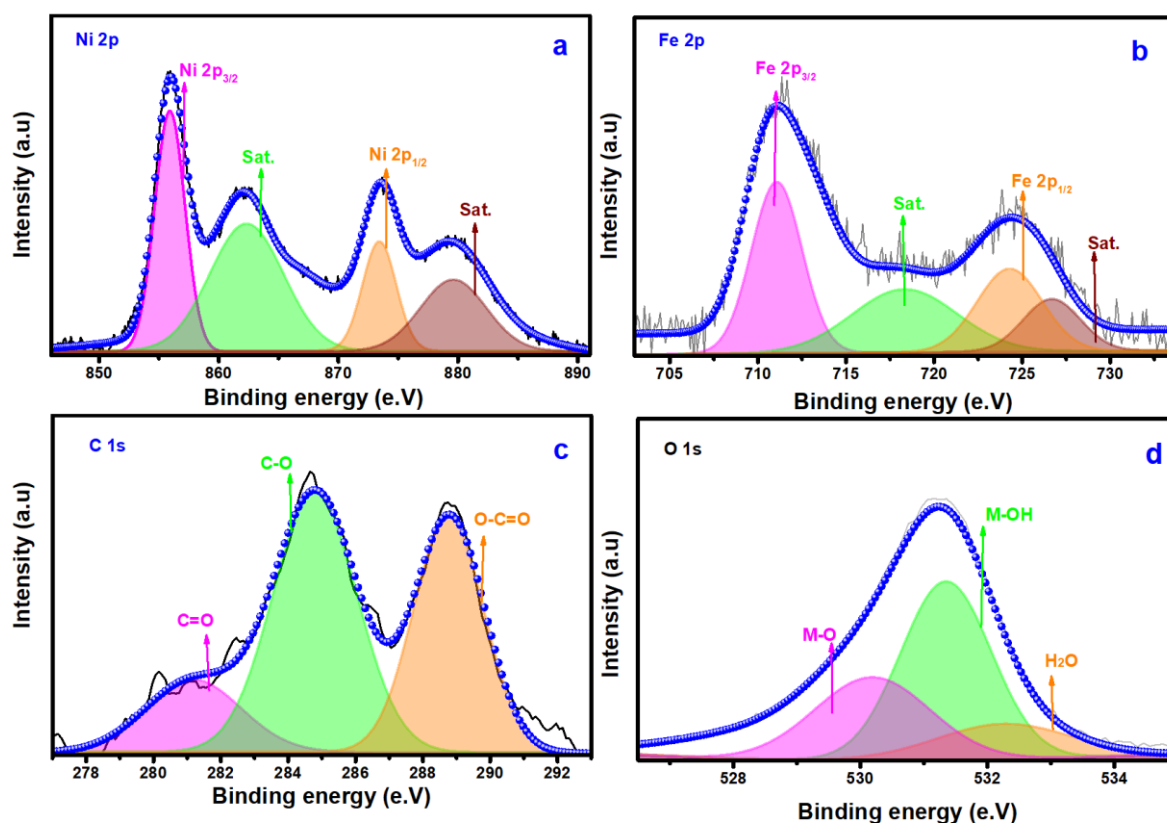


Figure 3. The XPS deconvoluted spectra of (a) Ni; (b) Fe; (c) C and (d) O.

The C 1s spectra revealed the presence of carbonate species with BE of 288.6 eV (O-C=O), 285.6 eV (C-O), and 284.5 eV (C=O). These CO₃²⁻ ions originated from sodium carbonate, which acted as a counter anion in the interlayer, contributing to the stabilization of

the LDH architecture (Figure 3c).^{27, 31} The O 1s spectra show peaks at 529.3 eV, 531.3 eV, and 532.4 eV, related to the production of M-O, M-OH, and H₂O, respectively, by the electrocatalyst (Figure 3d).^{32, 33} Through short ion diffusion pathways and dynamic oxygen liberation inside the lattice through the creation of oxygen vacancies, the metal ions Ni²⁺ and Fe³⁺ can effectively promote electron transport by enabling rapid transport of oxygen. Through short ion diffusion pathways and dynamic oxygen liberation inside the lattice through the creation of oxygen vacancies, the metal ions Ni²⁺ and Fe³⁺ can effectively promote electron transport by enabling rapid transport of O₂.

4. Electrochemical investigation

4.1 OER activity of NiFe@LDH

The electrochemical investigation of NiFe@LDH regarding its OER performance was evaluated by using a 3-electrode setup in a 1M KOH solution. The LSV graphs in Figure 4a demonstrate that the active catalyst, i.e., NiFe@LDH/NF, shows improved OER behavior with a less Tafel slope of 76 mV dec⁻¹, representing superior OER kinetics in comparison to other catalysts with Tafel values of IrO₂ (112 mV dec⁻¹), Ni(OH)₂ (158 mV dec⁻¹), Fe(OH)₂ (179 mV dec⁻¹), and NF (196 mV dec⁻¹) (Figure 4b). Additionally, besides the lower Tafel slope, NiFe@LDH displays a lower overpotential of 260 mV compared to other catalysts. IrO₂, Ni(OH)₂, Fe(OH)₂, and NF exhibit overpotentials of 320, 390, 420, and 460 mV, respectively (Figure 4c). The exceptional electrocatalytic behavior of NiFe@LDH is evidenced by its minor overpotential and Tafel slope, indicating improved kinetics. The superior catalytic behavior of NiFe@LDH in generating a larger current density is regarding the oxidation of the optimum ratio of the bimetallic with the hydroxide composite (Figure S2). Notably, NiFe@LDH exhibits a lesser overpotential than IrO₂.

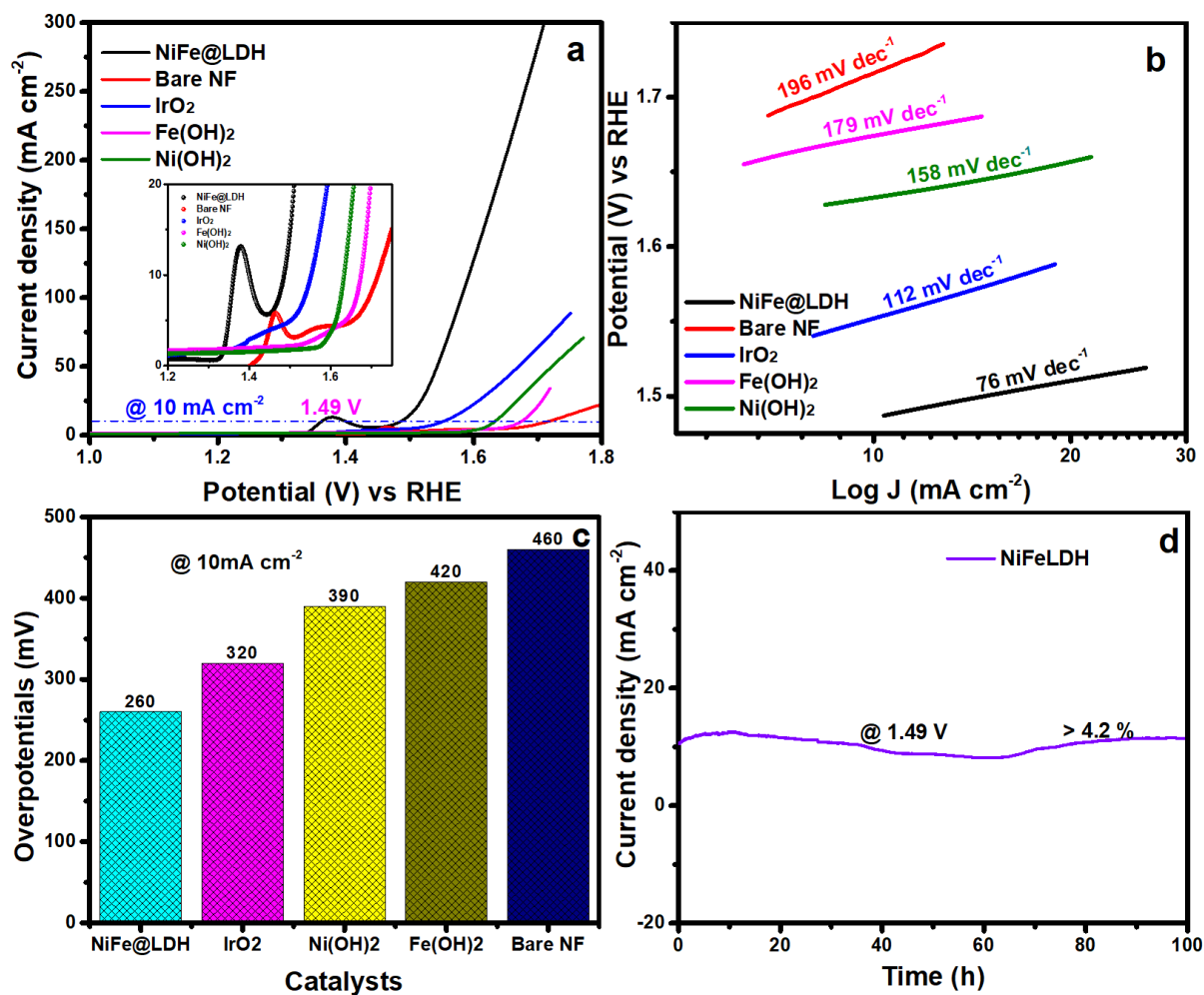


Figure 4. The polarization (OER) curves (no iR -corrected) of NiFe@LDH/NF, IrO₂/NF, Ni(OH)₂/NF, Fe(OH)₂/NF, and bare NF: (a) OER LSVs ; (b) Slopes of Tafel (c) Over potentials of different catalysts (10 mA cm⁻²); and (d) Amperometric durability test of NiFe@LDH/NF.

Table 1. Comparison of NiFe@LDH electrode electrocatalytic OER and HER activities are compared with different transition metal catalysts.

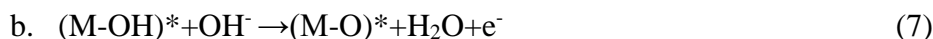
Catalyst	Synthesis method	Substrate	η (mV)	Durability (h)	Ref.
OER Activity					
NiFe LDH	Solvothermal	GC	348	--	34
NiFe LDH	Topochemical approach	GCE	300	12	35

NiFe-LDH	Hydrothermal	CFP	304	10	36
NiFe-LDH	Insitu-growth	NF	354	250	37
NiCo-LDH	Hydrothermal	CFP	346	10	36
NiFe-LDH@Ni ₃ S ₂	Wet-chemical method	NF	271	10	38
NiFe-LDH NS/DG10	Coprecipitation	GC	300	10	39
NiCoP@NiMn-LDH	Hydrothermal	NF	293	100	40
NiMn-LDH/NCO	Hydrothermal	NF	310	8	41
NiCo ₂ S ₄ @Co ₁ Ni ₄ -LDH	Hydrothermal	CC	337	40	42
NiFe-LDH/FeCoS ₂	Hydrothermal	CFC	308	12	43
Co ₄ Fe ₆ -LDH	Solvent deficient approach	GC	290	11	31
NiFe@LDH	Hydrothermal Synthesis	NF	260	100	This work
HER Activity					
NiSe-RGO-PI	Electrodeposition method	CNT film	270	12	44
Ni ₃ P PHNs	Annealing method	GC	~300	10	45
NiFe-LDH@Ni ₃ S ₂	Wet-chemical method	NF	184	10	38
NiFe-LDH	Electro deposition	NF	368	23	46
NOPHC10-900	Pyrolysis method	GC	290	20	47
FeNi LDH/V ₂ CT _x	Hydrothermal deposition	NF	274	10	28
NiCo ₂ S ₄ NW/NF	In-situ growth	NF	210	50	48
CoNiN@NiFe LDH	Electrodeposition	CC	157	50	49
NiFe- NCs	Calcination method	CFP	197	18	50
Rh/NiFeRh-LDH	Hydrothermal deposition	NF	58	-	51
NiFeRu-LDH	Hydrothermal deposition	NF	29	10	52
NiFe@LDH	Hydrothermal Synthesis	NF	138	100	This work

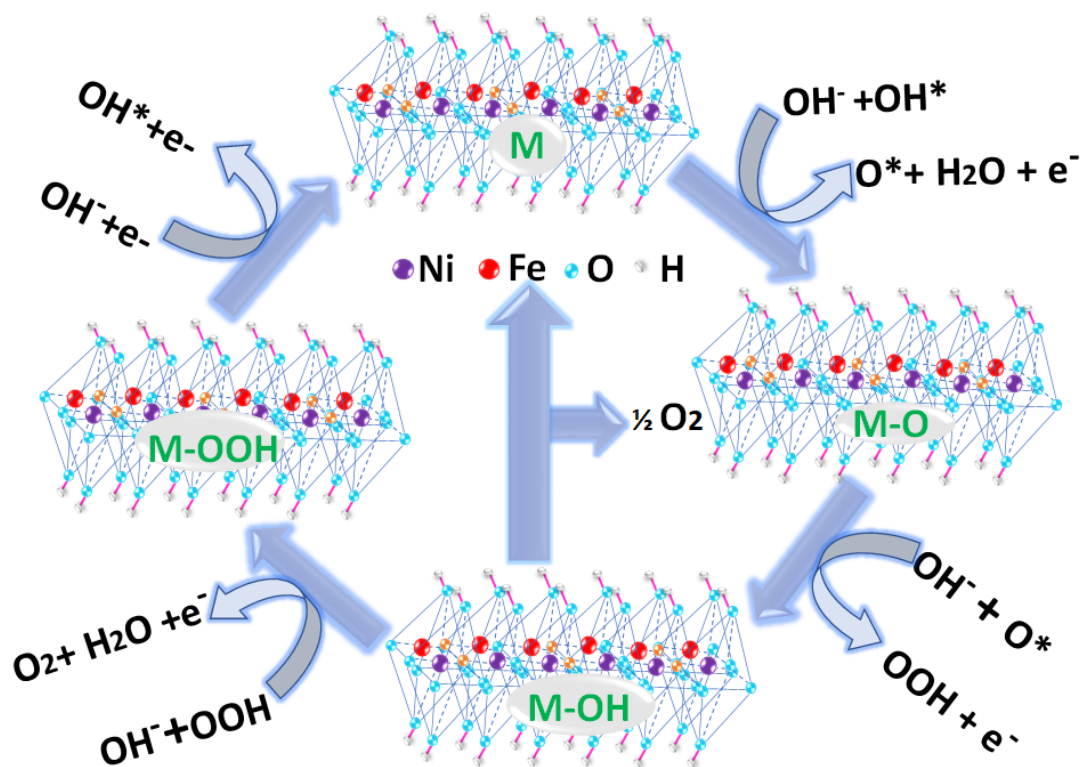
Table 1 presents the overpotential values from the literature compared to those of the NiFe@LDH/NF catalyst required to attain 10 mA cm⁻² of current density, indicating its enhanced electrocatalytic efficiency. Furthermore, to assess the electrocatalytic behavior,

Turnover Frequency (TOF) was calibrated at 1.62 V, resulting in values of 0.0848 s⁻¹, 0.0413 s⁻¹, 0.00962 s⁻¹, and 0.00712 s⁻¹ for NiFe@LDH, IrO₂, Ni(OH)₂, and Fe(OH)₂, correspondingly. This designates that NiFe@LDH/NF exhibits approximately 2.1 times higher electrocatalytic capability compared to commercialized IrO₂. The high TOF value of NiFe@LDH among the catalysts confirms its excellent OER activity. Overall, the electrochemical results demonstrate that the appropriate composition of Ni and Fe is crucial for efficient OER activity, surpassing that of IrO₂, Ni(OH)₂, and Fe(OH)₂. The enhanced catalytic behavior of NiFe@LDH can be related to effective charge transfer between the optimized ratios of Ni and Fe, OH⁻, resulting in a highly active and porous framework nanostructure that offers essential reaction kinetics. It's worth noting that while nickel content in electrocatalysts plays a vital role in improving catalytic behavior, both Ni and Fe in optimized ratios contribute to the efficient OER process.⁵³

The electrocatalyst likely experiences the subsequent OER mechanism:



The OER, which results in the production of O₂, is widely recognized to occur through a four-electron transfer mechanism. Initially, active sites facilitate the adsorption of OH⁻ ions to form M-OH*, followed by a subsequent deprotonation reaction resulting in the formation of M-O*. These intermediates further react with OH⁻ ions to produce the intermediate species M-OOH, which is a critical step in the OER procedure. Finally, the M-OOH* species undergoes deprotonation to yield O₂, followed by the renewal process of the catalytic sites. In the case of the NiFe@LDH catalyst, its enhanced efficiency is primarily attributed to the optimum ratio of bimetallic nickel and iron sites, coordinated with OH⁻ ions within the LDH composite (Scheme 2).



Scheme 2. Plausible OER mechanism of NiFe@LDH in 1M KOH.

In the OER process, Nickel ions in the form of Ni^{2+} may contribute to enhancing catalytic efficiency at the active sites, while Iron ions in the form of Fe^{3+} oxidation state could assist in boosting electrocatalytic performance at these sites. Primarily, the greater OER catalytic effect of NiFe@LDH can be accredited to efficient charge transfer (low resistance), increased electrochemical catalytic reactivity, and the presence of an abundance of catalytic sites. The durability of NiFe@LDH electrodes was assessed by performing an amperometric (i-t) curve measurement during prolonged OER activity lasting 100 hours to preserve a stable current density of 10 mA cm^{-2} . The electrodes demonstrated exceptional stability, with only a 4.2% reduction in current density observed over the testing period (Figure 4d).

4.2 HER behaviour of (NiFe@LDH)

The HER performance of NiFe@LDH/NF was evaluated by recording LSV curves within the potential range of -0.4 to 0.0 V vs. RHE. The LSV curves shown in Figure 5a demonstrate

that the NiFe@LDH electrode exhibits superior performance compared to other catalysts. Tafel analysis of NiFe@LDH revealed a Tafel slope of 83 mV dec^{-1} , which is significantly lower than that of Ni(OH)_2 (123 mV dec^{-1}), Fe(OH)_2 (149 mV dec^{-1}), and bare NF (187 mV dec^{-1}). As anticipated, the 5% Pt/C-loaded nickel foam exhibited a lower overpotential of 36 mV to achieve a current density of 10 mA cm^{-2} , with a Tafel slope of 83 mV dec^{-1} . In comparison, the NiFe@LDH catalyst demonstrated a moderate overpotential of 138 mV and a Tafel slope of 83 mV dec^{-1} for HER activity at a current density of -10 mA cm^{-2} (Figure 5b). Conversely, Ni(OH)_2 (123 mV dec^{-1}), Fe(OH)_2 (149 mV dec^{-1}), and bare NF (187 mV dec^{-1}) required overpotentials of 176, 198, and 302 mV, respectively, for effective HER activity (Figure 5c). The less overpotential value of 138 mV and the reduced Tafel plots, along with enhanced kinetics observed with the NiFe@LDH electrocatalyst, indicate its capability to efficiently produce H_2 through HER behavior.

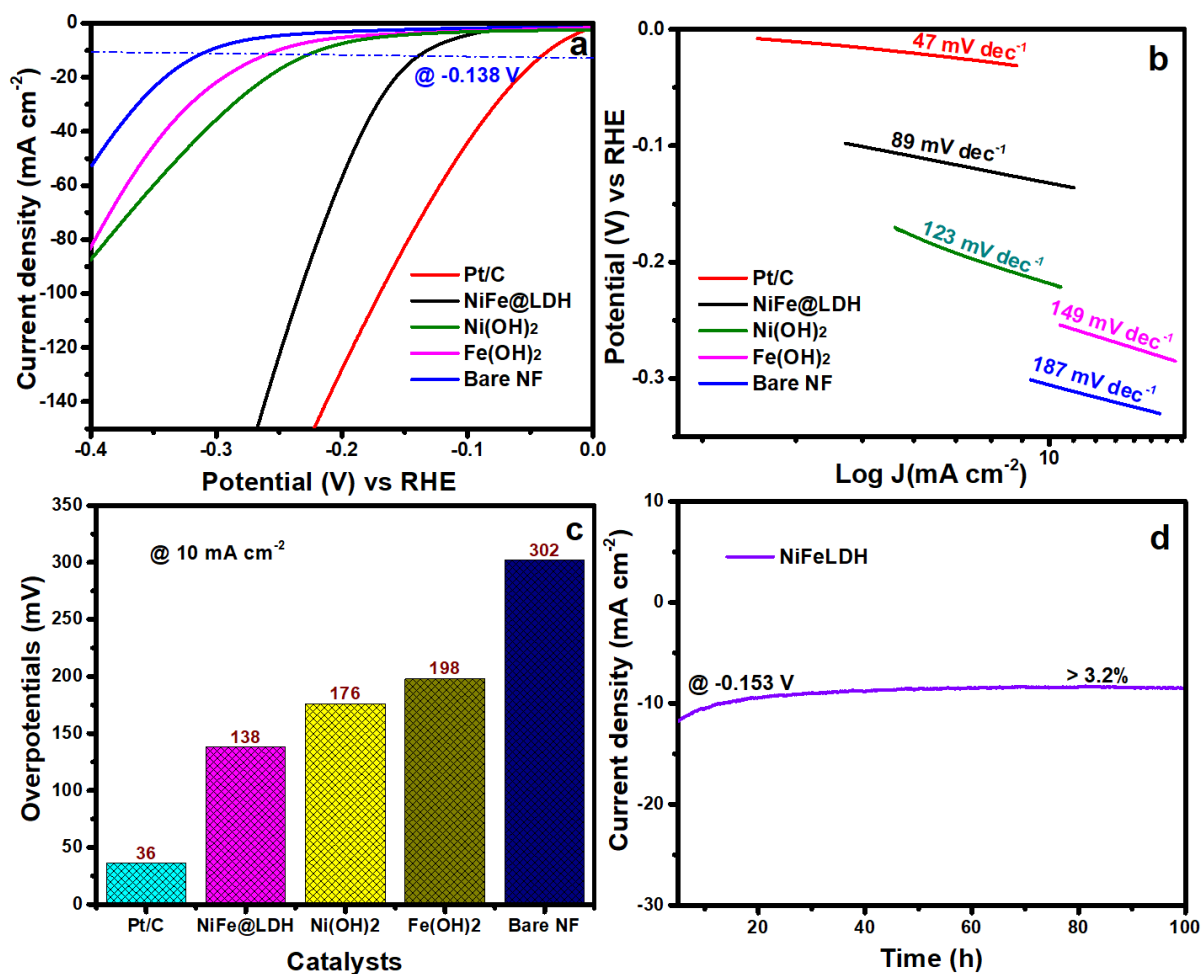


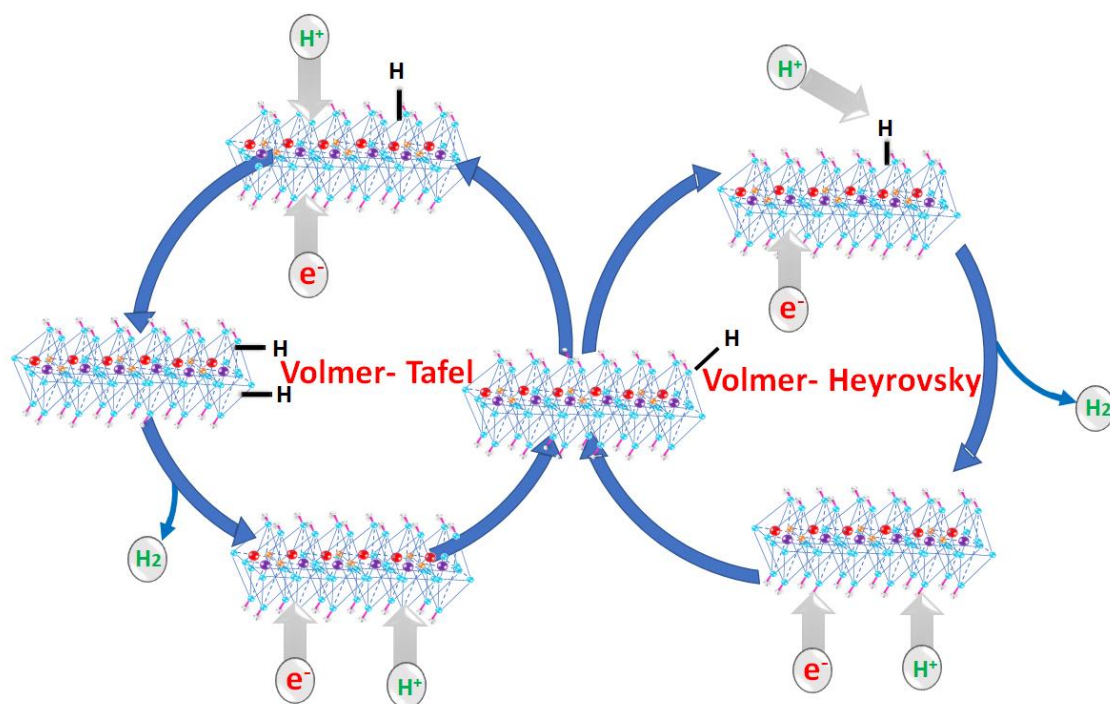
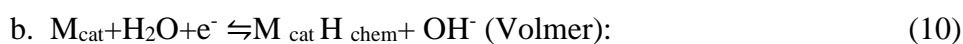
Figure 5. The polarization (HER) curves (no iR -corrected) of NiFe@LDH/NF, Pt/C/NF, Fe(OH)₂, Ni(OH)₂, and NF; (a) The LSV of the HER; (b) Tafel plot (c) Overpotentials for different electroactive catalysts (10 mA cm^{-2}); and (d) Chronoamperometric durability trial of NiFe@LDH/NF.

Tafel slopes were examined to assess the catalyst reaction kinetics for HER activity, as depicted in Figure 5b. The Tafel plot of NiFe@LDH yielded a value of 83 mV dec^{-1} , which was notably less compared to that of Ni(OH)₂ (123 mV dec^{-1}), Fe(OH)₂ (149 mV dec^{-1}), and bare NF (187 mV dec^{-1}). As anticipated, the 5% Pt/C loaded Ni foam exhibited a lower overpotential of 36 mV to attain a current density of 10 mA cm^{-2} , with a Tafel value of 69 mV dec^{-1} , contrasting with the NiFe@LDH catalyst. However, it is noteworthy that the HER behavior of the bare NF greatly increased upon coating with NiFe@LDH. The Turnover Frequency (TOF) value at -0.2 V was utilized to evaluate the crucial electrocatalytic efficacy

of NiFe@LDH catalyst compared to the standard Pt/C catalyst and other catalysts such as Ni(OH)₂ and Fe(OH)₂. Pt/C exhibited a TOF value of 0.1321 s⁻¹, while NiFe@LDH displayed a TOF value of 0.0891 s⁻¹, Ni(OH)₂ showed 0.0513 s⁻¹, and Fe(OH)₂ showed 0.0308 s⁻¹, respectively. This remarkable TOF value indicates the potential of NiFe@LDH for efficient HER activity compared to other catalysts, Ni(OH)₂, and Fe(OH)₂. The HER process was determined to follow the Volmer-Heyrovsky mechanism, as indicated by its lower Tafel slopes. Evaluation of current-time (i-t) plots for the NiFe@LDH electrode indicated excellent stability over 100 hours (at 10 mA cm⁻²) with a negligible reduction of < 3.2% in current density (Figure 5d).

Compared to the commonly tested transition metal-based electrocatalysts, NiFe@LDH demonstrated exceptional HER behavior, as evidenced by its less overpotential and reduced Tafel slope values. Table 1 provides a comparison of overpotential values reported for various transition metal electrocatalysts, further confirming the superior HER activity of NiFe@LDH. The effective HER performance of NiFe@LDH is attributed to its irregular spherical microstructures and hydroxide-bridged framework, which facilitate efficient active sites and an effective pathway for charge diffusion. The electrochemical data strongly indicate the effectiveness of NiFe@LDH in HER activity. In the HER, the disintegration of water is the step that determines the rate, and NiFe@LDH shows a strong tendency for water disintegration, resulting in the production of numerous H₂ atoms. These H₂ atoms migrate to the electrocatalytic sites of NiFe@LDH where they form M-H bonds, which subsequently combine with water molecules to generate H₂ gas. This behavior aligns with the observations from the Tafel slope analysis. The formation of (M-OH)_x species reduces the availability of local surface OH-species, thereby promoting the desorption of hydroxide ions (OH⁻) from the surface. The presence of low oxidation state nickel species on the surface of NiFe@LDH greatly enhances its capability for water disintegration and HER kinetics. The increased activity

of the HER electrocatalyst suggests an augmentation in the number of active sites. Consequently, bimetallic Ni-Fe encapsulated with layered hydroxide nanostructured electrocatalysts emerges as a capable candidate for electrochemical energy conversion. In the HER process, the Tafel-Volmer-Heyrovsky pathway is employed to generate H₂ from transition metals and metal chalcogenides (Scheme 3). The Volmer-Heyrovsky equation, which facilitates the formation of H₂ at very low potentials (V) in 1M KOH, may explain the enhanced HER activity observed in NiFe@LDH.



Scheme 3. Plausible HER mechanism of NiFe@LDH in an alkaline medium (1M KOH).

To measure the electrochemically active surface area (ECSA = C_{dl}/C_s) and roughness factor (Rf = ECSA/GSA) of the NiFe@LDH, and bare NF electrodes were assessed. Here, GSA = 0.25 cm² represents the geometric surface area, C_{dl} denotes the double-layer capacitance

(in mF cm^{-2}), and C_s represents the specific capacitance. The C_s values for NiFe@LDHs electrocatalysts in an alkaline medium are assumed to be 0.040 mF cm^{-2} . The C_{dl} values of NiFe@LDH (0.00269 mF), as well as bare NF shows (0.00098 mF), were determined through CVs conducted at various scan rates ($10, 20, 30, 40,$ and 50 mV s^{-1}) within the potential range of 0.9 to 1.06 V vs. RHE (Figure S3). The measured ECSA value of NiFe@LDH was determined to be 67.25 cm^2 , while for bare NF was calculated to be 24.65 cm^2 indicating the occurrence of abundant catalytic sites on the superficial of the active catalyst. Additionally, the roughness factor of NiFe@LDH was calibrated as $269 R_f$, whereas NF shows $99 R_f$. The ECSA (67.25 cm^2), C_{dl} (0.00269 mF), and R_f ($269 R_f$) values of NiFe@LDH/NF demonstrate superior catalytic behavior, indicating a great communication of the catalyst with the electrolyte, leading to improved HER and OER action.

The charge transfer conductance of NiFe@LDH during the OER and HER were examined using EIS measurements, as depicted in Figure 6. The Randles equivalent circuit employed to model the obtained EIS curves is depicted in Figure 6, where R_s represents the electrolyte resistivity, while R_{ct} denotes the charge transfer resistance at the double-layer capacitance (C_{dl}). The R_{ct} values for NiFe@LDH were determined to be 1.29Ω , which were notably lower compared to those bare NF 12.82Ω catalysts. As a redox-capable catalyst, NiFe@LDH exhibits enhanced electronic properties and a relatively mild resistance (R_{ct} : 1.29Ω), facilitating efficient charge transfer kinetics. This capability allows NiFe@LDH to cycle between different oxidation states, thereby facilitating electron transmission among the catalyst and reactants effectively.

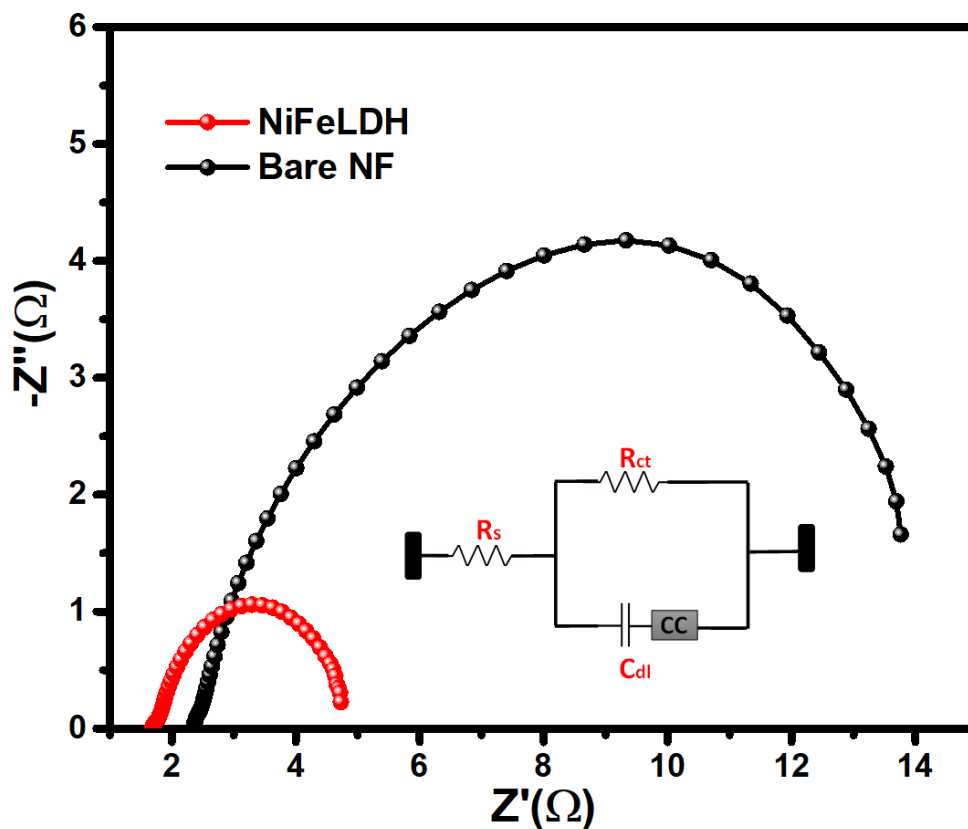


Figure 6. Electrochemical Impedance spectra of NiFe@LDH and Bare NF (inset-Randles equivalent circuit).

5. Total water disintegration of NiFe@LDH

The bifunctional characteristics of the NiFe@LDH/NF catalyst were assessed by employing it as both an anode and a cathode electrode concurrently [NiFe@LDH/NF//NiFe@LDH/NF]. The LSV plot of NiFe@LDH/NF//NiFe@LDH/NF illustrates the catalyst's superior efficiency in total water disintegration compared to the bare NF//NF system (Figure 7a). To attain a 10 mA cm^{-2} current density with rapid H_2 and O_2 productions at the cathode and anode, respectively, the NiFe@LDH catalysts need a less overpotential of 1.57 V (NiFe@LDH//NiFe@LDH/NF), which is 0.25 V lower than the NF//NF system requiring 1.82 V of bias potential for overall water disintegration. Notably, this value is lower than that of the widely used bifunctional catalysts as indicated in Table 2. As expected, the ideal bifunctional catalyst $\text{IrO}_2/\text{NF}//\text{Pt}/\text{C}/\text{NF}$ displays the water-

disintegration behavior at a very minute overpotential of 1.51 V. Additionally, stability tests of the NiFe@LDH/NF//NiFe@LDH/NF bifunctional system demonstrated excellent performance with only a 4.6 % reduction in current density after 150 hours of prolonged water disintegration at 10 mA cm⁻² (Figure 7b & 7c). The synchronous result brought about by electron dissemination from the Fe-Ni to the hydroxide complex enabled the catalytic process.⁵⁴

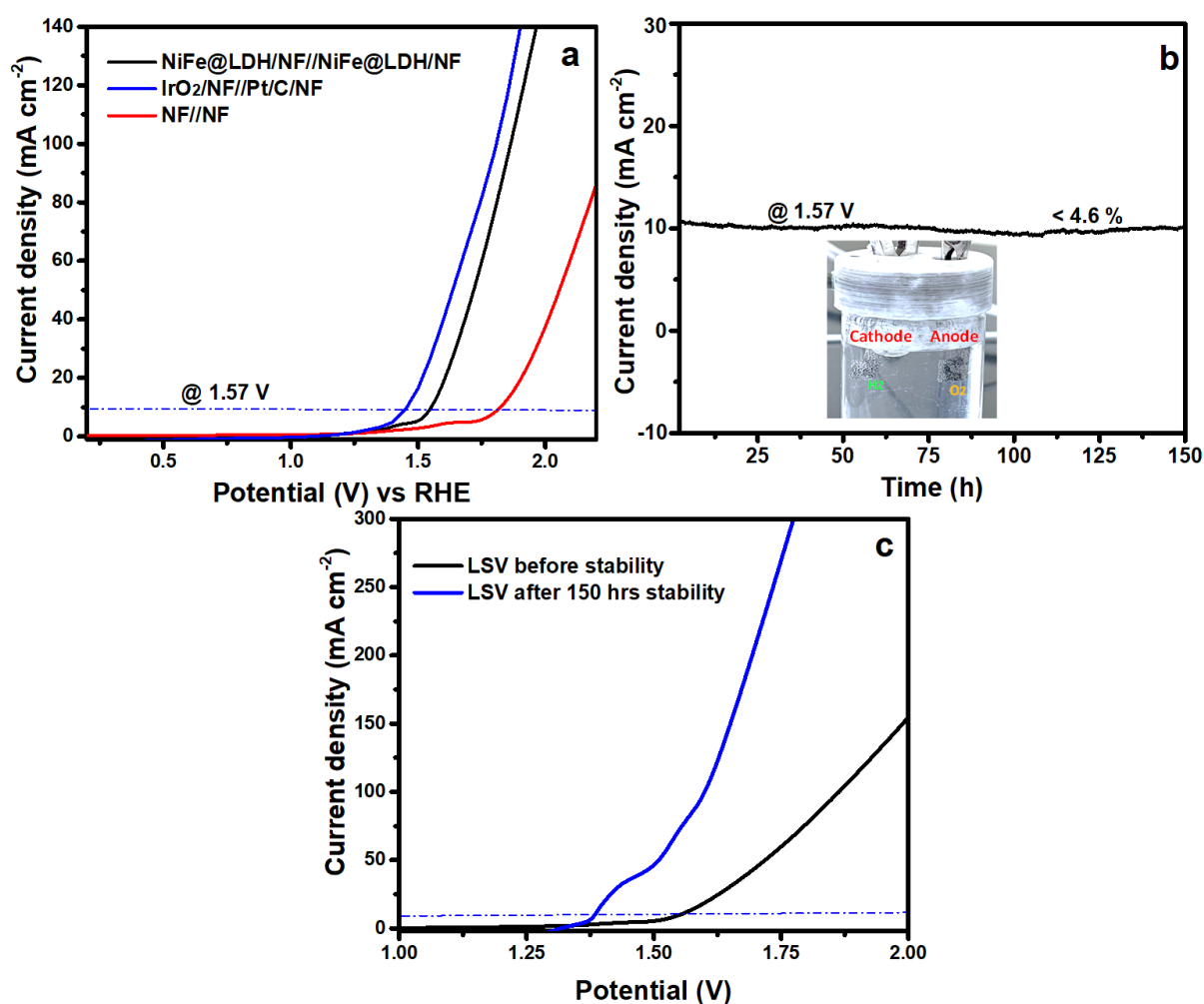


Figure 7. (a) Full cell LSVs of NiFe@LDH/NF, IrO₂/Pt/C/NF, and Nascent NF (b) Full Cell stability test at 1.61 V vs RHE (@10 mA cm⁻²) and (c) LSV curves pre and post durability.

Table 2. NiFe@LDH electrode electrocatalytic full-cell activities are compared with different transition metal catalysts.

Catalyst	Substrate	Cell potential (V)	Ref.
CoFe-LDH	NF	1.69	55
CoFe-LDH@g-C ₃ N ₄	NF	1.82	56
NiCo ₂ S ₄ @NiFe-LDH	RDE	1.60	57
NiFe-LDH-Co ₃ O ₄	NF	1.64	58
NiSe@CoFe LDH	NF	1.69	59
NiFe LDH	NF	1.70	60
Fe ₃ O ₄ /NiFe LDH/Fe ₃ O ₄	NF	1.63	61
Co ₉ S ₈ /Ni ₃ S ₂ @NiFe-LDH	NF	1.62	62
Co ₃ S ₄ @NiCo-LDH	NF	1.59	63
NiFe@LDH	NF	1.57	This work

6. Solar-to-hydrogen (STH) of NiFe@LDH

The NiFe@LDH/NF//NiFe@LDH/NF system was coupled with a commercial solar panel to demonstrate its renewable energy potential. A multimeter was utilized to regulate and measure the voltage supplied by the solar panels to the NiFe@LDH/NF//NiFe@LDH/NF water-splitting system containing 1M KOH. The setup was positioned directly under sunlight exposure (Fig 8a). With an applied potential of 1.62 V via solar panels, continuous production of O₂ and H₂ gas was observed. Based on the generated current, the amount of H₂ and O₂ produced was calibrated to be 6.15 and 2.89 mmol h⁻¹cm⁻², respectively, maintaining the expected molar ratio (Figure 8b). Interestingly, these results underscore the bifunctional capability of the catalyst along with its renewable applicability for low-cost hydrogen production.

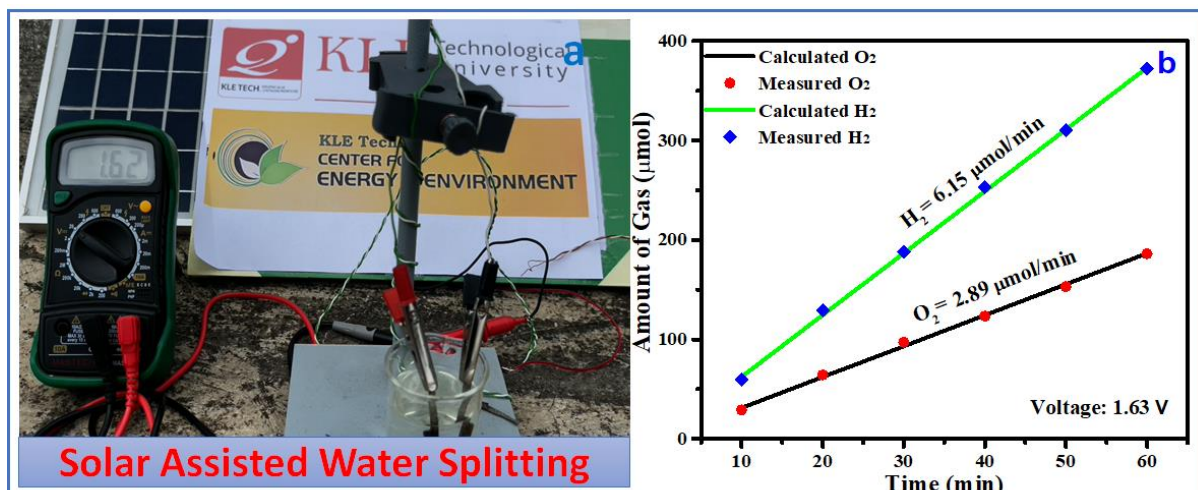


Figure 8. (a) Photograph of solar-water splitting (b) Plot Faradic efficiency.

7. Conclusions

A hydrothermal approach has been developed to synthesize a NiFe LDH-based bifunctional electrocatalyst for alkaline water disintegration. This innovative approach allows for precise adjustment of the stoichiometry to optimize the ratio of Fe and Ni bound to the OH moiety of LDH. Among the various catalysts synthesized, NiFe@LDH displays improved catalytic behavior compared to other hydroxide forms i.e. Ni(OH)₂, Fe(OH)₂. The NiFe@LDH/NF electrodes fabricated using this catalyst demonstrate a consistent 10 mA cm⁻² current density at a remarkably low potential of 260 mV with a Tafel value of 76 mV dec⁻¹ for the OER, and an overpotential of 138 mV with a Tafel value of 83 mV dec⁻¹ for the HER. The overpotential and Tafel plot values of NiFe@LDH are found to be more favorable and analogous to the standard catalysts IrO₂ and Pt/C. Furthermore, NiFe@LDH exhibits excellent stability over 100 hours, with only a 4.2% reduction in current density during OER and a 3.2% reduction during HER under O₂ and H₂ production conditions, respectively. When employed in a bifunctional setup, the NiFe@LDH/NF//NiFe@LDH/NF electrode facilitates rapid H₂ and O₂ production at 10 mA cm⁻² under a cell potential of 1.57 V. Notably, the bifunctional NiFe@LDH catalyst maintains excellent durability over 150 hours of operation, with only a 4.6% reduction in current. The renewal of the system was established by integrating the

NiFe@LDH/NF//NiFe@LDH/NF setup with solar panels, which enabled the production of H₂ and O₂ at an overpotential of 1.62 V. In conclusion, the catalyst developed in the current work represents a greater class of LDH with highly effective tunable, stable properties with promising applications in future hydrogen production using renewable energy sources.

Supporting Information

Preparation of Ni(OH)₂ and Fe (OH)₂, Survey Spectrum of XPS, Cyclic voltammograms of NiFe@LDH, Ni(OH)₂, and Fe(OH)₂, ECSA of NiFe@LDH & Bare NF.

References:

1. Zhang, W.; Lai, W.; Cao, R., Energy-Related Small Molecule Activation Reactions: Oxygen Reduction and Hydrogen and Oxygen Evolution Reactions Catalyzed by Porphyrin- and Corrole-Based Systems. *Chem. Rev.* 2017, 117 (4), 3717-3797.
2. Zhang, J.; Wang, T.; Pohl, D.; Rellinghaus, B.; Dong, R.; Liu, S.; Zhuang, X.; Feng, X., Interface Engineering of MoS₂ /Ni₃ S₂ Heterostructures for Highly Enhanced Electrochemical Overall-Water-Splitting Activity. *Angew. Chem. Int. Ed.* 2016, 55 (23), 6702-7.
3. Reddy, N. R.; Bharagav, U.; Shankar, M. V.; Reddy, P. M.; Reddy, K. R.; Shetti, N. P.; Alonso-Marroquin, F.; Kumari, M. M.; Aminabhavi, T. M.; Joo, S. W., Photocatalytic hydrogen production by ternary heterojunction composites of silver nanoparticles doped FCNT-TiO₂. *ISO4 Standard J. Environ. Manage.* 2021, 286, 112130.
4. Esposito, D. V.; Hunt, S. T.; Stottlemyer, A. L.; Dobson, K. D.; McCandless, B. E.; Birkmire, R. W.; Chen, J. G., Low-Cost Hydrogen-Evolution Catalysts Based on Monolayer Platinum on Tungsten Monocarbide Substrates. *Angew. Chem. Int. Ed.* 2010, 49 (51), 9859-9862.

5. Lee, Y.; Suntivich, J.; May, K. J.; Perry, E. E.; Shao-Horn, Y., Synthesis and Activities of Rutile IrO₂ and RuO₂ Nanoparticles for Oxygen Evolution in Acid and Alkaline Solutions. *J. Phys. Chem. Lett.* 2012, 3 (3), 399-404.
6. Singla, S.; Shetti, N. P.; Basu, S.; Mondal, K.; Aminabhavi, T. M., Hydrogen production technologies - Membrane based separation, storage and challenges. *J. Environ. Manage.* 2022, 302, 113963.
7. Sreenivasulu, M.; Shetti, R. S.; Mathi, S.; Maiyalagan, T.; Shetti, N. P., Ni-tethered MoS₂: In-situ fast reduction synthesis as an ultra-durable and highly active electrocatalyst for water splitting and urea oxidation. *Mater. Today Sustain.* 2024, 26, 100782.
8. Liu, T.; Yan, X.; Xi, P.; Chen, J.; Qin, D.; Shan, D.; Devaramani, S.; Lu, X., Nickel–Cobalt phosphide nanowires supported on Ni foam as a highly efficient catalyst for electrochemical hydrogen evolution reaction. *Int. J. Hydrogen Energy.* 2017, 42 (20), 14124-14132.
9. Geng, X.; Wu, W.; Li, N.; Sun, W.; Armstrong, J.; Al-hilo, A.; Brozak, M.; Cui, J.; Chen, T.-p., Three-Dimensional Structures of MoS₂ Nanosheets with Ultrahigh Hydrogen Evolution Reaction in Water Reduction. *Adv. Funct. Mater.* 2014, 24 (39), 6123-6129.
10. Kalanur, S. S.; Seo, H., An experimental and density functional theory studies of Nb-doped BiVO₄ photoanodes for enhanced solar water splitting. *J. Catal.* 2022, 410, 144-155.
11. Li, H.; Wang, X.; Wang, T.; Xiao, F., A facile, green and time-saving method to prepare partially crystalline NiFe layered double hydroxide nanosheets on nickel foam for superior OER catalysis. *J. Alloys Compd.* 2020, 844, 156224.
12. Yin, P.; Wu, G.; Wang, X.; Liu, S.; Zhou, F.; Dai, L.; Wang, X.; Yang, B.; Yu, Z.-Q., NiCo-LDH nanosheets strongly coupled with GO-CNTs as a hybrid electrocatalyst for oxygen evolution reaction. *Nano Res.* 2021, 14 (12), 4783-4788.

13. Kalanur, S. S.; Noh, Y.-G.; Seo, H., Engineering band edge properties of WO₃ with respect to photoelectrochemical water splitting potentials via a generalized doping protocol of first-row transition metal ions. *Appl. Surf. Sci.* 2020, 509, 145253.
14. Li, P.; Duan, X.; Kuang, Y.; Li, Y.; Zhang, G.; Liu, W.; Sun, X., Tuning Electronic Structure of NiFe Layered Double Hydroxides with Vanadium Doping toward High Efficient Electrocatalytic Water Oxidation. *Adv. Energy Mater.* 2018, 8 (15), 1703341.
15. Yang, Y.; Dang, L.; Shearer, M. J.; Sheng, H.; Li, W.; Chen, J.; Xiao, P.; Zhang, Y.; Hamers, R. J.; Jin, S., Highly Active Trimetallic NiFeCr Layered Double Hydroxide Electrocatalysts for Oxygen Evolution Reaction. *Adv. Energy Mater.* 2018, 8 (15), 1703189.
16. Mathi, S.; Ashok, V.; Alodhayb, A. N.; Pandiaraj, S.; Shetti, N. P., Cobalt decorated S-doped carbon electrocatalyst assembly for enhanced oxygen evolution reaction. *Mater. Today Sustain.* 2024, 26, 100717.
17. Liu, Q.; Huang, J.; Yang, D.; Feng, Y.; Li, G.; Zhang, X.; Zhang, Y.; Xu, G.; Feng, L., Formation of porous NiCoV-LTH nanosheet arrays by in situ etching of nickel foam for the hydrogen evolution reaction at large current density. *Dalton Trans.* 2021, 50 (1), 72-75.
18. Banerjee, D.; Kushwaha, N.; Shetti, N. P.; Aminabhavi, T. M.; Ahmad, E., Green hydrogen production via photo-reforming of bio-renewable resources. *Renew. Sustain. Energy Rev.* 2022, 167, 112827.
19. Sreenivasulu, M.; Shetti, R. S.; Mathi, S.; Shetti, N. P., Highly efficient Cu-Fe containing prussian blue analogs (PBAs) for excellent electrocatalytic activity towards overall water splitting. *Electrochim. Acta.* 2024, 492, 144340.

20. Wang, Y.; Yan, D.; El Hankari, S.; Zou, Y.; Wang, S., Recent Progress on Layered Double Hydroxides and Their Derivatives for Electrocatalytic Water Splitting. *Adv. Sci.* 2018, 5 (8), 1800064.
21. Liang, J.; Xiang, C.; Zou, Y.; Hu, X.; Chu, H.; Qiu, S.; Xu, F.; Sun, L., Spacing graphene and Ni-Co layered double hydroxides with polypyrrole for high-performance supercapacitors. *J. Mater. Sci. Technol.* 2020, 55, 190-197.
22. Sreenivasulu, M.; Malode, S. J.; Alqarni, S. A.; Shetti, N. P., Graphitic carbon nitride (g-C₃N₄)-based electrochemical sensors for the determination of antiviral drug acyclovir. *Mater. Chem. Phys.* 2024, 312, 128650.
23. Wang, F.-G.; Yan, W.-M.; Yan, M.; Song, M.-M., Outcomes of transanal tube placement in anterior resection: A meta-analysis and systematic review. *Int. J. Surg.* 2018, 59, 1-10.
24. Yang, C.; Wöll, C., IR spectroscopy applied to metal oxide surfaces: adsorbate vibrations and beyond. *Adv. Phys. X* 2017, 2 (2), 373-408.
25. Zhai, L.-F.; Mao, H.-Z.; Sun, M., Fabrication of Ni-Fe LDH/GF anode for enhanced Fe(III) regeneration in fuel cell-assisted chelated-iron dehydrosulfurization process. *J. Chem. Technol. Biotechnol.* 2018, 93 (1), 80-87.
26. Wang, H.; Wang, C.; Zhang, W.; Yao, S., A nano-spherical structure Ni₃S₂/Ni(OH)₂ electrocatalyst prepared by one-step fast electrodeposition for efficient and durable water splitting. *Int. J. Hydrogen Energy.* 2022, 47 (33), 14916-14929.
27. Liu, P. F.; Yang, S.; Zhang, B.; Yang, H. G., Defect-Rich Ultrathin Cobalt–Iron Layered Double Hydroxide for Electrochemical Overall Water Splitting. *ACS Appl. Mater. Interfaces.* 2016, 8 (50), 34474-34481.
28. Yang, L.; Yang, T.; Chen, Y.; Zheng, Y.; Wang, E.; Du, Z.; Chou, K.-C.; Hou, X. FeNi LDH/V₂CT_x/NF as Self-Supported Bifunctional Electrocatalyst for Highly Effective Overall Water Splitting. *Nanomater.* 2022, 12(15), 2640.

29. Yu, L.; Zhou, H.; Sun, J.; Qin, F.; Yu, F.; Bao, J.; Yu, Y.; Chen, S.; Ren, Z., Cu nanowires shelled with NiFe layered double hydroxide nanosheets as bifunctional electrocatalysts for overall water splitting. *Energy Environ. Sci.* 2017, *10* (8), 1820-1827.
30. Hou, Y.; Lohe, M. R.; Zhang, J.; Liu, S.; Zhuang, X.; Feng, X., Vertically oriented cobalt selenide/NiFe layered-double-hydroxide nanosheets supported on exfoliated graphene foil: an efficient 3D electrode for overall water splitting. *Energy Environ. Sci.* 2016, *9* (2), 478-483.
31. Vishnu, B.; Sriram, S.; Jayabharathi, J., A green synthetic approach: crystalline–amorphous interface CoFe-LDH as a sustainable electrocatalyst for water oxidation with low cell voltage and evaluation of its sustainability standards. *Sustain. Energy Fuels.* 2023, *7* (18), 4638-4653.
32. Jadhav, H. S.; Roy, A.; Desalegan, B. Z.; Seo, J. G., An advanced and highly efficient Ce assisted NiFe-LDH electrocatalyst for overall water splitting. *Sustain. Energy Fuels.* 2020, *4* (1), 312-323.
33. Bo, X.; Li, Y.; Hocking, R. K.; Zhao, C., NiFeCr Hydroxide Holey Nanosheet as Advanced Electrocatalyst for Water Oxidation. *ACS Appl. Mater. Interfaces.* 2017, *9* (47), 41239-41245.
34. Hao, C.; Wu, Y.; An, Y.; Cui, B.; Lin, J.; Li, X.; Wang, D.; Jiang, M.; Cheng, Z.; Hu, S., Interface-coupling of CoFe-LDH on MXene as high-performance oxygen evolution catalyst. *Mater. Today Energy.* 2019, *12*, 453-462.
35. Song, F.; Hu, X., Exfoliation of layered double hydroxides for enhanced oxygen evolution catalysis. *Nat. Commun.* 2014, *5* (1), 4477.
36. Zhang, M.; Liu, Y.; Liu, B.; Chen, Z.; Xu, H.; Yan, K., Trimetallic NiCoFe-Layered Double Hydroxides Nanosheets Efficient for Oxygen Evolution and Highly Selective

- Oxidation of Biomass-Derived 5-Hydroxymethylfurfural. *ACS Catal.* 2020, 10 (9), 5179-5189.
37. Wu, S.-W.; Liu, S.-Q.; Tan, X.-H.; Zhang, W.-Y.; Cadien, K.; Li, Z., Ni₃S₂-embedded NiFe LDH porous nanosheets with abundant heterointerfaces for high-current water electrolysis. *Chem. Eng. J.* 2022, 442, 136105.
38. Liang, X.; Li, Y.; Fan, H.; Deng, S.; Zhao, X.; Chen, M.; Pan, G.; Xiong, Q.; Xia, X., Bifunctional NiFe layered double hydroxide@Ni₃S₂ heterostructure as efficient electrocatalyst for overall water splitting. *Nanotechnol.* 2019, 30 (48), 484001.
39. Jia, Y.; Zhang, L.; Gao, G.; Chen, H.; Wang, B.; Zhou, J.; Soo, M. T.; Hong, M.; Yan, X.; Qian, G.; Zou, J.; Du, A.; Yao, X., A Heterostructure Coupling of Exfoliated Ni-Fe Hydroxide Nanosheet and Defective Graphene as a Bifunctional Electrocatalyst for Overall Water Splitting. *Adv. Mater.* 2017, 29 (17) 1700017.
40. Wang, P.; Qi, J.; Chen, X.; Li, C.; Li, W.; Wang, T.; Liang, C., Three-Dimensional Heterostructured NiCoP@NiMn-Layered Double Hydroxide Arrays Supported on Ni Foam as a Bifunctional Electrocatalyst for Overall Water Splitting. *ACS Appl. Mater. Interfaces.* 2020, 12 (4), 4385-4395.
41. Yang, L.; Chen, L.; Yang, D.; Yu, X.; Xue, H.; Feng, L., NiMn layered double hydroxide nanosheets/NiCo₂O₄ nanowires with surface rich high valence state metal oxide as an efficient electrocatalyst for oxygen evolution reaction. *J. Power Sources.* 2018, 392, 23-32.
42. Yuan, F.; Wei, J.; Qin, G.; Ni, Y., Carbon cloth supported hierarchical core-shell NiCo₂S₄@CoNi-LDH nanoarrays as catalysts for efficient oxygen evolution reaction in alkaline solution. *J. Alloys Compd.* 2020, 830, 154658.
43. Zhang, Z.; Zhou, J.; Wei, H.; Dai, Y.; Li, S.; Shi, H.; Xu, G., Construction of hierarchical NiFe-LDH/FeCoS₂/CFC composites as efficient bifunctional

- electrocatalysts for hydrogen and oxygen evolution reaction. *J. Mater. Sci.* 2020, 55, 16625+.
44. Wang, T.; Li, X.; Jiang, Y.; Zhou, Y.; Jia, L.; Wang, C., Reduced graphene oxide-polyimide/carbon nanotube film decorated with NiSe nanoparticles for electrocatalytic hydrogen evolution reactions. *Electrochim. Acta.* 2017, 243, 291-298.
45. Jin, L.; Xia, H.; Huang, Z.; Lv, C.; Wang, J.; Humphrey, M. G.; Zhang, C., Phase separation synthesis of trinickel monophosphide porous hollow nanospheres for efficient hydrogen evolution. *J. Mater. Chem. A.* 2016, 4 (28), 10925-10932.
46. Yang, Y.; Xie, Y.; Yu, Z.; Guo, S.; Yuan, M.; Yao, H.; Liang, Z.; Lu, Y. R.; Chan, T.-S.; Li, C.; Dong, H.; Ma, S., Self-supported NiFe-LDH@CoS_x nanosheet arrays grown on nickel foam as efficient bifunctional electrocatalysts for overall water splitting. *Chem. Eng. J.* 2021, 419, 129512.
47. Huang, S.; Meng, Y.; Cao, Y.; He, S.; Li, X.; Tong, S.; Wu, M., N-, O- and P-doped hollow carbons: Metal-free bifunctional electrocatalysts for hydrogen evolution and oxygen reduction reactions. *Appl. Catal. B: Environ.* 2019, 248, 239-248.
48. Sivanantham, A.; Ganesan, P.; Shanmugam, S., Bifunctional Electrocatalysts: Hierarchical NiCo₂S₄ Nanowire Arrays Supported on Ni Foam: An Efficient and Durable Bifunctional Electrocatalyst for Oxygen and Hydrogen Evolution Reactions. *Adv. Funct. Mater.* 2016, 26 (26), 4660-4660.
49. Wang, J.; Lv, G.; Wang, C., A highly efficient and robust hybrid structure of CoNiN@NiFe LDH for overall water splitting by accelerating hydrogen evolution kinetics on NiFe LDH. *Appl. Surf. Sci.* 2021, 570, 151182.
50. Kumar, A.; Bhattacharyya, S., Porous NiFe-Oxide Nanocubes as Bifunctional Electrocatalysts for Efficient Water-Splitting. *ACS Appl. Mater. Interfaces.* 2017, 9 (48), 41906-41915.

51. Zhang, B.; Zhu, C.; Wu, Z.; Stavitski, E.; Lui, Y. H.; Kim, T.-H.; Liu, H.; Huang, L.; Luan, X.; Zhou, L.; Jiang, K.; Huang, W.; Hu, S.; Wang, H.; Francisco, J. S., Integrating Rh Species with NiFe-Layered Double Hydroxide for Overall Water Splitting. *Nano Lett.* 2020, 20 (1), 136-144.
52. Chen, G.; Wang, T.; Zhang, J.; Liu, P.; Sun, H.; Zhuang, X.; Chen, M.; Feng, X., Accelerated Hydrogen Evolution Kinetics on NiFe-Layered Double Hydroxide Electrocatalysts by Tailoring Water Dissociation Active Sites. *Adv. Mater.* 2018, 30 (10), 1706279.
53. Shetti, R. S.; Sreenivasulu, M.; Mathi, S.; Shetti, N. P., Highly Efficient and Low-Cost CuFeCN as an OER and HER Electrocatalyst for Sustainable Hydrogen Production. *Energy Fuels.* 2023, 37 (21), 16588-16598.
54. Yin, X.; Yang, L.; Gao, Q., Core-shell nanostructured electrocatalysts for water splitting. *Nanoscale.* 2020, 12 (30), 15944-15969.
55. Han, L.; Dong, C.; Zhang, C.; Gao, Y.; Zhang, J.; Gao, H.; Wang, Y.; Zhang, Z., Dealloying-directed synthesis of efficient mesoporous CoFe-based catalysts towards the oxygen evolution reaction and overall water splitting. *Nanoscale.* 2017, 9 (42), 16467-16475.
56. Arif, M.; Yasin, G.; Shakeel, M.; Mushtaq, M. A.; Ye, W.; Fang, X.; Ji, S.; Yan, D., Hierarchical CoFe-layered double hydroxide and g-C₃N₄ heterostructures with enhanced bifunctional photo/electrocatalytic activity towards overall water splitting. *Mater. Chem. Front.* 2019, 3 (3), 520-531.
57. Feng, X.; Jiao, Q.; Chen, W.; Dang, Y.; Dai, Z.; Suib, S. L.; Zhang, J.; Zhao, Y.; Li, H.; Feng, C., Cactus-like NiCo₂S₄@NiFe LDH hollow spheres as an effective oxygen bifunctional electrocatalyst in alkaline solution. *Appl. Catal. B: Environ.* 2021, 286, 119869.

58. Wang, J.; Song, Y.-F., Synchronous Electrocatalytic Design of Architectural and Electronic Structure Based on Bifunctional LDH-Co₃O₄/NF toward Water Splitting. *Chem. Eur. J.* 2021, 27 (10), 3367-3373.
59. Nie, F.; Li, Z.; Dai, X.; Yin, X.; Gan, Y.; Yang, Z.; Wu, B.; Ren, Z.; Cao, Y.; Song, W., Interfacial electronic modulation on heterostructured NiSe@CoFe LDH nanoarrays for enhancing oxygen evolution reaction and water splitting by facilitating the deprotonation of OH to O. *Chem. Eng. J.* 2022, 431, 134080.
60. Luo, J.; Im, J. H.; Mayer, M. T.; Schreier, M.; Nazeeruddin, M. K.; Park, N. G.; Tilley, S. D.; Fan, H. J.; Grätzel, M., Water photolysis at 12.3% efficiency via perovskite photovoltaics and Earth-abundant catalysts. *Science.* 2014, 345 (6204), 1593-6.
61. Zhang, X.; Qiu, Y.; Li, Q.; Liu, F.; Cui, L.; Li, C.; Liu, J., Sandwich structured Fe₃O₄/NiFe LDH/Fe₃O₄ as a bifunctional electrocatalyst with superior stability for highly sustained overall water splitting. *J. Alloys Compd.* 2023, 932, 167612.
62. Liu, F.; Guo, X.; Hou, Y.; Wang, F.; Zou, C.; Yang, H., Hydrothermal combined with electrodeposition construction of a stable Co₉S₈/Ni₃S₂@NiFe-LDH heterostructure electrocatalyst for overall water splitting. *Sustain. Energy Fuels.* 2021, 5 (5), 1429-1438.
63. Xu, X.; Su, L.; Zhang, Y.; Dong, L.; Miao, X., Hierarchical tube brush-like Co₃S₄@NiCo-LDH on Ni foam as a bifunctional electrocatalyst for overall water splitting. *New J. Chem.* 2021, 45 (34), 15429-15436.

Supporting Information

Contents

SI-I: Experimental

SI-II: Figures

SI-I: Experimental

Synthesis of Ni(OH)₂:

Ni(OH)₂ was synthesized by a simple one-step hydrothermal approach, approximately 2 mmole of Nickel nitrate hexahydrate Ni(NO₃)₂·6H₂O, is dissolved in 80 ml of NaOH (12 mmoles) later 1.04 mmole of sodium carbonate and 1 mmole of CTAB was added under constant vigorous stirring for 30 min at 950 rpm, later the contents are transferred into the Teflon lined autoclave and allow for undergoing reaction for 24 hrs at 180°C, later it allowed to cool down to room temperature and the contents are cleaned with acetone and ethanol.

Synthesis of Fe(OH)₂:

NiFe@LDH was synthesized by simple one-step hydrothermal approach, approximately 2 mmole of Ferrous nitrate nonahydrate Fe(NO₃)₂·9H₂O, is dissolved in 80 ml of NaOH (12 mmoles) later 1.04 mmole of sodium carbonate and 1 mmole of CTAB was added under constant vigorous stirring for 30 min at 950 rpm, later the contents are transferred into the Teflon lined autoclave and allow for undergoing reaction for 24 hrs at 180°C, later it allowed to cool down to room temperature and the contents are cleaned with acetone and ethanol.

SI-II: Figures

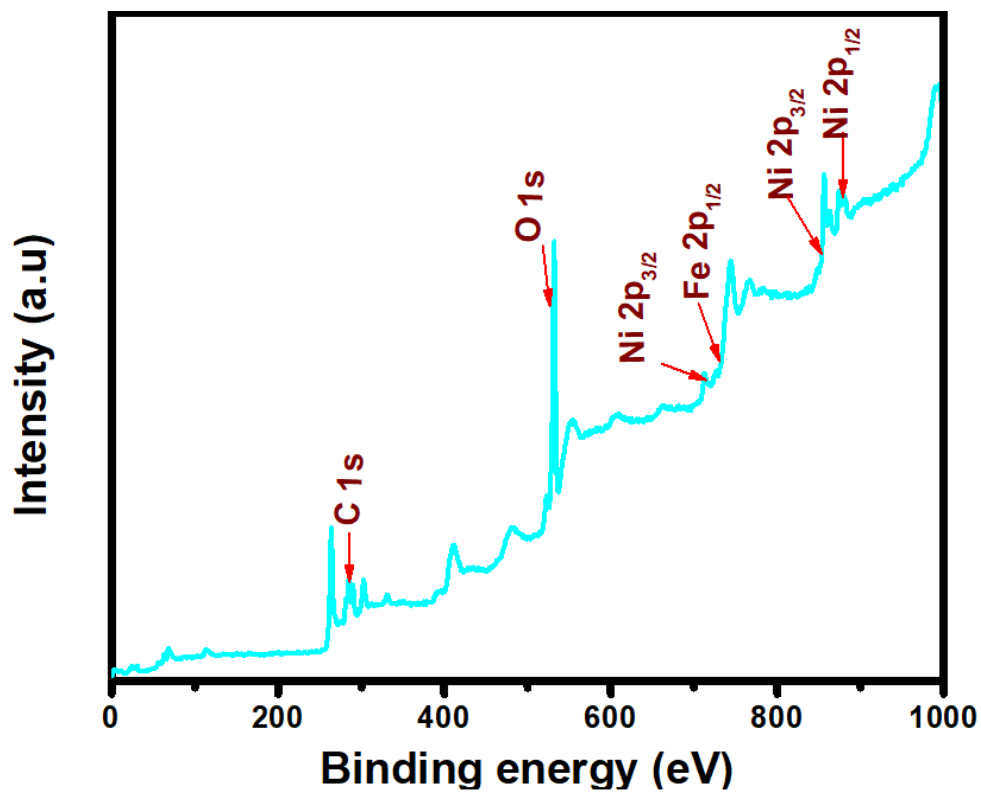


Figure S1. X-ray Photoelectron Spectroscopy Survey Spectrum.

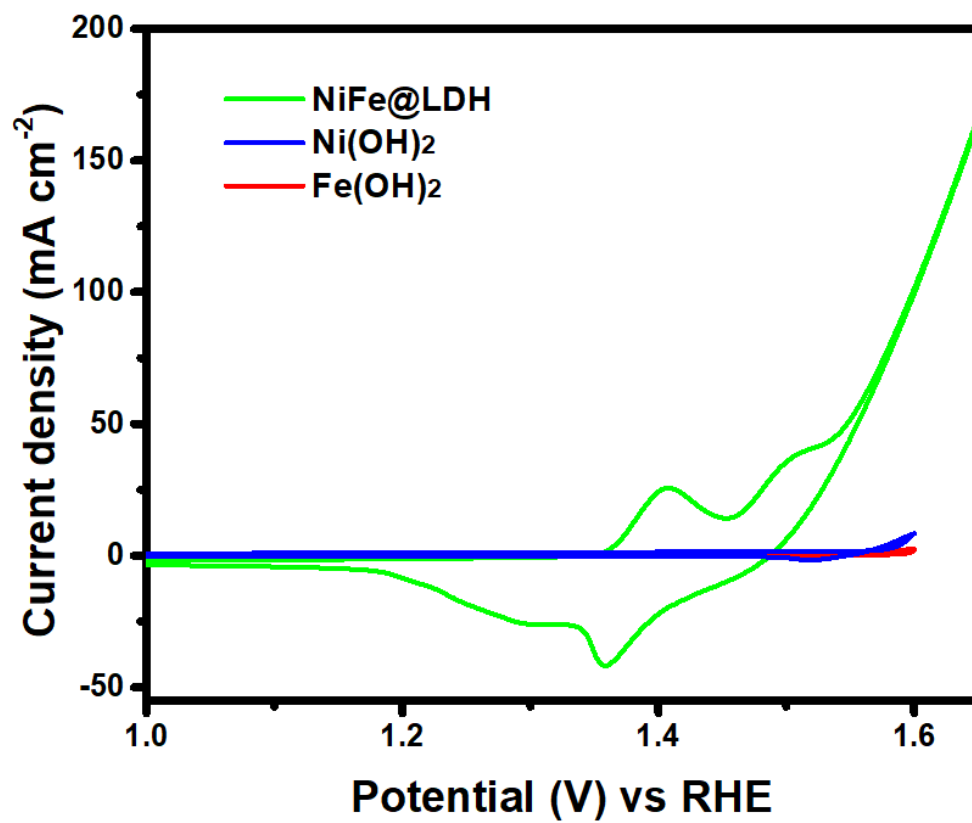


Figure S2. Cyclic Voltammogram (CV) of NiFe@LDH, Ni(OH)₂, and Fe(OH)₂.

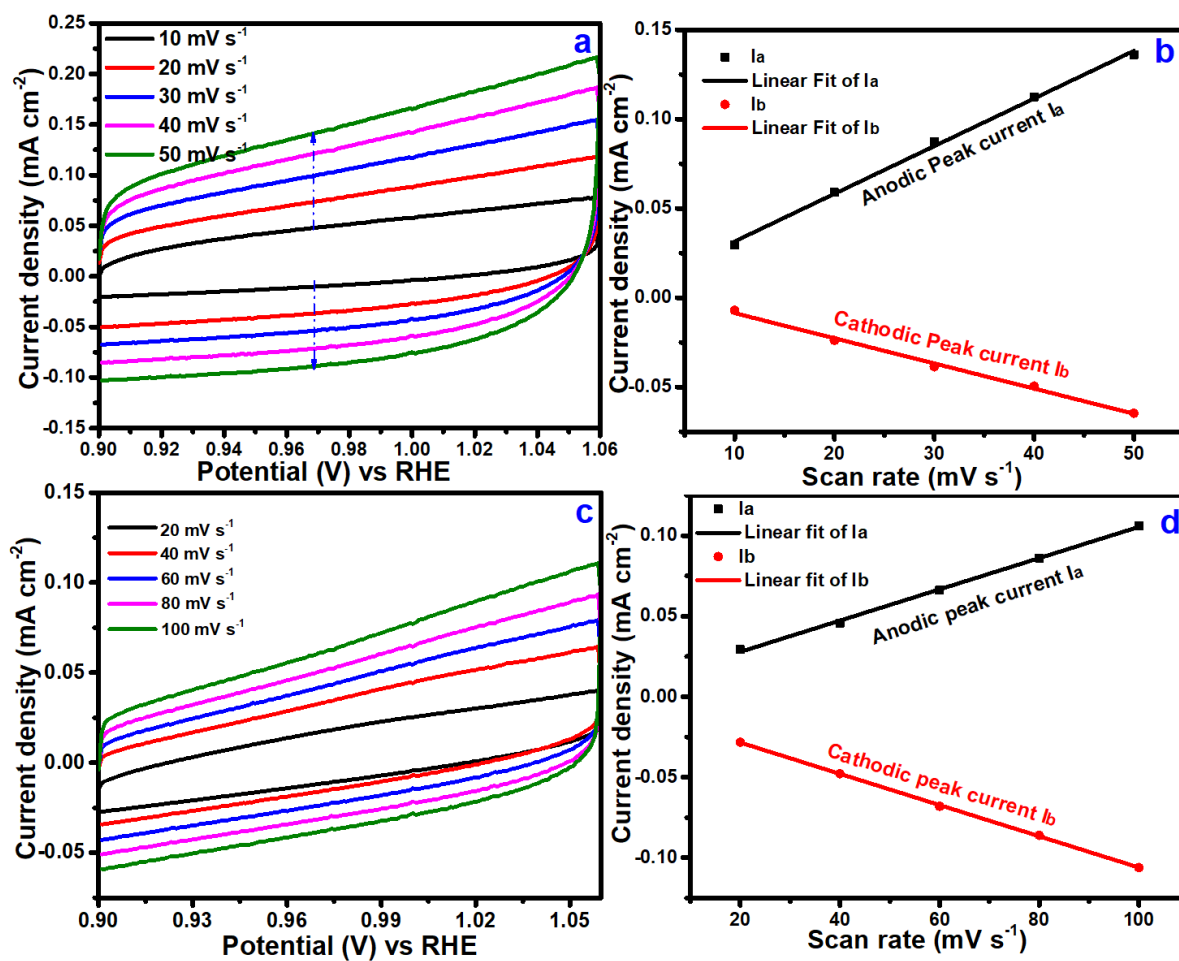


Figure S3. ECSA of electrocatalysts: (a, b) NiFe@LDH and (c, d) Bare NF.

Perspective of Electrochemical Biosensors in Agriculture

Jitendra Kumar^{1,2*}, **Bhanu Prakash Sandaka**^{1,2}, **Kuber C. Bhainsa**¹, and **Anand D. Ballal**^{1,2}

¹*Nuclear Agriculture and Biotechnology Division, Bhabha Atomic Research Centre,
Trombay, Mumbai, Maharashtra, India – 400085*

²*Homi Bhabha National Institute, Anushakti Nagar, Mumbai, Maharashtra, India – 400094*

E-mail: jkumar@barc.gov.in (Jitendra Kumar), aballal@barc.gov.in (Anand D. Ballal),
kuber@barc.gov.in (Kuber C. Bhainsa), sbhanu@barc.gov.in (Bhanu Prakash Sandaka)

Abstract

In light of the potential benefits of precision agriculture in the future, biosensors are bound to play a critical role in monitoring agriculture-related analytes, such as pesticides, nutrients, and metabolites pertaining to abiotic or biotic plant stress. This article provides a brief overview on the concept of biosensors and its potential uses in agriculture, with a special emphasis on electrochemical biosensors.

1. Introduction

With better resource management, precision agriculture (PA) reduces negative environmental consequences while increasing the agricultural output, which is an ingenious and sustainable approach. To ensure the steady operation of a sustainable and intelligent agricultural system, it is imperative to establish a monitoring system that furnishes crucial data for constructing a site-specific database on crop development, soil, and environmental parameters [1]. A wide range of analytical methods such as chemiluminescence, spectrophotometry, fluorescence, and chromatography have been used for monitoring plant

growth. However, this traditional analysis method is not suitable for on-site monitoring because the pre-treatment is complicated, requiring expensive equipment and highly skilled technicians. On the other hand, the biosensor detection system is particularly useful as it is a portable device that is convenient to use and has a fast response. A biosensor is an analytical device that integrates an immobilized biological element with a transducer to recognize the analyte and the signal due to interaction between analyte and biological element is proportional to the concentration of analyte. "L.L. Clark," an American scientist, invented the first biosensor in 1950. The electrode utilized in this biosensor, also known as the oxygen electrode or Clark electrode, is used to measure blood oxygen levels. Subsequently, the blood sugar was also determined by layering a gel comprising of an enzyme that oxidizes glucose on top of the oxygen electrode. Similarly, urea was determined in bodily fluids including (blood and urine) using the enzyme urease and an electrode specifically designed for NH_4 ions [2-11].

1.1. Biosensor concept

According to IUPAC, a biosensor is "a self-contained integrated device that is capable of providing specific quantitative or semiquantitative analytical information using a biological recognition element (biochemical receptor) that is retained in direct spatial contact with a transduction element". Biosensors are composed of biological components such as enzymes, nucleic acids, aptamers, cells, antibodies, or antigens, and physical components such as a transducer, signal, a processor and a screen for display. A schematic of how a biosensor works is indicated in Figure 1. A common working definition is that biosensors are analytical devices that use biological components to recognize an analyte and subsequently activate a signal that is detected with a transducer. However, this common working definition does not suggest an integrated device in which the transducing element is in spatial contact with the biorecognition element [8-11].

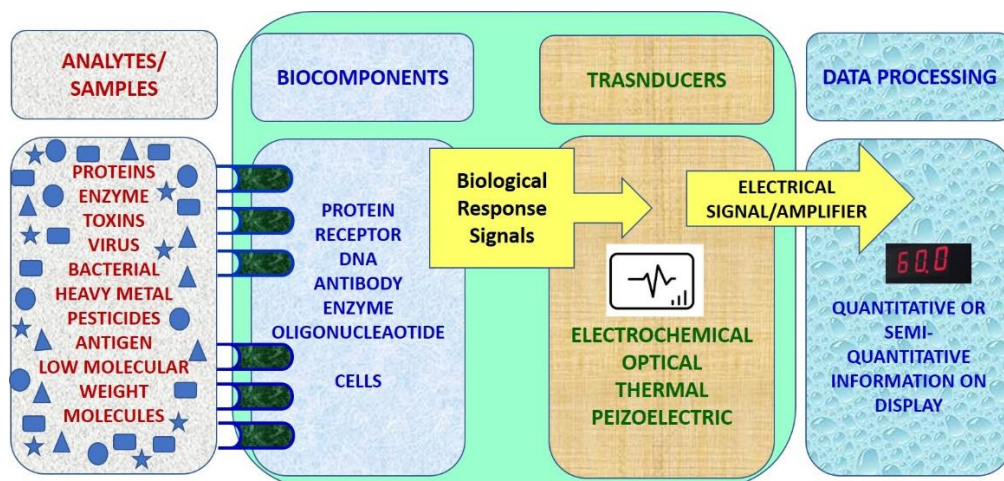


Figure 1. Schematic diagram explaining the principle of biosensor

A physicochemical transducer or transducing microsystems that are either closely linked to or incorporated inside a biological material (a material derived from biology) or a biomimic, are used as the recognition molecules in biosensors. Producing a digital electrical signal that is proportionate to the concentration of a particular analyte or collection of analytes is often the objective. Biosensor facilitates onsite detection of a large number of samples with no or very little preparation, minimal time requirement and no requirement of expensive apparatus or trained personnel which are generally limitation in traditional analytical methods.

1.2. Types of Biosensors

Different kinds of biosensors are essentially based on two elements, namely the sensing (or recognition) element and transducing element (Figure 2).

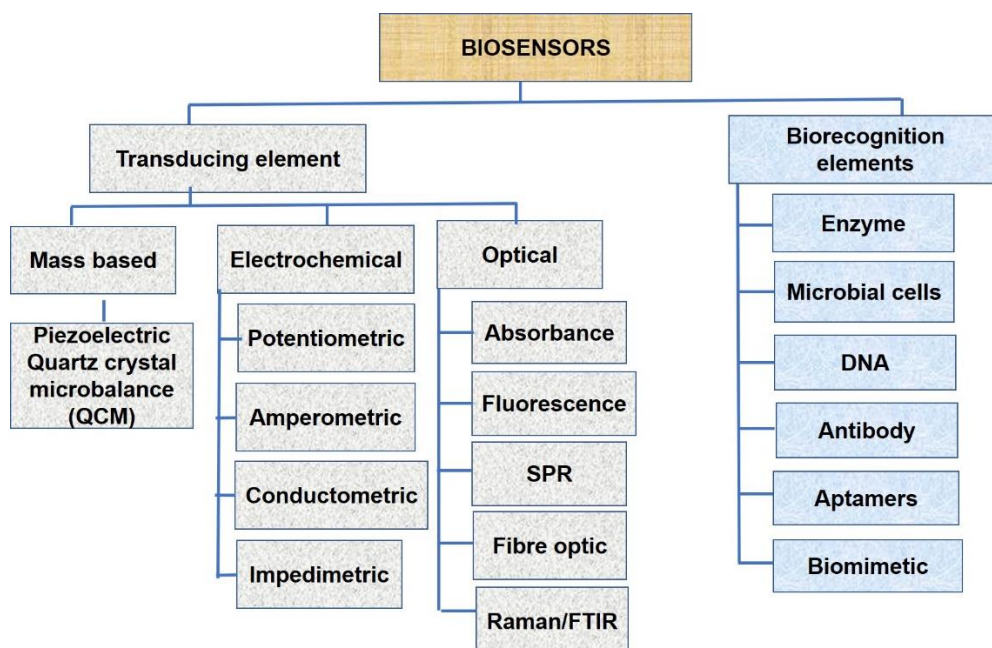


Figure 2. Types of Biosensors

Based on the activity of the biorecognition element, biosensors are divided into affinity and catalytic biosensors. The affinity biosensors recognize the analyte by binding to the analyte i.e. biorecognition is their fundamental property, e.g., antibody–antigen, DNA, aptamers etc. Catalytic biosensors have enzymes (or microorganisms) as their biorecognition elements that not only bind the analyte, but also catalyses a reaction involving the analyte to produce a product, e.g., glucose biosensors.

The transducer, a chief component of biosensors, plays an important role in the signal the detection process. Transducers convert a wide range of physical, chemical, or biological reactions into an electrical signal. Depending on the type of transduction signal, the biosensors can be distinguished into optical, piezoelectric, and electrochemical biosensors [8-11].

1.2.1. Electrochemical biosensors

An electrochemical biosensor is a self-contained integrated device that provides quantitative or semi-quantitative analytical information by using a biological recognition

element (biochemical receptor) that is maintained in direct spatial contact with an electrochemical transduction element. The term electrochemistry refers to the application of electrochemical tools for the recognition of analyte that exhibits electroactivity. Several modern electrochemical techniques have been created to investigate the fundamentals of electrochemical processes and to identify various electrochemical characteristics of electroactive species by measuring the voltage or current in an electrochemical cell. Most of the electroanalytical methods operate a three-electrode cell design for electrochemical measurements.

2. Perspectives of biosensors in agriculture

Agriculture is a complex but a systematic practice that includes various process, techniques, methods and technologies, which eventually allow the produce reach from farm to fork. Early detection of crucial analytes is essential in the agricultural field because crop illnesses, insect damage, weed infestations, water shortages or surpluses, managing floods, assessing crop nutrition, and other issues, which can cause severe damage, are mostly preventable. There is cause for concern since herbicide, pesticide, and heavy metal concentrations are increasing in agricultural areas. The concentrations of chemicals such as pesticides, herbicides, and heavy metals in the soil and groundwater can be determined using biosensors. With the development of this technology, biosensors can now be used to anticipate the probable emergence of soil-borne disease. The use of herbicides, pesticides, and heavy metals is intensifying in agriculture, which is cause for concern. The concentrations of pesticides, herbicides, and heavy metals in the soil and groundwater can be determined using biosensors. It is also now possible to predict the potential appearance of soil-borne diseases using biosensors. By biologically identifying the disease-causing organisms in the soil using a biosensor, the oil-borne disease can be reliably prevented and the soil can be decontaminated at an early stage. The ability of humans to oversee quality has long been a requirement in the

agriculture sector. Therefore, all needs for accelerating the production of agricultural items can be met by biosensors. There are various stages in agriculture where monitoring of required analytes can be made, to improve agriculture (Figure 3) [1, 10-12].

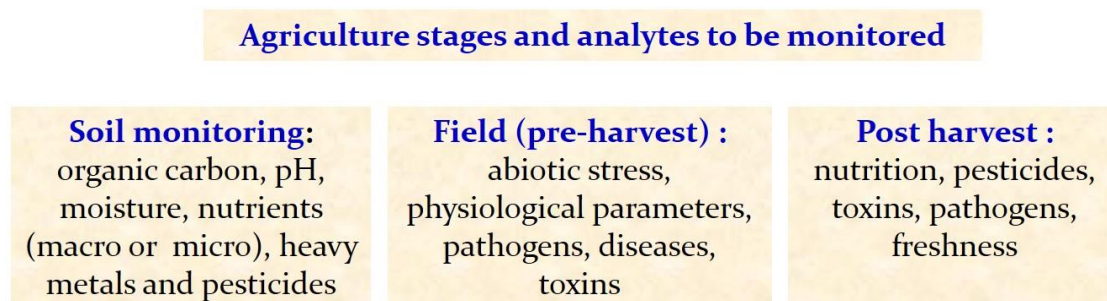


Figure 3. Scope of biosensors in agriculture for monitoring of analytes

Several kinds of biosensors have uses in agriculture since they work on the principle of turning biological signal into electronic signals. Moreover, biosensors are quick, dependable, and accurate analytical tools. Electroanalytical techniques can also be applied quickly and simply to agriculture fields, in real-time, due to their high levels of accuracy, precision, sensitivity, and selectivity. In next section, we report the electrochemical sensor's analytical performance, establish its effectiveness and broad application in agriculture.

3. Applications of electrochemical biosensors in agriculture

Electrochemical techniques have been widely incorporated in biosensors for monitoring analytes related to agriculture such as pesticides, nutrients, metabolites altered during plant stress, chemicals, plant pathogens etc. (Table 1) [13]. This section is a bibliographic compilation of electrochemical methods in use, such as transducers for detection of agriculture related analytes.

Organophosphorus (OP) pesticides have been widely used in the field of agriculture for the control insect pests. These pesticides and their degradation products cause environmental pollution, resulting in ecological crisis. Methyl parathion (a nitro-aromatic

organophosphate compound), although very toxic to mammals was widely used as an insecticide. Our laboratory has developed an electrochemical microbial biosensor by immobilizing recombinant *E. coli*, having organophosphorus hydrolase enzyme, on a screen-printed carbon electrode (SPCE) and integrated this system with an electrochemical analyzer for detection of methyl parathion using the cyclic voltammetry method (Figure 4) [14].

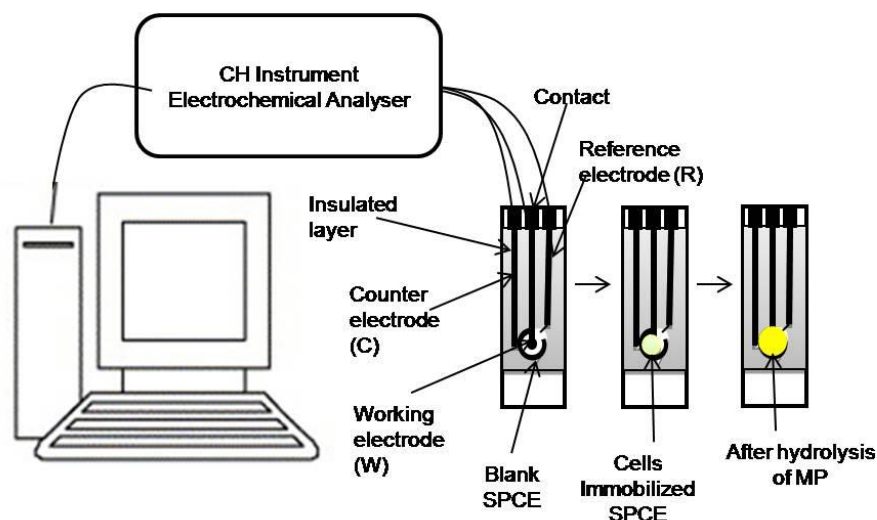


Figure 4. Schematic diagram of electrochemical biosensor using cells immobilized SPCE

Along similar lines, many acetylcholinesterase based electrochemical biosensors have reported for monitoring of dichlorvos pesticides [11].

The development of a simple, economically feasible, and rapid detection technique for the identification of nutrients especially, NPK, is mandatory. In last decade, various types of sensors, such as electrochemical sensors, optical sensors, and mass-sensitive biosensors have been developed for the detecting NPK in soil. Among these biosensors, an electrochemical sensor the most sensitive and rapid tools for NPK detection. It is a promising strategy for developing an innovative, cost-effective, and portable NPK testing method for soil. Recently, Hossain et al., (2024), have compiled an excellent review which has focused on the

development of electrochemical sensors to rapidly detect macronutrients, i.e., nitrogen (N), phosphorus (P), and potassium (K), in soil or water [15].

Pathogens are infectious agents that cause disease. They include microorganisms, such as fungi, protozoans, and bacteria, and molecular-scale infectious agents, including viruses and prions. Ellen Cesewski and Blake N. Johnson, (2020) have published a critical review on electrochemical biosensors for pathogen detection [16]. Electrochemical biosensors for pathogen detection are broadly reviewed in terms of transduction elements, biorecognition elements, electrochemical techniques, and biosensor performance. Transduction elements are discussed in terms of electrode material and form factor. Biorecognition elements for pathogen detection, including antibodies, aptamers, and imprinted polymers, are discussed in terms of availability, production, and immobilization approach. Emerging areas of electrochemical biosensor design are reviewed, including electrode modification and transducer integration.

Table 1. Examples of Electrochemical Biosensor for monitoring of agriculture related analytes.

Agricultural applications	Analytes	Electrochemical technique	Ref
Pesticides	Methyl parathion	Cyclic Voltammetry	[14]
Pesticides	Dichlorvos	Amperometric	[11]
Nutrients	NPK	Electrochemical	[15]
Plant pathogen	Soybean rust Fungal spores	Electrochemical immunosensor	[17]

Plant pathogen	Plum pox virus	Electrochemical impedance spectroscopy	[18]
Abiotic stress in plants	Indole 3- Acetic Acid in Plant	Amperometric	[19]

4. Conclusion and future aspects

In this article, we have attempted to emphasize the importance of biosensors, especially electrochemical biosensors, in order to monitor the agriculturally-relevant analytes. we have also analyzed the key advancements and uses of electrochemical biosensors in precision agriculture. Looking back at this analysis, we think that the use of electrochemical multi-sensors for monitoring plant health can be a primary tool Precision Agriculture going forward. We hope that this review will help further the field of smart farms by encouraging more researchers to investigate plant sensor systems for precision agriculture.

References:

1. J. Kumar, B.P. Sandaka (2021) Biosensors for Pesticides: From concept to the field application; SMC Bulletin: Special Issue on Materials for Biosensing Applications, 12 (03) 109-114.
2. J. Kumar, J.S. Melo (2015) Microbial Biosensors for Methyl Parathion: From Single to Multiple Samples Analysis, in: T.G. Everett (Ed.), Adv. Biosens. Reserach, New York, pp. 89–111.
3. J. Kumar, A. Mishra, J.S. Melo (2018) Biodegradation of Methyl Parathion and its Application in Biosensors, Austin J. Environ. Toxicol. 4, 1024.
4. J. Kumar, S.F. D'Souza (2010) An optical microbial biosensor for detection of methyl parathion using *Sphingomonas* sp. immobilized on microplate as a reusable biocomponent, Biosens. Bioelectron. 26, 1292–1296. <https://doi.org/10.1016/j.bios.2010.07.016>.
5. J. Kumar, S.F. D'Souza (2011) Immobilization of microbial cells on inner epidermis of onion bulb scale for biosensor application, Biosens. Bioelectron. 26, 4399–4404. <https://doi.org/10.1016/j.bios.2011.04.049>.
6. A. Mishra, J. Kumar, J.S. Melo (2017) An optical microplate biosensor for the detection of methyl parathion pesticide using a biohybrid of *Sphingomonas* sp. cells-silica nanoparticles, Biosens. Bioelectron. 87, 332–338.
7. J. Kumar, S.K. Jha, S.F. D'Souza (2006) Optical microbial biosensor for detection of methyl parathion pesticide using *Flavobacterium* sp. whole cells adsorbed on glass fiber filters as disposable biocomponent, Biosens. Bioelectron. 21, 2100–2105. <https://doi.org/10.1016/j.bios.2005.10.012>.
8. J. Kumar, J.S. Melo (2017) Overview on Biosensors for Detection of Organophosphate Pesticides, Curr. Trends Biomed. Eng. Biosci. 5, 555663. <https://doi.org/10.19080/CTBEB.2017.05.555663>.

9. Kumar J., Kumar D. (2023) Sensing Approaches for Industrial Waste Management: View Point from Personal and Societal Healthcare; Chapter 14 In book: Health and Environmental Applications of Biosensing Technologies, Publisher: Elsevier.
10. A. Ahamad, J. Kumar (2023) Pyrethroid pesticides: an overview on classification, toxicological assessment and monitoring. *J. Hazard. Mater. Adv.*, 10 (2023), Article 100284, 10.1016/j.hazadv.2023.100284.
11. A. Mishra, J. Kumar, J.S. Melo, B.P. Sandaka (2021) Progressive development in biosensors for detection of dichlorvos pesticide: a review. *J. Environ. Chem. Eng.*, 9 (2021), pp. 105067-105434.
12. R.N. Pudake, U. Jain, C. Kole (2021) *Biosensors in Agriculture: Recent Trends and Future Perspectives*, Springer.
13. M-Y, Kim, K.H. Lee (2022) Electrochemical Sensors for Sustainable Precision Agriculture—A Review. *Front. Chem.* 10:848320. doi: 10.3389/fchem.2022.848320
14. J. Kumar, S.F. D'Souza (2011) Microbial biosensor for detection of methyl parathion using screen printed carbon electrode and cyclic voltammetry, *Biosens. Bioelectron.* 26 4289–4293. <https://doi.org/10.1016/j.bios.2011.04.027>.
15. M.I. Hossain, M.A. Khaleque, M.R. Ali, M.S. Bacchu, M. S. Hossain, S.M.F. Shahed, M. Aly Saad, Md. Z.H. Khan (2024) Development of electrochemical sensors for quick detection of environmental (soil and water) NPK ions. *RSC Adv.*, 2024,14, 9137-9158. DOI:10.1039/D4RA00034J.
16. E. Cesewski, B.N. Johnson (2020) Electrochemical biosensors for pathogen detection, *Biosensors and Bioelectronics*, 159, 112214, ISSN 0956-5663, <https://doi.org/10.1016/j.bios.2020.112214>.
17. R.K. Mendes, D.C.M. Ferreira, R.F. Carvalhal, L.A. Peroni, D.R. Stach-Machado, L.T. Kubota, (2009) Development of an electrochemical immunosensor for Phakopsora

- pachyrhizi detection in the early diagnosis of soybean rust. *J. Braz. Chem. Soc.*, 20(4):795-801. DOI: 10.1590/S0103-50532009000400023.
18. U. Jarocka, Wałsowicz, M., H. Radecka, T. Malinowski, L. Michalczyk, J. Radecki, (2011) Impedimetric immunosensor for detection of plum pox virus in plant extracts. *Electroanalysis* 23, 2197–2204. doi:10.1002/elan.201100152.
19. K.K. Subraya, A. Diggs, D.M. Porterfield, (2013). Amperometric biosensor approaches for quantification of indole 3-acetic acid in plant stress responses. *Commun. Soil Sci. Plant Anal.*, 44(11), 1749-1763.

Comparative Electrochemical Studies of Binary Metal Oxide Nanocomposite on GCE and NF Substrates for Supercapacitor Application

Bhakti G. Thali and Rajesh M. Kamble*

Electro-Analytical Research Laboratory, Department of Chemistry, University of Mumbai, Santacruz (E), Mumbai 400 098, India

E-mail: *kamblerm@chem.mu.ac.in*

Abstract:

The article outlines a study focusing on a binary composite, $\text{CuCo}_2\text{O}_4@\text{Co}_3\text{O}_4$, synthesized using a simple hydrothermal method aimed at energy storage applications. Various characterization techniques such as FT-IR, XRD, FE-SEM, and XPS confirmed the successful formation of the nanocomposite. Electrochemical assessments including cyclic voltammetry (CV), Galvanostatic Charge-Discharge (GCD), and Electrochemical Impedance Spectroscopy (EIS) demonstrated specific capacitances 542.77 Fg^{-1} on Glassy Carbon Electrode (GCE) and 683.72 Fg^{-1} on Nickel foam (NF), both at 1 Ag^{-1} current density. The composite exhibited pseudocapacitive behaviour in 1 M Na_2SO_4 and 1 M KOH electrolytes. Impedance analysis affirmed the capacitive nature of the materials. Cyclic stability was observed using Glassy Carbon Electrode (GCE) was 76% retention over 1000 cycles and Nickel foam (NF) was 78% retention over 3000 cycles at 5 Ag^{-1} . As a result of the investigation, the $\text{CuCo}_2\text{O}_4@\text{Co}_3\text{O}_4$ nanocomposite exhibits promising characteristics as an efficient electrode material in energy storage applications.

Keywords: Binary Metal Oxide Nanocomposite, Electrochemical performance, Supercapacitors

1. Introduction

Due to environmental pollution and the depletion of fossil fuels, coupled with regional dependence on renewable energies like solar, wind, and tidal power, clean and recyclable energy storage and conversion systems have become a highly prioritized area of research [1]. The performance of supercapacitors heavily relies on electrode materials, prompting significant efforts to develop novel materials with enhanced capabilities [2,3]. Metal oxides are preferred in pseudocapacitors due to their high specific capacitance and low resistance, whereas conducting polymers are preferred for their ionic interaction and conductivity. Transition metal oxides, with their variable oxidation states and faradic properties, are particularly suitable for applications such as fuel cells, sensors, and solar cells [4]. Nanostructured metal oxides, characterized by their high aspect ratio, exhibit strong capacitive and sensing properties [5]. Among pseudocapacitive materials, spinel structures composed of binary or ternary metal oxides are studied for energy storage applications [6]. Spinel cobaltites (MCo_2O_4), featuring mixed-valence metal cations, offer superior electrical conductivity and electrochemical activity compared to single-component oxides [7], making them promising electrode materials for Li-ion batteries and supercapacitors. $CuCo_2O_4$, a non-toxic and cost-effective cobaltite spinel is specifically studied here to enhance electrode kinetics for rapid ion insertion/de-insertion, utilizing nanostructures like nanoparticles and nanowires [8, 9].

Previous research by Wang et al. synthesized $CuCo_2O_4$ nanowire arrays on carbon fabric substrates, achieving a specific capacitance of 57.8 Fg^{-1} at 1.25 Ag^{-1} [10]. To enhance performance further, they developed core-shell $CuCo_2O_4@MnO_2$ heterostructured nanowire arrays, achieving a maximum specific capacitance of 327 Fg^{-1} [11]. Cobalt-based semiconductors like Co_3O_4 have also garnered interest for electrochemical devices and catalysis due to their visible-light sensitivity, chemical stability, and unique electronic structure [12]. However, nanoparticle structures of Co_3O_4 often suffer from aggregation and deactivation during photocatalytic processes [13], prompting efforts to create stable multiscale structures

for improved electrochemical sensors and supercapacitors [14]. The complementary features and closely matched band structures of CuCo_2O_4 and Co_3O_4 suggest that their coupling could enhance supercapacitive performance [15]. In this study, a novel binary composite $\text{CuCo}_2\text{O}_4@ \text{Co}_3\text{O}_4$ is synthesized for supercapacitor applications [16]. Pure Co_3O_4 and CuCo_2O_4 samples are also synthesized and characterized using X-ray diffraction (XRD), Fourier transform infrared spectroscopy (FT-IR), field emission scanning electron microscopy (FE-SEM), energy-dispersive X-ray analysis (EDX), and X-ray photoelectron spectroscopy (XPS). Electrochemical performance is evaluated through cyclic voltammetry (CV), Galvanostatic Charge-Discharge (GCD), and Electrochemical Impedance Spectroscopy (EIS) using Glassy Carbon Electrode (GCE) and Nickel Foam substrates. This comprehensive approach aims to provide insights into the electrochemical behaviour and potential applications of synthesized nanomaterials in energy storage technologies.

2. Experimental Section

2.1 Materials

The initial raw materials used for synthesizing the nanomaterials were purified copper chloride hexahydrate ($\text{CuCl}_2 \cdot 2\text{H}_2\text{O}$), extra pure AR grade cobalt chloride ($\text{CoCl}_2 \cdot 6\text{H}_2\text{O}$), ethyl acetate, and urea. All chemicals were sourced from Sigma Aldrich and used without further purification. Throughout the experiments, double distilled and deionized water was used exclusively.

2.2 Synthetic Procedures

2.2.1 Synthesis of Cobalt oxide nanoparticles

Cobalt oxide nanoparticles were prepared using a straightforward hydrothermal method. A mixture of 0.52g $\text{CoCl}_2 \cdot 6\text{H}_2\text{O}$ and 0.67g $\text{CO}(\text{NH}_3)_2$ was dissolved in 25 ml of double distilled

water with vigorous stirring. The solution was transferred into a Teflon-lined autoclave and heated at 80 °C for 12 hours. The resulting product was centrifuged, washed with distilled water and ethanol, and then dried at 60 °C. Finally, the Co₃O₄ nanoparticles were obtained by calcining the powder at 350 °C for 2 hours in a muffle furnace.

2.2.2 Synthesis of CuCo₂O₄ nanoparticles

CuCo₂O₄ nanoparticles were synthesized by mixing 1 mmol each of CoCl₂·6H₂O and CuCl₂·2H₂O in 40 ml of double distilled water. 15 ml NH₃·H₂O was added to the solution, followed by stirring. The mixture was then transferred to a Teflon-lined autoclave and heated at 140 °C for 24 hours. The resulting powder was washed with ethanol, dried at 60 °C, and further calcined at 350 °C for 2 hours in a muffle furnace to obtain CuCo₂O₄ nanoparticles.

2.2.3 Synthesis of CuCo₂O₄@Co₃O₄ nanocomposite

To prepare the CuCo₂O₄@Co₃O₄ nanocomposite, a solution containing 2 mmol CoCl₂·6H₂O and 1 mmol CuCl₂·2H₂O in 40 ml double distilled water was prepared similarly as for CuCo₂O₄ nanoparticles. The solution was subjected to autoclaving at 140 °C for 24 hours. The solid obtained was washed thoroughly with water and ethanol and then dried at 60 °C. Finally, the CuCo₂O₄@Co₃O₄ nanocomposite was obtained by calcining the powder at 350 °C for 4 hours in a muffle furnace.

3. Results and Discussion

3.1 Functional and Crystallographic Studies

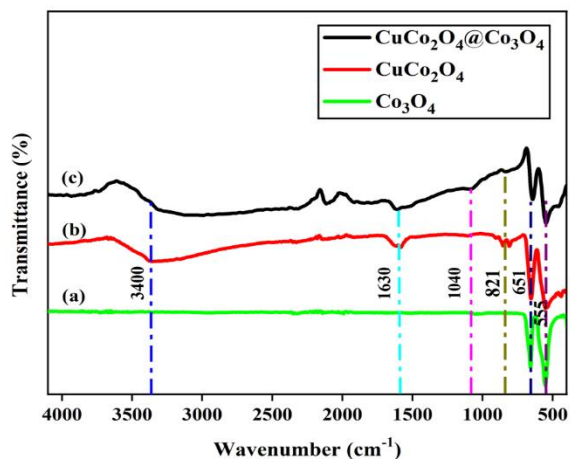


Fig. 1. FT-IR spectrum of Co_3O_4 (a), CuCo_2O_4 (b), and $\text{CuCo}_2\text{O}_4@\text{Co}_3\text{O}_4$ (c).

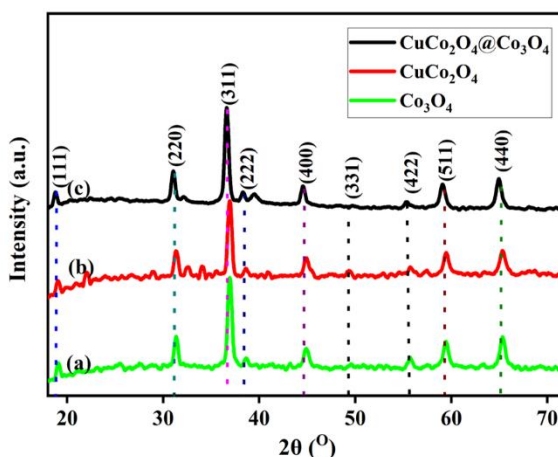


Fig. 2. XRD pattern of Co_3O_4 (a), CuCo_2O_4 (b), and $\text{CuCo}_2\text{O}_4@\text{Co}_3\text{O}_4$ (c).

Fourier transform infrared (FT-IR) spectroscopy was employed on Co_3O_4 , CuCo_2O_4 , and $\text{CuCo}_2\text{O}_4@\text{Co}_3\text{O}_4$ over the range of $4000\text{--}400\text{ cm}^{-1}$ to confirm the successful formation of these synthesized nanomaterials, as illustrated in **Fig. 1**. The FT-IR spectrum of Co_3O_4 displayed in **Fig. 1 (a)**, exhibits characteristic peaks at 555 cm^{-1} and 651 cm^{-1} , corresponding to Co-O stretching and Co-O bending vibrations, respectively, confirming the formation of Co_3O_4 nanoparticles. The peak at 555 cm^{-1} primarily indicates vibrations involving Co^{3+} , while the peak at 651 cm^{-1} involves Co^{2+} , Co^{3+} , and O in the spinel structure of Co_3O_4 [17]. In **Fig. 1 (b)**, the FT-IR spectrum of CuCo_2O_4 shows peaks at 555 cm^{-1} and 651 cm^{-1} , confirming the formation of the pure spinel phase CuCo_2O_4 nanomaterial [18]. Additionally, an absorption band observed at 3400 cm^{-1} indicates O-H stretching, and a band at 1630 cm^{-1} is attributed to H-O-H bending vibration mode [19]. Additionally, the peaks observed at 1040 cm^{-1} and 821 cm^{-1} in the FT-IR spectrum of $\text{CuCo}_2\text{O}_4@\text{Co}_3\text{O}_4$ indicate interactions between the pure CuCo_2O_4 and Co_3O_4 synthesized nanomaterials, respectively.

The crystallographic analysis was conducted to validate all the synthesized nanomaterials as depicted in **Fig. 2**. In **Fig. 2 (a)**, the X-ray diffraction (XRD) pattern of pure Co_3O_4 shows

distinct diffraction peaks corresponding to JCPDS No. 76–1802, confirming its cubic symmetry. The diffraction peaks observed for Co_3O_4 nanoparticles include (111), (220), (311), (400), (511), and (440), with the most prominent peak at $2\theta = 36.85^\circ$ corresponding to the (311) plane, indicating good crystallinity [17]. **Fig. 2 (b)** shows the XRD pattern of synthesized CuCo_2O_4 nanomaterial, where the diffraction peaks match well with JCPDS card no. 01-1155, corresponding to planes (111), (220), (311), (222), (400), (331), (422), (511), and (440) with cubic symmetry [20]. Similarly, **Fig. 2 (c)** represents the XRD pattern of $\text{CuCo}_2\text{O}_4@\text{Co}_3\text{O}_4$ nanocomposite, revealing diffraction peaks at (220), (111), (311), (222), (400), (331), (422), (440), and (511), confirming the successful formation of the binary composite.

3.2 Morphological Studies with Elemental Analysis

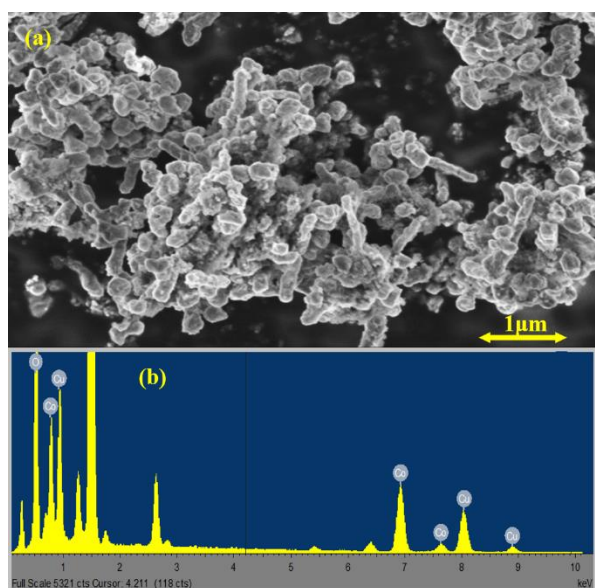


Fig.3. SEM micrographs of $\text{CuCo}_2\text{O}_4@\text{Co}_3\text{O}_4$ (a) and EDS spectrum of $\text{CuCo}_2\text{O}_4@\text{Co}_3\text{O}_4$ (b).

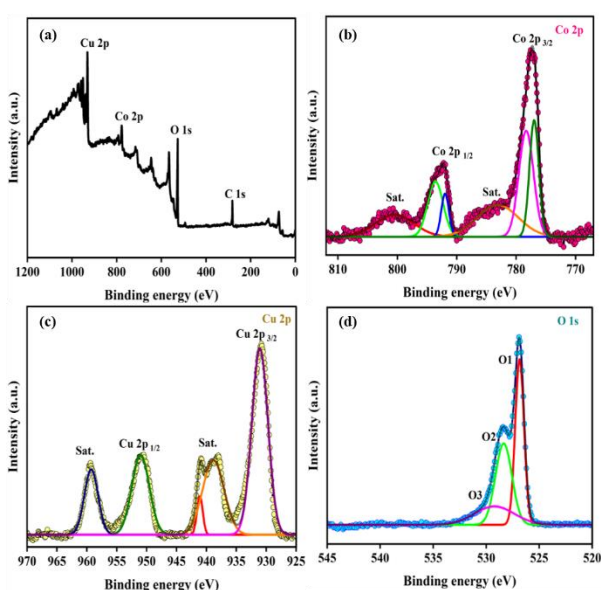


Fig. 4. XPS spectra of $\text{CuCo}_2\text{O}_4@\text{Co}_3\text{O}_4$ (a), Survey scan from 0 to 1000 eV; Fitted XPS spectra of (b) Co 2p; (c) Cu 2p; (d) O 1s; signals.

The surface roughness of the $\text{CuCo}_2\text{O}_4@\text{Co}_3\text{O}_4$ nanocomposite was assessed through FE–SEM analysis, highlighting features that could influence its electrochemical properties. The FE–SEM analysis of the $\text{CuCo}_2\text{O}_4@\text{Co}_3\text{O}_4$ nanocomposite displayed in **Fig. 3 (a)** typically revealed a combination of regular rod-shaped particles and various spherical structures with an average diameter of approximately 100–120 nm [16]. The different elements present in the $\text{CuCo}_2\text{O}_4@\text{Co}_3\text{O}_4$ nanocomposite were identified using the EDS technique. The EDS sum spectrum, which includes all the elements of the hybrid nanocomposite along with their corresponding elemental mapping, is shown in **Fig. 3 (b)**.

Additionally, X–ray photoelectron spectroscopy (XPS) was used to validate the complementary information obtained from EDS analysis and to understand the surface states and the nature of chemical bonding of all the elements in the nanocomposite. The wide survey spectrum for $\text{CuCo}_2\text{O}_4@\text{Co}_3\text{O}_4$, shown in **Fig. 4 (a)**, displays distinct peaks at various binding energies in the 50–1000 eV range, corresponding to Co 2p, Cu 2p, and O 1s elemental states respectively. This spectrum confirms the presence of Co, Cu, and O in the $\text{CuCo}_2\text{O}_4@\text{Co}_3\text{O}_4$ composite. The peak at 285.1 eV (C 1s) is used as an internal reference. **Fig. 4 (b)** shows two prominent peaks at 778.51 and 796.94 eV, along with two satellite peaks at 784.23 and 800.87 eV, indicating the presence of Co^{2+} in the composite. Additionally, peaks at 777.12 and 792.90 eV indicate the presence of Co^{3+} . Thus, cobalt exists in both oxidation states, Co^{2+} and Co^{3+} , in the $\text{CuCo}_2\text{O}_4@\text{Co}_3\text{O}_4$ composite. The spectrum for Cu 2p is depicted in **Fig. 4 (c)**, showing two major peaks at 931.02 and 951.25 eV, along with satellite peaks at 940.94 and 959.28 eV for the Cu 2p_{3/2} and Cu 2p_{1/2} bands, respectively, confirming the presence of Cu^{2+} in the CuCo_2O_4 nanoparticles. This indicates the successful synthesis of the $\text{CuCo}_2\text{O}_4@\text{Co}_3\text{O}_4$ nanocomposite. **Fig. 4 (d)** shows the XPS spectra of O 1s, which can be deconvoluted into three peaks: O1 at 526.86 eV, O2 at 528.37 eV, and O3 at 530.1 eV. These peaks correspond to the metal–oxygen bonds present in the nanocomposite [16].

3.3 Electrochemical characterization

The electrochemical measurements of the synthesized materials were evaluated using an Autolab PGSTAT302N electrochemical workstation equipped with NOVA software, within a potential range of -0.2 to $+0.8$ V. The electrochemical properties of the synthesized materials Co_3O_4 , CuCo_2O_4 , and $\text{CuCo}_2\text{O}_4@\text{Co}_3\text{O}_4$ composite were assessed using two different electrode substrates (GCE and NF). For electrochemical measurements on GCE, the active material was taken along with Carbon black and Polyvinylidene fluoride (PVDF) in the ratio 80:10:10 dispersed in a mixture of 10 μl of ethanol and 10 μl of Dimethylformamide (DMF), followed by sonication for 1 hour and then it was drop-casted and kept for drying at 80°C for 5 hours. 1 M Na_2SO_4 was used as an electrolyte for recording electrochemical studies. Before using NF (1 cm X 1cm) as a substrate, it was subjected to a cleaning procedure using 1 M HCL, acetone, and distilled water. Further same binder and conductive agent were used. Only the solvent used was NMP and measurements were recorded in 1 M KOH.

Specific capacitance can be calculated using the following formula:

$$C = \frac{I\Delta t}{m\Delta V}$$

Where C is the capacitance (F/g), I is the current density (A/g), Δt is the discharge time (s), and Δv is the working potential difference of the electrochemical cell [21].

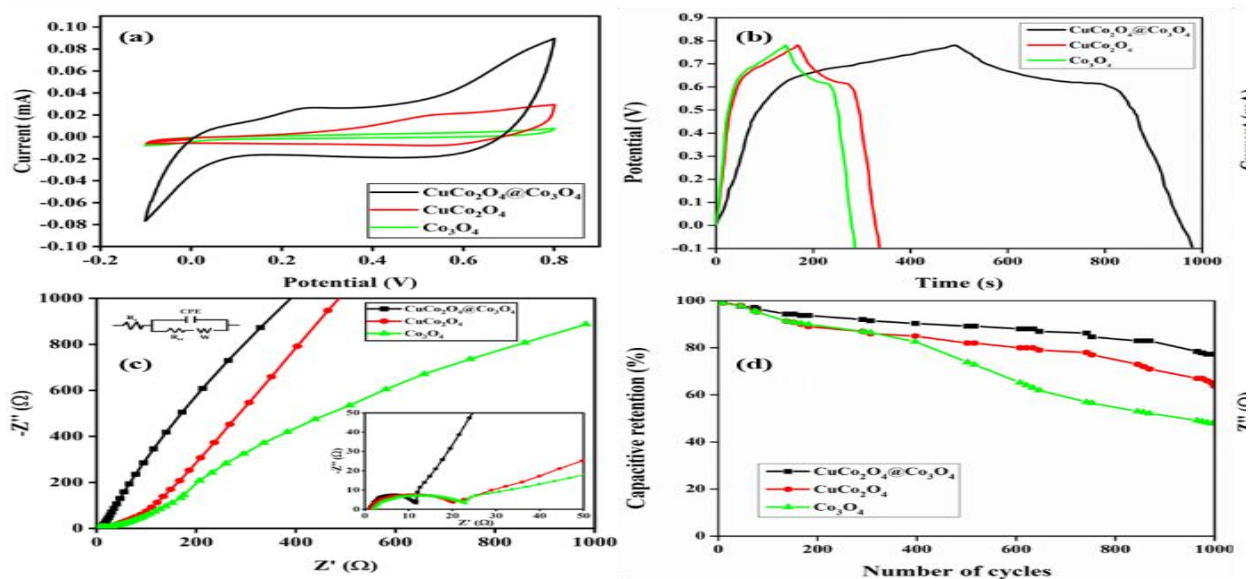


Fig. 5. CV of Co_3O_4 , CuCo_2O_4 , and $\text{CuCo}_2\text{O}_4@/\text{Co}_3\text{O}_4$ at 100 mV/s (a), GCD of Co_3O_4 , CuCo_2O_4 , and $\text{CuCo}_2\text{O}_4@/\text{Co}_3\text{O}_4$ at 1 A/g (b), and Nyquist plots of the samples (c), and Cyclic stability at 5 A/g (d) on GCE.

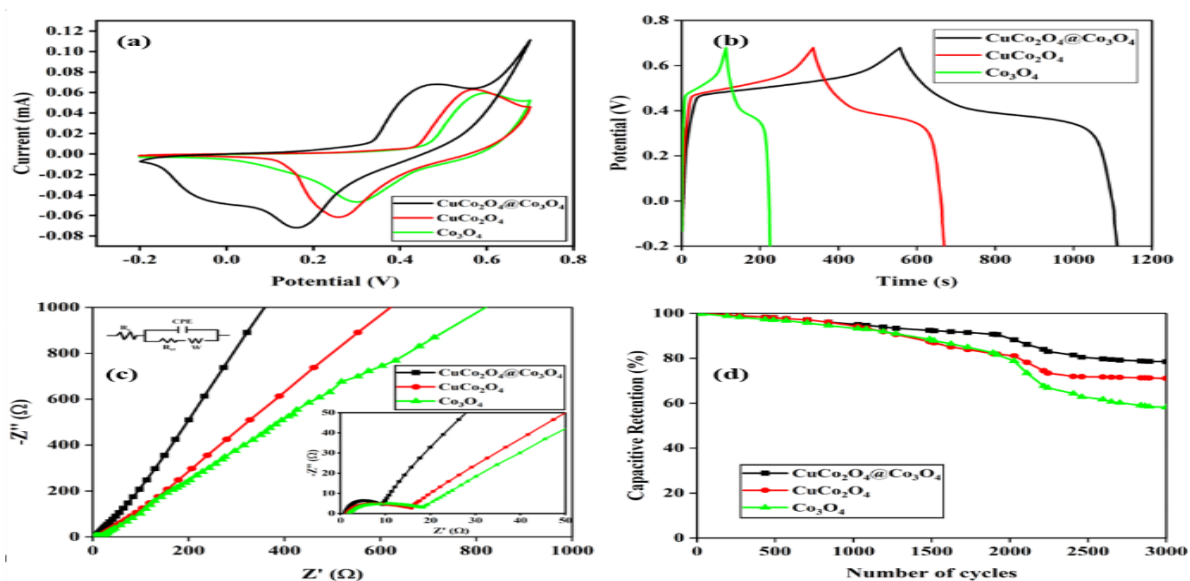


Fig. 6. CV of Co_3O_4 , CuCo_2O_4 , and $\text{CuCo}_2\text{O}_4@/\text{Co}_3\text{O}_4$ at 100 mV/s (a), GCD of Co_3O_4 , CuCo_2O_4 , and $\text{CuCo}_2\text{O}_4@/\text{Co}_3\text{O}_4$ at 1 A/g (b), and Nyquist plots of the samples (c), and Cyclic stability at 5 A/g (d) on NF.

Fig. 5 (a) and **Fig. 6 (a)** display the CV curves of the Co_3O_4 , CuCo_2O_4 , and $\text{CuCo}_2\text{O}_4@\text{Co}_3\text{O}_4$ composite respectively at 100 mV/s using GCE and NF as substrates. The nature of all the CV plots indicates the slight distinctive redox peaks using GCE and distinctive redox peaks using NF exhibiting pseudocapacitive behavior. The CV curve for the $\text{CuCo}_2\text{O}_4@\text{Co}_3\text{O}_4$ nanocomposite encompasses a larger area for both GCE and NF compared to the other synthesized materials, indicating an enhancement in the capacitive performance of the electrode. This enhancement is attributed to the greater surface area of the prepared electrode material, which facilitates rapid redox reactions. The GCD curves of the Co_3O_4 , CuCo_2O_4 , and $\text{CuCo}_2\text{O}_4@\text{Co}_3\text{O}_4$ composite on GCE and NF at 1 A g^{-1} are displayed in **Fig. 5 (b)** and **Fig. 6 (b)**. In terms of the aforementioned CV curves, the GCD curves of all three materials display a plateau rather than a linear dependency, suggesting the faradic behaviour of the electrode [20–23]. The specific capacitance calculated for Co_3O_4 , CuCo_2O_4 , and $\text{CuCo}_2\text{O}_4@\text{Co}_3\text{O}_4$ composite at 1 A g^{-1} using GCE was 158.33 Fg^{-1} , 186.11 Fg^{-1} and 542.77 Fg^{-1} whereas using NF was 139.00 Fg^{-1} , 411.00 Fg^{-1} and 683.72 Fg^{-1} which suggests that composite shows higher capacitance than the other materials in both the cases. Further impedance studies were conducted to evaluate the interfacial charge transfer of all the synthesized materials. EIS graphs are obtained by plotting Z' versus Z'' as depicted in **Fig. 5 (c)** and **Fig. 6 (c)** wherein the diameter of the semicircle for the composite was lesser compared to the other materials and the slope was higher for the composite with respect to the other pristine materials indicating a faster diffusion taking place. The values calculated from equivalent circuit fitting for $\text{CuCo}_2\text{O}_4@\text{Co}_3\text{O}_4$ on GCE were R_s ($0.84 \text{ } \Omega$) and R_{ct} ($10.51 \text{ } \Omega$) and on NF were R_s ($0.95 \text{ } \Omega$) and R_{ct} ($8.51 \text{ } \Omega$). For pristine CuCo_2O_4 and Co_3O_4 , on GCE were R_s ($1.19 \text{ } \Omega$), R_{ct} ($19.09 \text{ } \Omega$), R_s ($1.53 \text{ } \Omega$) and R_{ct} ($21.42 \text{ } \Omega$) and using NF were R_s ($1.53 \text{ } \Omega$), R_{ct} ($14.21 \text{ } \Omega$), R_s ($1.66 \text{ } \Omega$) and R_{ct} ($16.87 \text{ } \Omega$). Thus the values obtained for $\text{CuCo}_2\text{O}_4@\text{Co}_3\text{O}_4$ are lower than the values obtained for pure CuCo_2O_4 and pristine Co_3O_4 nanomaterials respectively for both the substrates which

suggests a better capacitive nature of the composite compared to the other materials [16]. Cyclic stability was employed as it plays a pivotal role in supercapacitor application. The cyclic stability of all the materials was evaluated on GCE and NF for $\text{CuCo}_2\text{O}_4@\text{Co}_3\text{O}_4$ nanocomposite at 5 Ag^{-1} wherein retention was found to be 76% and 78% upto 1000 and 3000 cycles respectively. The retention for CuCo_2O_4 and Co_3O_4 nanomaterials was observed on GCE as 65% and 47% upto 1000 cycles and NF as 71% and 58% until 3000 cycles respectively at 5 Ag^{-1} [16]. Thus, the $\text{CuCo}_2\text{O}_4@\text{Co}_3\text{O}_4$ nanocomposite has the potential to serve as an exceptional electrode material for high-performance supercapacitors.

4. Conclusion

To summarize, we have successfully developed a hydrothermal technique for the synthesis of $\text{CuCo}_2\text{O}_4@\text{Co}_3\text{O}_4$ nanocomposite for supercapacitive applications. FT-IR, XRD, FE-SEM, analysis verified the successful synthesis and validation of the corresponding nanomaterials and $\text{CuCo}_2\text{O}_4@\text{Co}_3\text{O}_4$ nanocomposite. From the electrochemical studies, it was evident that $\text{CuCo}_2\text{O}_4@\text{Co}_3\text{O}_4$ nanocomposite using nickel foam, the specific capacitance was higher at 683.72 Fg^{-1} than the GCE, which was computed at 542.77 Fg^{-1} at the same current density of 1 Ag^{-1} . Furthermore, $\text{CuCo}_2\text{O}_4@\text{Co}_3\text{O}_4$ nanocomposite with nickel foam as the electrode substrate showed good cyclic stability of 78% for up to 3000 cycles than GCE as 76% up to 1000 cycles at 5 Ag^{-1} .

Acknowledgments

The authors greatly thank Micro-Analytical Laboratory, Department of Chemistry, University of Mumbai for providing Instrumental facilities. The authors also thank IIT Bombay for providing XRD, XPS measurements and SEM analysis. One author, Bhakti G. Thali, is grateful to Savitribai Jyotirao Phule Single Girl Child Fellowship (SJSGC) UGC, Delhi, India for SRF.

5. References

- [1] Zhong Y, Xia X, Mai W, Tu J, Fan H J Integration of Energy Harvesting and Electrochemical Storage Devices. *Adv. Mater. Technol.* (2017) 2:1–14. <https://doi.org/10.1002/admt.201700182>
- [2] Krishnan S G, Reddy M, Harilal M, Vidyadharan B, Jose R Characterization of MgCo_2O_4 as an electrode for high performance supercapacitors. *Electrochim. Acta.* (2015) 161:312–321. <https://doi.org/10.1016/j.electacta.2015.02.081>
- [3] Chen Hu, Xuming Du, Runze Wu, Wang Ya, Jiale Sun, Yanfei Zhang, Chunju Xu Facile hydrothermal synthesis of porous MgCo_2O_4 nanoflakes as electrode material for high–performance asymmetric supercapacitors. *Nanoscale Advances* (2023) 1043–1059. <https://doi.org/10.1039/D3NA00462G>
- [4] Shanmugavalli V, Vishista K An Investigation on the Supercapacitive Performance of CuCo_2O_4 /Polyaniline, a Nanocomposite of Spinel Structured Transition Binary Metal Oxide and Conducting Polymer, with a Special Focus on Bonding and Electron Density Distribution Through MEM. *J. Inorg. Organomet. Polym. Mater.* (2020) 30:1448–1462. <https://doi.org/10.1007/s10904-019-01268-z>
- [5] Dakshayini B S, Reddy K R, Mishra A, Shetti N P, Malode S J, Basu S, Naveen S, Raghu Anjanapura V Role of conducting polymer and metal oxide–based hybrids for applications in amperometric sensors and biosensors. *Microchem. J.* (2019) 147:7–24. <https://doi.org/10.1016/j.microc.2019.02.061>
- [6] Duan L, Gao F, Wang L, Jin S, Wu H Hydrothermal synthesis and characterization of MnCo_2O_4 in the low-temperature hydrothermal process: Their magnetism and electrochemical properties. *J. Adv. Ceram.* (2013) 2:266–273. <https://doi.org/10.1007/S40145-013-0070-0>

- [7] Yana Li, Xianhua Hou, Yajie Li, Qiang Ru, Wang, Hu Shaofeng, Lam Shejun, Kwok-Ho Facile Synthesis of Hierarchical CoMn_2O_4 Microspheres with Porous and Micro-Nanostructural Morphology as Anode Electrodes for Lithium-Ion Batteries. *Electron. Mater. Lett.* (2017) 13:427–433. <https://doi.org/10.1007/s13391-017-6258-7>
- [8] Li J, Xiong S, Li X, Qian YA facile route to synthesize multiporous MnCo_2O_4 and CoMn_2O_4 spinel quasi-hollow spheres with improved lithium storage properties. *Nanoscale* (2013) 5:2045–2054. <https://doi.org/10.1039/C2NR33576J>
- [9] Silambarasan M, Padmanathan N, Ramesh P S, Geetha D Spinel CuCo_2O_4 Nanoparticles: Facile One-Step Synthesis, Optical, and Electrochemical properties. *Mater. Res. Express.* (2016) 3:1–10. <https://doi.org/10.1088/2053-1591/3/9/095021>
- [10] Wang Q, Xu J, Wang X Core-Shell $\text{CuCo}_2\text{O}_4@ \text{MnO}_2$ Nanowires on Carbon Fabrics as High-Performance Materials for Flexible, All-Solid-State, Electrochemical Capacitors. *Chem. Electro. Chem.* (2014) 1:559–564. <https://doi.org/10.1002/CELC.201300084>
- [11] Pendashteh A, Moosavifard Seyyed E, Rahmanifar Mohammad S, Wang Yue Highly Ordered Mesoporous CuCo_2O_4 Nanowires, a Promising Solution for High-Performance Supercapacitors. *Chem. Mater.* (2015) 27:3919–3926. <https://doi.org/10.1021/acs.chemmater.5b00706>
- [12] Jang G S, Ameen S, Akhtar M S, Kim E, and Shin H S Electrochemical Investigations of Hydrothermally Synthesized Porous Cobalt Oxide (Co_3O_4) Nanorods: Supercapacitor Application. *ChemistrySelect* (2017) 2:8941–8949. <https://doi.org/10.1002/slct.201701571>

- [13] Hasan I and Alharthi F A Synthesis of Cobalt Oxide (Co_3O_4) Nanoparticles for Efficient Photocatalytic Water Splitting and Hydrogen Production. *ChemistrySelect* (2023) 8:202302685. <https://doi.org/10.1002/SLCT.202302685>
- [14] Wang Q, Jiang M, Zhang L Label-free and visible-light driven photoelectrochemical sensor with $\text{CuCo}_2\text{O}_4@ \text{CoO}$ Core-shell hybrid rod as photoanode for selective sensing diclofenac. *Electrochim. Acta.* (2021) 397:139239. <https://doi.org/10.1016/j.electacta.2021.139239>
- [15] Jiang F, Su Q, Li H, Yao L, Deng H, Du G Growth of ultrafine CuCo_2O_4 nanoparticle on graphene with enhanced lithium storage properties. *J. Chem. Engg.* (2017) 314:301–310. <https://doi.org/10.1016/J.CEJ.2016.11.064>
- [16] Thali B G, Kamble R M Synthesis and electrochemical properties of $\text{CuCo}_2\text{O}_4@ \text{Co}_3\text{O}_4$ nanocomposite for supercapacitor application. *J. Solid State Electrochem.* (2024) 1–15. <https://doi.org/10.1007/s10008-024-05909-3>
- [17] Das D, Saikia B Jyoti Synthesis, characterization and biological applications of cobalt oxide (Co_3O_4) nanoparticles. *Chem. Phys. Impact* (2022) 6:1–3. <https://doi.org/10.1016/j.chphi.2022.100137>
- [18] Sivashanmugam G, Lakshmi K, Preethi B, Nelson S, Sathiyaseelan M CTAB-templated formation of $\text{CuCo}_2\text{O}_4/\text{CuO}$ nanorods and nanosheets for high-performance supercapacitor applications. *J. Mater. Sci. Mater. Electron.* (2021) 32:27148–27158. <https://doi.org/10.1007/S10854-021-06845-Y>
- [19] Patil K N, Prasad D, Bhanushali D, Kim J T, Atar H, Nagaraja A B, Jadhav B M Sustainable Hydrogen Generation by Catalytic Hydrolysis of NaBH_4 Using Tailored Nanostructured Urchin-like CuCo_2O_4 Spinel Catalyst. *Catal. Letters* (2020) 150:586–604. <https://doi.org/10.1007/S10562-019-03025-W>

- [20] Javed M S, Dai S, Wang M, Xi Yi Faradic redox active material of Cu₇S₄ nanowires with a high conductance for flexible solid–state supercapacitors. *Nanoscale* (2015) 7:13610–13618. <https://doi.org/10.1039/C5NR03363B>
- [21] Wang X, Ding H, Luo Wei, Yu Yi, Chen Q, LuO B, Xie M, Guo X Morphology evolution of CoNi-LDHs synergistically engineered by precipitant and variable cobalt for asymmetric supercapacitor with superior cycling stability. *EcoEnergy*. (2023) 1:448—459. <https://doi.org/10.1002/ece2.21>
- [22] Zhang Y, Hu Y, Wang Z, Lin T, Zhu Xi Lithiation–Induced Vacancy Engineering of Co₃O₄ with Improved Faradic Reactivity for High–Performance Supercapacitor. *Adv. Funct. Mater.* (2020) 30:2004172. <https://doi.org/10.1002/adfm.202004172>
- [23] Nawaz B, Ullah M O, Ali G An investigation of the electrochemical properties of CuCo₂O₄@NiCo₂O₄ composite as binder-free electrodes of a supercapacitor. *Energies* (Basel), (2014) 14:3237. <https://doi.org/10.3390/en14113237>

Workshop-EST-2024

Members of Local Organising Committee

C.N. Patra

A.K. Satpati

Sangita D. Kumar

Sanjukta A. Kumar

K. K. Swain

P. K. Mishra

V. T. Aher

M. K. Dey

Srikant Sahoo

Mohsin Jafar

Sudipa Manna

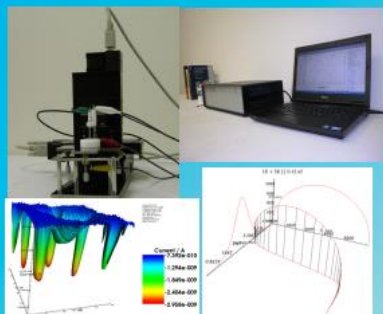
Mridusmita Sarma

S. S. Pawar

P. Bhaye

Sinsil International Pvt Ltd

Your Partner in Scientific Needs



Electrochemical Workstation
CH Instruments
www.chinstruments.com



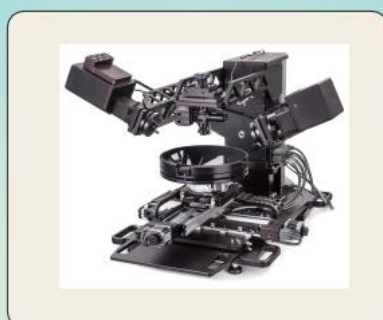
ZHN Nanoindenter
ZwickRoell
www.zwickroell.com



Confocal Microscope
ISS
www.iss.com



Dielectric Impedance Analyzer
Novocontrol
www.novocontrol.com



Ellipsometer
J.A.Woollam
www.jawoollam.com



3D Profilometer
Filmetrics
www.filmetrics.com



Gravimetric Sorption Analyzer
Rubolab
www.rubolab.de



Solar Simulator
Photo Emission Tech
www.photoemission.com



UV-VIS-Fibre Optics Spectrometer
Ocean Insight
www.oceaninsight.com

SINSIL INTERNATIONAL PVT LTD

NO 31, OPP S J E S College
Old Madras Road,
Medahalli, Virgonagar Post,
Bengaluru-560049.

Email:- bangalore@sinsil.in

+91-80-50891594

+91-9341282569

Sinsil Intl

Baroda : info@sinsil.in

Delhi : delhi@sinsil.in

Kolkata : kolkata@sinsil.in

Chennai: bangalore@sinsil.in

Mumbai : mumbai@sinsil.in

Hyderabad: bangalore@sinsil.in

+91-9167404043

+91-9312437300

+91-9681442892

+91-9980287123

+91-9833011933

+91-8008999507

www.sinsilinternational.com



Indian Society for ElectroAnalytical Chemistry

www.iseac.org.in